

https://dspace.org/

Adaptive wall wind tunnel investigation of a circulation controlled circular cylinder

Berndt, Roland Gunther

2016-07-19
http://hdl.handle.net/10539/20664

Downloaded from a DSpace repository. https://dspace.org/

ADAPTIVE WALL WIND TUNNEL

INVESTIGATION OF A CIRCULATIO

CONTROLLED CIRCULAR CYLINDER

AUTHOR : Roland Günther Berndt

SUPERVISOR : Professor A Nurick

BRANCH OF AERONAUTICAL ENGINEERING

UNIVERSITY OF THE WITWATERSRAND

Abstract

A low speed adaptive wall wind tunnel investigation of a circulation controlled circular cylinder, with 4 independently adjustable slots, was undertaken. A 2-D adaptive wall wind tunnel was designed and commissioned to accurately measure the aerodynamic performance of high-lift aerofoils with minimal tunnel boundary interference. A simple potential flow wall streamlining strategy was used to minimize tunnel boundary interferences, and found to be satisfactory. The power coefficient was shown to be a useful parameter in comparing the merits of different slot configurations. It was found that lift is a function of the number of slots, slot location and slot thickness. Also, for any given slot configuration, a slot thickness exists that maximizes the lift. With respect to power input, the optimum configuration tested had four equal slots (t/c = 0.015) positioned at 70°, 105°, 140° and 175°.

Acknowledgements

The author wishes to thank the following people:

Professor Alan Nurick for enthusiastic supervision, technical advice and financial assistance, both personal and project related.

The Mechanical Engineering Laboratory staff for the manufacture of the wind tunnel and model. A special word of thanks to the following technicians:
John Coetzee
Robert Broadhurst
John Cooper

Declaration

I, Roland Gunter Berndt, declare that this research report is my own work. It is being submitted to the Branch of Aeronautical Engineering of the University of the Witwatersrand, Johannesburg South Africa, for the Degree of Master of Science in Aeronautical Engineering. It has not been submitted before for any other degree.

Roland Gunter Berndt

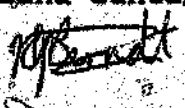

Nomenclature

Upper case

A	Boundary layer magnitude coefficient.
	Area (m^2).
B	Boundary layer shift coefficient.
C_d	Drag coefficient.
C_l	Lift coefficient.
C_p	Pressure coefficient.
C_{pow}	Power coefficient.
C_q	Flow rate coefficient.
C_μ	Momentum coefficient.
D	Diameter.
	Drag (N).
ER_t	Tunnel energy ratio.
K_0	Loss coefficient.
L	Length (m).
	Lift (N).
M	Mach number.
P	Power.
Q	Flow rate (m^3/s).
Re	Reynold's number.
S	Wing area (m^2).
U	Tunnel speed (m/s).
	Velocity in x direction (m/s).
V	Velocity (m/s).
	Velocity in y direction (m/s).

Lower case

a	Cylinder radius (m).
b	Aerofoil wingspan (m).
c	Aerofoil chord (m).
d	Cylinder diameter (m).
k	Circulation (m^2/s).
	Vortex strength (m^2/s).
m	Slope of curve.
p	Pressure.
q	Source strength per unit span (m^2/s).
	Dynamic pressure (Pa).
r	Radius (m).
t	Slot thickness (m).
x	Longitudinal test section coordinate (m).

y	Transverse test section coordinate (m).
z	Vertical test section coordinate (m).

Greek upper case

Ψ	Stream function (m^2/s).

Greek lower case

$\alpha/2$	Diffuser half-angle.
γ	Specific heat ratio.
δ	Boundary layer thickness.
δ^*	Boundary layer displacement thickness.
η	Mechanical efficiency.
θ	Slot reference angle.
λ	Skin friction coefficient.
ρ	Density (kg/m^3).
μ	Dynamic viscosity (Pa.s).
	Doublet strength (m^2/s).

Subscripts

0	Test section.
2	Diffuser exit.
c	Contraction.
jet	Slot efflux.
t	Test section.
tr	Transition.

Abbreviations

2-D	Two-dimensional.
3-D	Three dimensional.
CC	Circulation control.
CCTB	Circulation Control Tail Boom.
NPL	National Physical Laboratory.

Definitions

$q = 0.5\ \rho\ U^2$.

$C_d = D/(q\ S)$.

$C_l = L/(q\ S)$.

$C_p = p_{jet}/q$.

$C_{pow} = P/(q\ S\ U) = (p\ Q)_{jet}/(q\ S\ U)$.

$C_q = Q_{jet}/(S\ U)$.

$C_\mu = (\rho\ Q\ V)_{jet}/(q\ S) = (\rho\ Q^2)_{jet}/((t/c)^3 q\ S)$.

Table of Contents

Abstract i

Acknowledgements ii

Declaration iii

Nomenclature iv

Table of Contents vi

1 Introduction 1
1.1 Background 1
1.2 Circulation Controlled Tail Boom 1
1.3 Advantages of the CCTB 3
1.4 Wind Tunnel Testing 4
1.5 Adaptive Wall Wind Tunnels 5

2 Objectives 6

3 Literature Survey 7
3.1 Wind Tunnel Testing 7
3.1.1 Types of Wind Tunnels 7
3.1.1.1 Open Circuit Tunnels 7
3.1.1.2 Continuous Circuit Tunnels 8
3.1.2 Similarity Considerations 9
3.1.3 Two-Dimensional Testing 10
3.1.4 Wind Tunnel Interferences 11
3.2 Adaptive Wall Wind Tunnels 13
3.2.1 Background 13
3.2.2 Adaptive Wall Wind Tunnel Types 14
3.2.2.1 Ventilated Wall Test Section . . . 14
3.2.2.2 Flexible Wall Test Section 15
3.2.3 Advantages of Adaptive Wall Tunnels . . . 17
3.2.3.1 Higher Reynold's Number 17
3.2.3.2 Reduced Power Requirements 17
3.2.3.3 Rapid Data Availability 18
3.2.3.4 Improved Flow Quality 18
3.2.3.5 Test Mode Versatility 18
3.2.4 Disadvantages of Adaptive Wall Tunnels . . 21
3.2.4.1 Operational Aspects 22
3.2.4.2 Increased Cost and Complexity . . . 21

3.2.5 Wall Streamlining Strategy 22
3.2.5.1 The NRL Strategy 22
3.2.5.2 The Potential Flow Strategy . . . 22
3.2.5.3 Self-Streamlining Strategy 23
3.3 The CCTB Concept 23
3.4 Circulation Controlled Aerofoils 24
3.4.1 Analytical Methods 24
3.4.2 Experimental Methods 26

4 Design of Equipment 29
4.1 Description of Wind Tunnel 30
4.1.1 Inlet Contraction 30
4.1.2 Inlet Honeycomb 30
4.1.3 Test Section 31
4.1.3.1 Rigid Top and Bottom Walls . . . 31
4.1.3.2 Flexible Side Walls 32
4.1.3.3 Slides 32
4.1.3.4 Actuators 33
4.1.3.5 Actuator Power Supplies 33
4.1.3.6 Wall Suction Fan 34
4.1.4 Exit Honeycomb 34
4.1.5 Diffuser 35
4.1.6 Control Room 35
4.1.7 Tunnel Drive Fans 35
4.2 Wind Tunnel Calculations 36
4.2.1 Tunnel Power and Size 36
4.2.1.1 Tunnel Losses 37
4.2.1.2 Inlet Contraction 38
4.2.1.3 Test Section 38
4.2.1.4 Diffuser 39
4.2.1.5 Transition 39
4.2.2 Structural Considerations 40
4.3 Model and Balance 41
4.3.1 Model 41
4.3.2 Balance 42
4.3.3 Circulation Control Air Supply 42
4.3.4 Orifice Plate 42
4.4 Data Acquisition and Control 43
4.4.1 Transducers 43
4.4.1.1 Load Cells 43
4.4.1.2 Pressure Transducers 43
4.4.1.3 Position Transducers 43
4.4.2 A/D System 44
4.4.3 I/O System 44

4.5 Software Design 44
4.5.1 Calibration Software 44
4.5.1.1 Raw Data Acquisition 44
4.5.1.1.1 Position Transducers . . . 44
4.5.1.1.2 Load Transducers 45
4.5.1.1.3 Pressure Transducers . . . 45
4.5.1.1.4 Tunnel Speed Calibration . 45
4.5.1.2 Data Processing 45
4.5.1.2.1 Position Transducers . . . 45
4.5.1.2.2 Load and Pressure 46
4.5.1.2.3 Tunnel Speed 46
4.5.2 Operating Software 46
4.5.3 Utility Software 46
4.5.3.1 Velocity Traverse 46
4.5.3.2 Relay Checking 47
4.5.3.3 Data Acquisition 47
4.5.3.4 Wall Pressure Calculation . . . 47

5 Theoretical Analysis 54
5.1 Wall Streamlining Theory 54
5.1.1 Potential Flow 56
5.1.1.1 Elementary Flows 56
5.1.1.2 Combined Flow 56
5.1.2 Newton - Raphson Method 58
5.2 Dimensional Analysis 59
5.3 Error Analysis 61

6 Calibration of Equipment 65
6.1 Wind Tunnel Calibration 65
6.1.1 Test Section Velocity Traverse 65
6.1.2 Test Section Flow Angularity 66
6.1.3 Tunnel Turbulence Level 67
6.1.4 Wall Boundary Layer Correction 67
6.1.5 Tunnel Speed Setting 69
6.2 Data Acquisition Calibration 69
6.2.1 Position Transducers 69
6.2.2 Pressure Transducers 70
6.2.3 Load Cells 71

7 Experimental Procedure 83
7.1 Tunnel initialization 83
7.2 Acquiring data 83
7.3 Terminating a test 84

8 Results 85
8.1 Adaptive Wall Wind Tunnel 85
8.1.1 Wall Streamlining Strategy 85
8.2 Tests on CC Cylinder 85
8.2.1 Test Schedule 85
8.2.2 Processed Data 87

9 Discussion 108
9.1 Adaptive Wall Wind Tunnel 108
9.1.1 Wall Streamlining Strategy 108
9.2 Tests on CC Cylinder 112
9.2.1 Drag of the Cylinder 112
9.2.2 Dimensionless Groups 114
9.2.3 Effect of Reynold's Number 115
9.2.4 Comparison of Configurations 116
9.2.5 Effect of Number of Slots 118
9.2.6 Effect of Slot Thickness 119
9.2.7 Effect of Slot Location 120
9.2.8 Analysis of a Single Configuration . . . 121

10 Conclusions 127
10.1 Adaptive Wall Wind Tunnel 127
10.2 Tests on CC Cylinder 127

11 Recommendations 128
11.1 Wind Tunnel 128
11.2 Software 129
11.3 Streamlining Algorithm 130
11.4 Further Tests 130

12 References and Bibliography 131
12.1 References 131
12.2 Bibliography 133

Appendix A
Orifice Plate Calculations A1
A.1 Working Equations in Metric Units A1
A.2 Correction Coefficients d = 125mm A2
A.2.1 Discharge Coefficient A2
A.2.2 Reynold's Number Correction A2
A.2.3 Pipe Diameter Correction A3
A.2.4 Expansibility Factor A3
A.3 Correction Coefficients d = 100mm A4
A.3.1 Discharge Coefficient A4

A.3.2 Reynold's Number Correction A4
A.3.3 Pipe Diameter Correction A4
A.3.4 Expansibility Factor A4

Appendix B
Wall Pressure Distribution B1
B.1 Elementary Flows B1
B.1.1 Uniform Stream B1
B.1.2 Source B1
B.1.3 Doublet B1
B.1.4 Vortex B2
B.2 Combined Flow B2
B.3 Pressure Difference B2

Appendix C
Structural Analysis C1
C.1 Test Section Beams C1
C.2 Test Section Floor and Ceiling C2
C.3 Flexible Walls C3

Appendix D
Fan Characteristics D1
D.1 Tunnel Drive Fans D1
D.2 Circulation Control Blower D2
D.3 Wall Suction Fan D3

Appendix E
Wiring Diagrams E1
E.1 A/D, I/O and PC Interface E1
E.2 Transducer Wiring E2
E.3 Actuator Relay Wiring E3

Appendix F
Software F1

List of Figures

Figure 1.1: General arrangement of the CCTB system.[3] . . . 2
Figure 1.2: Comparison of conventional and CC aerofoils.[3] 2
Figure 3.1: Open circuit tunnel.[6] 8
Figure 3.2: Continuous circuit tunnel.[24] 9
Figure 3.3: Ventilated wall test section.[9] 15
Figure 3.4: Unconfined flow about an aerofoil.[10] 15
Figure 3.5: Flexible wall test section.[9] 16
Figure 3.6: The principle of test section streamlining. . 16
Figure 3.7: Closed tunnel mode.[9] 18
Figure 3.8: Open jet mode.[9] 19
Figure 3.9: Infinite flow field mode.[9] 19
Figure 3.10: Ground effect mode.[9] 20
Figure 3.11: Cascade mode.[9] 20
Figure 3.12: Steady pitching mode.[9] 21
Figure 3.13: Dunham's CC cylinder (schematic).[17] 24
Figure 3.14: Effect of t/c on C_l vs C_μ.[17] 25
Figure 3.15: Variation of C_l with C_μ for an ellipse.[20] . . 26
Figure 3.16: C_l vs C_μ. Cylinder with 2 slots 90° apart.[19] 28
Figure 4.1: Plan and side view of the adaptive tunnel. . 29
Figure 4.2: Schematic diagram of the generic tunnel. . . 37
Figure 4.3: Skin friction vs Re.[6] 38
Figure 5.1: Pressure distribution about cylinder.[17] . . . 54
Figure 6.1: Test section velocity. y = -0.5m z = 0.15m 73
Figure 6.2: Test section velocity. y = -0.5m z = 0.05m 73
Figure 6.3: Test section velocity. y = -0.5m z = -0.05m 74
Figure 6.4: Test section velocity. y = -0.5m z = -0.15m 74
Figure 6.5: Test section velocity profiles. 75
Figure 6.6: Tunnel speed calibration curve. 75
Figure 6.7: Pressure transducer calibration (p_1). 76
Figure 6.8: Pressure transducer calibration (p_2). 76
Figure 6.9: Pressure transducer calibration (p_3). 77
Figure 6.10: Lift load cell calibration curve. 77
Figure 6.11: Drag load cell calibration curve. 78
Figure 8.1: Variation of C_d with Re_d. 93
Figure 8.2: C_l, C_d vs C_μ. 70°,1; 105°,1; 140°,1; 175°,1. . 93
Figure 8.3: C_l, C_d vs C_μ. 70°,2; 105°,2; 140°,2; 175°,2. 94
Figure 8.4: C_l, C_d vs C_μ. 70°,3; 105°,3; 140°,3; 175°,3. . 94
Figure 8.5: C_l, C_d vs C_μ. 70°,4; 105°,4; 140°,4; 175°,4. 95
Figure 8.6: C_l, C_d vs C_μ. 70°,5; 105°,5; 140°,5; 175°,5. . 95
Figure 8.7: C_l, C_d vs C_μ. 70°,1; 105°,1; 140°,1. 96

Figure 8.8: C_l, C_d vs C_μ. 70°,2; 105°,2; 140°,2. 96
Figure 8.9: C_l, C_d vs C_μ. 70°,3; 105°,3; 140°,3. 97
Figure 8.10: C_l, C_d vs C_μ. 70°,4; 105°,4; 140°,4. 97
Figure 8.11: C_l, C_d vs C_μ. 70°,5; 105°,5; 140°,5. 98
Figure 8.12: C_l, C_d vs C_μ. 70°,5; 105°,5; 140°,5. 98
Figure 8.13: C_l vs C_μ. 3 slots. 70°; 105°; 140°. 99
Figure 8.14: C_l vs C_{pow}. 3 slots. 70°; 105°; 140°. 99
Figure 8.15: C_l vs C_μ. 4 slots. 70°; 105°; 140°; 175°. . . . 100
Figure 8.16: C_l vs C_{pow}. 4 slots. 70°; 105°; 140°; 175°. . . 100
Figure 8.17: C_l vs C_μ. Slots at 70°; 105°; 140°; 175°. . . . 101
Figure 8.18: C_l vs C_{pow}. Slots at 70°; 105°; 140°; 175°. . . 101
Figure 8.19: C_l vs C_μ. Slots at 70°; 105°; 140°; 175°. . . . 102
Figure 8.20: C_l vs C_{pow}. Slots at 70°; 105°; 140°; 175°. . . 102
Figure 8.21: C_l vs C_μ. 3 slots. 3, 3, 3, 0. 103
Figure 8.22: C_l vs C_{pow}. 3 slots. 3, 3, 3, 0. 103
Figure 8.23: C_l vs C_μ. 2 slots. 3, 0, 3, 0. 104
Figure 8.24: C_l vs C_{pow}. 2 slots. 3, 0, 3, 0. 104
Figure 8.25: V_{jet} vs slot size. 3 slots. 70°; 105°; 140°. . . 105
Figure 8.26: V_{jet} vs C_p. 3 slots. 70°; 105°; 140°. 105
Figure 8.27: C_l vs C_q. 3 slots. 70°; 105°; 140°. 106
Figure 8.28: Slope of (C_l vs C_q) vs t/c. 106
Figure 8.29: Intercept of (C_l vs C_q) vs t/c. 107
Figure 8.30: C_l vs t. 3 slots. 70°; 105°; 140°. 107
Figure 9.1: Documented variation of C_d with Re_d. 112
Figure A.1: Discharge coefficient. A5
Figure A.2: Reynold's number correction factor. A5
Figure A.3: Pipe size correction factor. A5
Figure A.4: Expansibility factor. A6

List of Plates

Plate 4,1: Wind tunnel viewed from the front. 48
Plate 4,2: Wind tunnel viewed from behind. 48
Plate 4,3: Test section inlet. 49
Plate 4,4: Side view of the test section. 49
Plate 4,5: Internal view of the test section. 50
Plate 4,6: View of a slide. 50
Plate 4,7: View of an actuator. 51
Plate 4,8: View of the control room. 51
Plate 4,9: View of the CC cylinder. 52
Plate 4,10: View of the blowing slots. 52
Plate 4,11: View of the balance. 53
Plate 4,12: Circulation control blower. 53
Plate 6,1: Velocity traverse arrangement. 79
Plate 6,2: Tuft screen right hand side. 79
Plate 6,3: Tuft screen left hand side. 80
Plate 6,4: Corrected wall pressure distribution. 80
Plate 6,5: Top view of the calibration rig. 81
Plate 6,6: Front view of the calibration rig. 81
Plate 6,7: Loading the balance. 82
Plate 8,1: Wall pressures U=30 C_l=0. 88
Plate 8,2: Wall pressures U=30 C_l=1. 88
Plate 8,3: Wall pressures U=30 C_l=2. 89
Plate 8,4: Wall pressures U=30 C_l=3. 89
Plate 8,5: Wall pressures U=30 C_l=4. 90
Plate 8,6: Wall pressures U=40 C_l=0. 90
Plate 8,7: Wall pressures U=40 C_l=1. 91
Plate 8,8: Wall pressures U=40 C_l=2. 91
Plate 8,9: Wall pressures U=40 C_l=3. 92

1 Introduction

1.1 Background

The function of the tail rotor on a conventional helicopter is to counteract the torque applied to the main rotor, as well as to provide yaw control about the main rotor axis. As the main rotor torque is varied, it is necessary to vary the thrust of the tail rotor to maintain angular equilibrium about the main rotor axis. Furthermore, to provide yaw control, the tail rotor thrust must be variable. The tail rotor is a complex mechanical system, requiring a drive shaft from the main rotor gearbox, as well as a collective pitch mechanism. If the tail rotor of a helicopter could be eliminated, the aircraft could become simpler and cheaper.

1.2 Circulation Controlled Tail Boom

Circulation control (CC) by blowing, applied to the tail boom of a helicopter, can be used as a means of counteracting the main rotor torque. Hughes Helicopters and McDonnell Douglas have been investigating this concept, which is referred to as the NOTAR (No Tail Rotor) system, since 1976[1,2]. Since NOTAR is a trademark, the system shall henceforth be referred to as the Circulation Controlled Tail Boom or CCTB. The CCTB concept has been an area of much interest in recent times, since it has distinct advantages over conventional tail rotor anti-torque systems. Figure 1.1 shows how the tail rotor of the conventional helicopter is replaced by a CC tail boom as well as a thruster arrangement, a variable pitch fan situated forward of the tail boom supplying the necessary airflow to the boom and thruster.

The tail boom makes use of the main rotor downwash and CC blowing to generate an anti-torque moment about the main rotor axis. The jet thruster at the end of the tail boom allows the anti-torque moment to be continuously varied. Of interest to this research is the mechanism of lift production (in the sideways direction), of the circular-section CC tail boom. Figure 1.2 shows how a CC cylinder is functionally similar to the conventional aerofoil, but whereas conventional aerofoils generate circulation by viscous means (largely in the vicinity of the trailing edge) to satisfy the Kutta condition, the CC cylinder derives its circulation from fluid discharged tangentially onto a Coanda

surface via longitudinal slots.

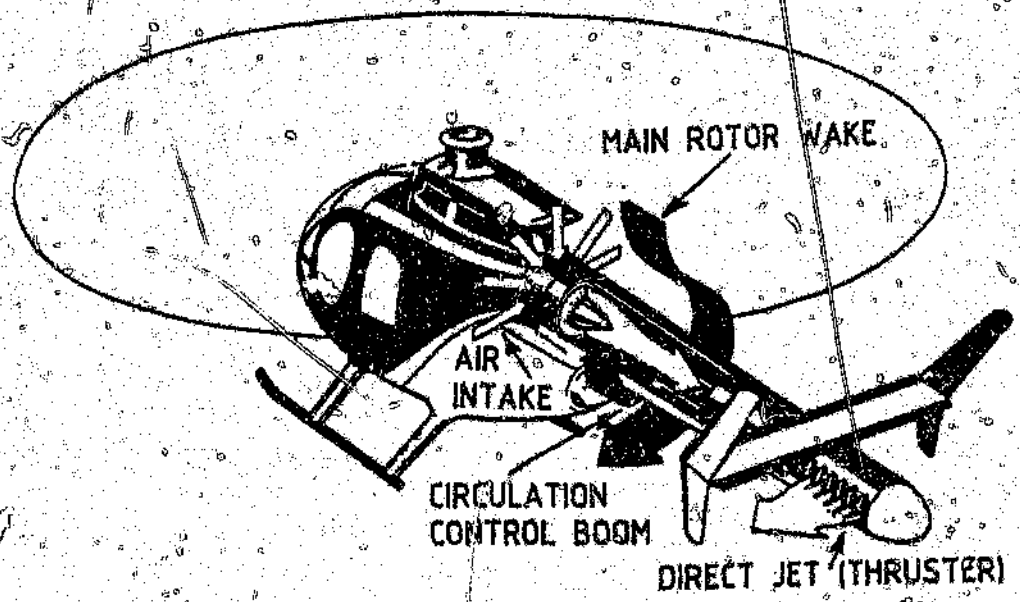

Figure 1.1: General arrangement of the CCTB system.[3]

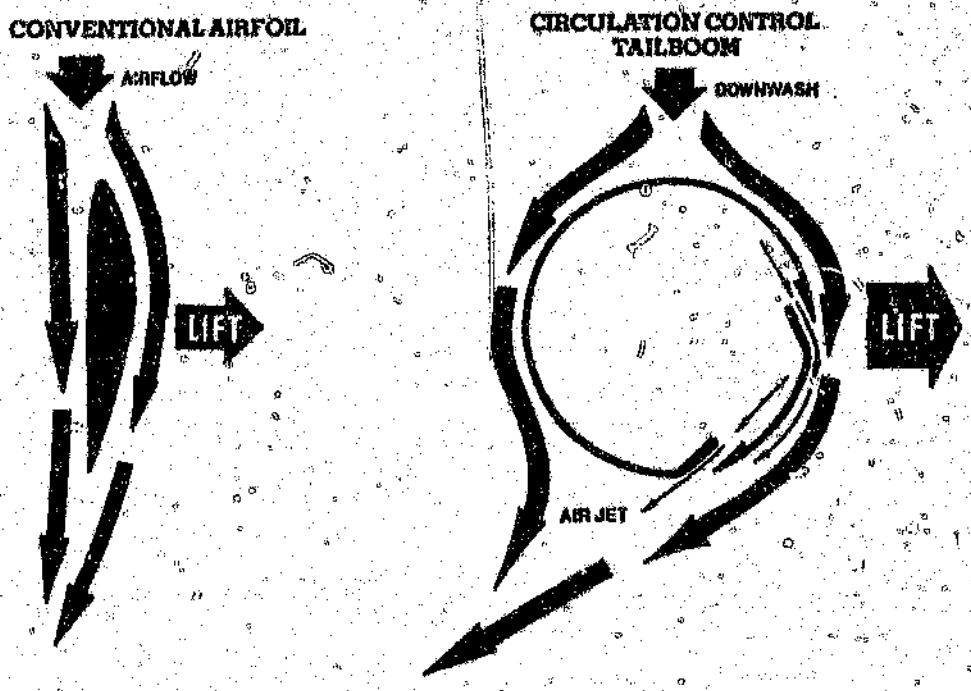

Figure 1.2: Comparison of conventional and CC aerofoils.[3]

1.3 Advantages of the CCTB

Nurick[4] gives several advantages of the circulation controlled tail boom (CCTB) over the conventional tail rotor.

1 **Mechanical complexity**
The tail rotor, its collective pitch mechanism, as well as the tail rotor gearbox and drive shaft are eliminated. Removing these items reduces both the mass and the maintenance requirements of the aircraft. A CCTB helicopter does require an additional blower but since this is located near the main rotor gearbox, undue mechanical complexity is circumvented.

2 **Danger**
More helicopter-related injuries are caused by the tail rotor than the main rotor.[1,2] With no moving blades except for the main rotor, the CCTB helicopter is inherently safer for ground personnel and passengers.

3 **Damage**
The tail rotor is more susceptible to damage than most other components of the helicopter.[1,2] A tail rotor striking the ground or a tree can result in a critical flight situation. Moreover, for military scenarios, the tail rotor is one of the more vulnerable components, especially from small arms fire.

4 **Noise**
The tail rotor is a source of considerable noise since tail rotor tip speeds are comparable to main rotor tip speeds. This consideration is particularly relevant to helicopters operating in a civilian environment. Although the CCTB helicopter may emit a higher pitched shear noise caused by air being ejected from the circulation control slots, being a high frequency sound emission, this will attenuate more rapidly than a low pitched oscillating emission.

McDonnell Douglas Helicopter Company has pioneered the use of CCTB technology on production helicopters with their MD 520N NOTAR (NO TAil Rotor) project.[1,2]

Ongoing research on the CCTB concept conducted by the School of Mechanical Engineering at the University of the Witwatersrand has

dealt with, amongst others, the 2-D and 3-D flow field around the boom. The 2-D research has focused on a numerical analysis by Groesbeek[5], while fully 3-D research has been performed on an outdoor helicopter rotor rig incorporating a CCTB. Due to the exposed environment of the latter facility, the results are affected by uncontrollable factors such as gusts of wind. Also, because the interaction between the rotor flow field and the CCTB is complex, 2-D effects which are fundamental to the flow field are masked by 3-D effects, making the analysis of data more difficult.

Since no experimental work had been done on the 2-D flow field around a CCTB, it was decided to perform 2-D wind tunnel tests on a CC cylinder with circular cross-section, in an attempt to gain greater insight into the mechanisms affecting boundary layer control and the flow field in general. The use of a 2-D tunnel allows the flow about a CC cylinder to be investigated without the confusing interaction of spanwise flows and other 3-D effects. Data obtained from a controlled 2-D environment can then be extended to evaluate the more complex 3-D flow field of a CCTB.

1.4 Wind Tunnel Testing

Conventional wind tunnels produce data with inherent errors because the wind tunnel affects the flow around the model being tested.[6,7] If the model is large compared to the size of the test section, the flow field about the model is seriously distorted, this distortion being referred to as wind tunnel boundary interference. Data obtained in such cases is usually modified by applying wind tunnel interference corrections to the data. The problem with such corrections is that they are usually either empirical, or otherwise based on classical inviscid flow theory. Empirical corrections are mostly limited to specific cases, while classical inviscid corrections only correct inaccuracies caused by the tunnel walls on the inviscid portion of the flow, neglecting the obviously important viscous portions of the flow such as the boundary layer and turbulent wake. The effect of the wind tunnel walls on the an aerofoil is to change its effective shape, especially at high lift coefficients. The shape of the boundary layer on a CC aerofoil is very crucial to its correct operation, and since CC is usually employed in high-lift aerofoils, there is a problem in ascertaining whether the corrected results from a fixed wall wind tunnel are correct, and

if not so, to what extent. Especially in the case of a CC cylinder, the focus of this research, the effect of the tunnel blockage is large, and cannot be eliminated by the application of post-test corrections.

1.5 Adaptive Wall Wind Tunnels

The adaptive wall wind tunnel solves the interference problem at its very source, namely at the wind tunnel boundaries. The flow field far away from the aerofoil is essentially inviscid, and since the walls of the wind tunnel are usually situated in the far flow field of the aerofoil, it is possible to apply the classical wind tunnel corrections to the walls of the tunnel instead of to the recorded data. If the wind tunnel walls are positioned in such a way as not to interfere with the model, ie. as if they were streamlines, then the recorded data will be correct as it was measured. Also, since the aerofoil is operating in an unconfined freestream, the boundary layer shape on its surface will be correct. Therefore, any measurements of the viscous flow field (boundary layer velocity profiles etc.), which can normally not be corrected, are correct to start of with. The success of the adaptive wall testing technique is based on the fact that, at any point in time, it will be easier to model the flow field in the region of the tunnel walls, than at the model. The adaptive wall testing technique therefore employs numerical methods to increase the accuracy of an experimental facility.

2 Objectives

1. Design and commission an adaptive wall wind tunnel, with particular emphasis on the capability of testing aerofoils at high lift coefficients.
2. Verify the correct operation of the adaptive wall wind tunnel.
3. Investigate the effects of slot size, location, thickness and blowing momentum on the lift and drag of a circulation controlled cylinder.
4. Investigate the effect of various slot configurations on the absorbed power per unit lift of the circulation controlled cylinder.

3 Literature Survey

A literature survey was conducted with specific emphasis on:

1 Wind tunnel testing.
2 Adaptive wall wind tunnels.
3 The circulation controlled tail boom (CCTB) concept.
4 Circulation controlled aerofoils, particularly those with a circular cross-section.

3.1 Wind Tunnel Testing

The primary aim of wind tunnel testing is to simulate as closely as possible, using a scaled-down model, the performance of a full-scale flying aircraft, or part thereof. The wind tunnel is designed in such a way as to produce a flow field that is well behaved and predictable, thereby allowing the performance of a test model to be accurately observed and quantified. The more closely the full-scale effect is simulated, the greater will be the predictive capability of the wind tunnel data. Rae and Pope[6] give a good overview of many relevant topics in low speed wind tunnel testing.

3.1.1 Types of Wind Tunnels

There are two types of low speed wind tunnels, the open circuit or non-return tunnel (also called Eiffel or NPL type), and the continuous circuit or closed-return tunnel (also called Prandtl or Göttingen type).[6] As the name implies, the open circuit tunnel is open to the atmosphere, or a room, at both its inlet and its exit. The continuous circuit tunnel has a set of corners and ducts that return the air from the test section exit to the test section inlet.

3.1.1.1 Open Circuit Tunnels

Figure 3.1 shows schematically the layout of a simple open circuit wind tunnel. Air enters the tunnel via an inlet contraction, the purpose of which is to accelerate the airstream smoothly to high speed before it enters the test section. The model is positioned in the test section, the airflow passing over it being observed and its effect on the model measured. After leaving the test section, the airflow is decelerated by the diffuser, after which it passes through the tunnel drive fan. The tunnel consumes the least power if the velocity of the air

leaving the tunnel it is kept to a minimum, hence the need for the diffuser. The open circuit tunnel has several inherent advantages and disadvantages.[6]

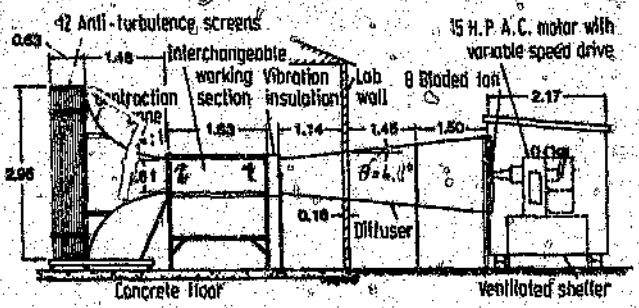

Figure 3.1: Open circuit tunnel.[6]

Advantages

1 Lower construction cost.
2 The required floor space is less.
3 If flow visualization using smoke is done, there is no purging problem.

Disadvantages

1 Depending on the size of the tunnel and the room it is situated in, the inlet may require screening to get high quality flow.
2 For a given size and speed, the tunnel will require more power to run.
3 The tunnel noise level is high since the tunnel is open at both ends.

3.1.1.2 Continuous Circuit Tunnels

Figure 3.2 shows schematically the layout of a continuous circuit wind tunnel. The continuous circuit tunnel also has a contraction, test section, diffuser and drive fan, but in addition to these, a series of ducts and corners guide the air leaving the drive fan back to the contraction. The closed circuit tunnel also has very distinct advantages and disadvantages.[6]

Advantages

1 Through the use of corner vanes and screens, the flow quality can be easily controlled.
2 For a given size and speed, the tunnel will require less power.

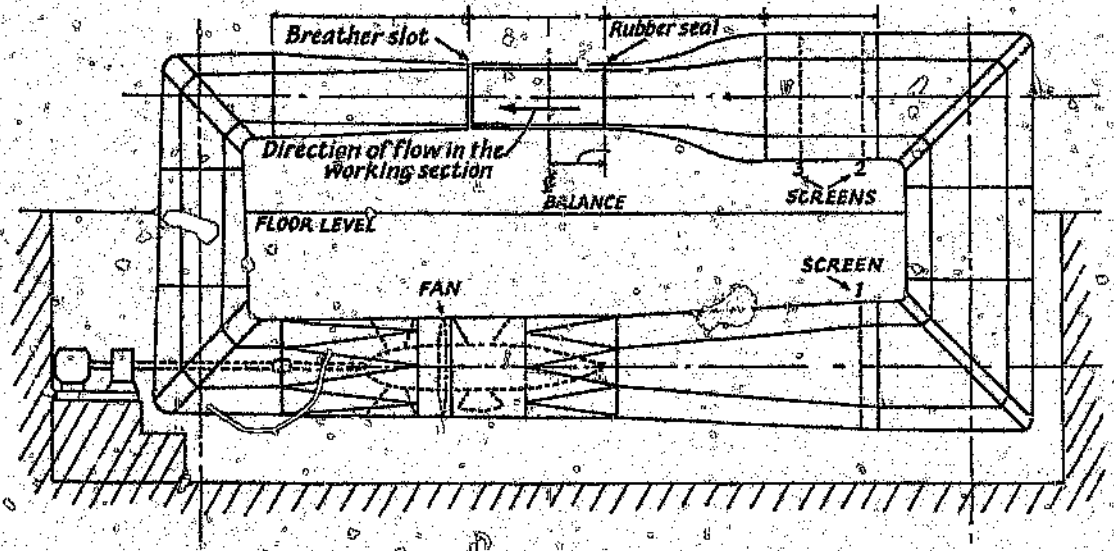

Figure 3.2: Continuous circuit tunnel.[24]

3 Since the tunnel is a closed circuit, it can be pressurized to achieve different flow characteristics.
4 The tunnel noise level is lower.

Disadvantages

1 Due to the extra corners and ducts, the construction cost is higher.
2 If extensive smoke tests are performed, the tunnel must be purged.
3 The tunnel may require cooling to counteract the increasing temperature of the confined tunnel flow.

3.1.2 Similarity Considerations

Generally, in order to simulate a full-scale aircraft aerodynamically, the model must be operated at the same Mach and Reynold's numbers.[6] This alone does not guarantee aerodynamic similarity, but is a good first step.

The Mach number of a flow is a measure of the ratio of inertial and elastic (or compressibility) forces of the flow. Since the drag, in particular, is strongly dependent on compressibility effects at speeds approaching that of the local sound speed in the fluid, matching the model and full scale aircraft Mach numbers is desirable.

The Reynold's number of the flow over an aircraft or component is a measure of the ratio of inertial and viscous forces, or in other words, the ratio of the importance of inviscid (far flow field) and viscous (boundary layer and wake) effects. Matching the Reynold's number of the model and the full scale aircraft is therefore also desirable.

From the above discussion it is evident that ideally one would like the model Mach and Reynold's numbers to be the same as those of the full-scale aircraft, but after brief consideration it is equally obvious that achieving this is not that simple. A large full-scale aircraft flying at a given speed would require a small model to be wind tunnel tested at a much higher speed, assuming that the kinematic viscosity of the fluid remains constant, or differs insignificantly. A higher speed in a fluid of equal kinematic viscosity implies a higher model Mach number.

For this precise reason, several modern wind tunnels can be pressurized (for increased density) and cooled (for increased density and decreased dynamic viscosity) in an attempt to alter the kinematic viscosity of the fluid in such a way as to allow an accurate matching of both Mach and Reynold's numbers.[6] This is however a costly affair, such tunnels only being used in cases where the absolute accuracy is of paramount importance, and where the cost of achieving this accuracy is warranted. Another approach is to use a fluid with a different kinematic viscosity, again with the objective of more accurately matching model and full-scale Mach and Reynold's numbers. Again, cost is the deciding factor since the tunnel has to be hermetically sealed, and may require more power for a given Mach and Reynold's number.

By definition, an incompressible flow is one with a Mach number of zero. Fortunately, if a model is tested at low Mach number, ie. $0 < M \leq 0.3$, compressibility effects will be negligible, and the flow will be essentially incompressible. It is therefore only necessary to attempt to match Reynold's number when performing tests on a model in an incompressible flow.

3.1.3 Two-Dimensional Testing

It is often necessary to test an aerofoil in conditions where there are only large scale pressure, velocity and directional changes of the flow in two directions. This condition can be achieved if a wing of constant section is allowed to span the

entire test section.[6] Although there may be 3-D (spanwise) flows in this situation, they will be small, and can either be ignored or dealt with separately.

Another approach is to use a wing of finite span, but with large end plates at either end to prevent 3-D flows.[6] If the end plates are sufficiently large, this method approaches a wing spanning the entire test section. This method is not often used because the drag of the two end plates is difficult to measure or establish, and thus the drag of the entire wing will have a degree of uncertainty.

A variation of the first method, ie. spanning the test section, makes use of 2-D test section insert, a special insert that allows a test section of small height to width ratio to be converted into one of large height to width ratio. Height to width (aspect) ratios of 8 or higher are typical for this type of 2-D testing technique.

3.1.4 Wind Tunnel Interferences

One of the early triumphs of the Lanchester-Prandtl wing theory was that it explained the effects of wind tunnel boundary interference, and provided explicit and simple formulae to correct wind tunnel measurements for these effects.

Rae and Pope[6] give a detailed account of the primary interferences encountered in conventional rigid wall wind tunnel testing. There are essentially 4 types of wind tunnel interferences encountered in 2-D aerofoil testing.

1 **Solid blockage**
Since the aerofoil occupies a portion of the available cross-sectional area of the test section, flow has to be deflected around the model. The straight tunnel walls restrict this displacement, leading to distortions of the flow field. To satisfy continuity within the confines of the tunnel walls, the flow generally moves faster than it should in the proximity of the model, causing lower pressures on the model surface to be experienced. Since the model has a boundary layer that is dependent on the pressure gradient impressed upon it, this layer will be distorted if the general pressure field is distorted. Generally, an increase in drag will be measured as a

result. If the model has areas of local flow separation on its rear surfaces (as is quite often the case with laminar aerofoils), complete pressure recovery will not be realized, resulting in a greater drag. Also, since the surface velocities of the model are increased, increased drag is experienced due to an increase in viscous shear stress.

2 **Wake blockage**

Any body that experiences drag will have a wake behind it, the wake being a region of lower average velocity than the freestream. To satisfy the law of continuity within the tunnel boundaries, the flow outside the wake must have a correspondingly higher velocity than the tunnel freestream velocity, giving rise to lower pressures over the rearward pprtion of the model. This manifests itself as an increase in the measured drag.

3 **Horizontal buoyancy**

The presence of a boundary layer along the walls of the test section displaces the inviscid test section flow, resulting in a decrease in available flow cross-sectional area for the inviscid flow, and hence by continuity, an increase of velocity along the test section length. This gives rise to a negative pressure gradient down the length of the test section, a grad nt which generates a rearward buoyancy (hence its name), or drag, on the model. Horizontal buoyancy can be alleviated by eliminating any longitudinal pressure gradients in the test section, this usually being done by tapering the test section, ie. increasing the cross-sectional area towards the rear of the test section to accommodate the boundary layer displacement thickness. Unfortunately, different boundary layer displacement thicknesses at various speeds require a different degree of taper for each tunnel speed, a situation that is difficult to achieve with a rigid test section.

4 **Streamline curvature**

A lifting aerofoil creates a curved flow field due to the superposition of a circulatory and a rectilinear flow field. Since the tunnel walls are straight and rigid, no streamline curvature can exist at the tunnel walls. As a result of this constraint, the flow field in the vicinity

of the aerofoil is also artificially straightened, leading to an apparent increase in aerofoil camber.

Tunnel blockage, wake blockage and streamline curvature effects can be reduced by increasing the ratio of test section frontal area and model frontal area. For a given tunnel, this implies a small model, and hence low model Reynold's number. Conversely, for a given model, a large tunnel is required, implying high capital and operating costs.

3.2 Adaptive Wall Wind Tunnels

3.2.1 Background

Discrepancies between tunnel data and measured flight data have accentuated the need for improved wind tunnel simulations.[7] At low subsonic speeds, wind tunnel data cannot be applied directly to full-scale flight conditions because of an inadequate Reynold's number simulation. Furthermore, the effects of test section boundary interference present a problem since a post-test analysis of measured data and the application of wind tunnel interference corrections is often unsatisfactory, particularly in the more interesting and challenging regimes of high-lift and V/STOL. An attractive wind tunnel testing option, which has recently been revived, is that of the adaptive wall test section. Such a test section allows wall boundary interferences to be either eliminated, or significantly reduced, by actively adapting the flow near the boundaries of the test section to match that of a free flow field.

The concept of a wind tunnel that does not affect the model being tested is not new, the idea being almost as old as the wind tunnel itself. The first adaptive wall wind tunnel was built by the National Physical Laboratory (NPL) in the UK in 1937[9], with the intention of overcoming severe transonic wall interference (ie. choking). Research done on that facility proved the viability of streamlining the flexible walls to minimize wind tunnel interference, despite the fact that streamlining the walls was a slow and tedious process due to the absence of computational facilities. While the original research into flexible walled test sections was driven by the need to overcome transonic choking, parallel research efforts were being pursued in other areas of high speed interference-free wind tunnel testing, culminating in test sections with ventilation. Since these sections were passive, they did not require the long wall

setting tunes of flexible walled test sections, and as a consequence became accepted as the norm for transonic testing.[9] The adaptive wall wind tunnel was rediscovered in the 1970's when the need arose for transonic wind tunnel data of higher quality. Due to the availability of cheap and fast computers, rapid wall streamlining could be achieved, thus allowing data free of boundary interference to be obtained.[7] Tuttle and Mineck[8] give a detailed bibliography of much of the work done on adaptive wall tunnels up to 1986.

3.2.2 Adaptive Wall Wind Tunnel Types

Two distinctly different adaptive wall wind tunnels have evolved, namely those with a ventilated test section and those with a flexible wall test section.[9]

3.2.2.1 Ventilated Wall Test Section

The actively ventilated test section is a development of the existing passively ventilated test section. This system employs a controlled inflow or outflow of fluid through the ventilated walls to adapt the test section flow field as shown in Figure 3.3.

Consider the flow field created by a 2-D aerofoil flying in a real fluid of unlimited extent as shown in Figure 3.4. The boundary conditions defining this flow are those imposed by the aerofoil's geometry as well as the far flow field, ie. the conditions of undisturbed stream flow far upstream and downstream, as well as those at great lateral distance from the aerofoil. Let the infinite flow field be considered in two parts, namely inside (region I), and outside (region II) of two imaginary parallel planes S, which do no intersect the boundary layer or wake of the aerofoil. Let the two flow situations which coincide at S, be considered separately.

Considering firstly the flow exterior to S, in region II, it can be shown that, at least in the inviscid-fluid approximation, the flow is fully defined if the direction of flow is known at S. Once the flow is fully defined, all other flow variables can be derived.

Considering the flow interior to S, in region I, it is obvious that the boundary conditions of I can only match those of II, where they meet at S, if the flow field is unconfined.

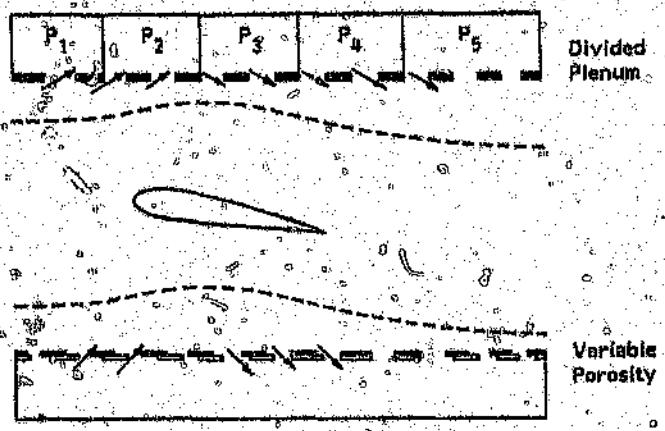

Figure 3.3: Ventilated wall test section.[9]

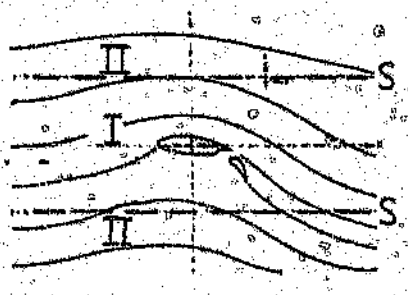

Figure 3.4: Unconfined flow about an aerofoil.[10]

The above discussion lends itself directly to a means of overcoming wind tunnel boundary interferences. If a wind tunnel has porous walls, the components of flow perpendicular to the walls can be adjusted in such a way as to eliminate boundary interference. This is done by computing the flow field exterior, and measuring the flow field interior, to S. The two flow fields can only match if they are identical, ie. if the interior flow field is unconfined. This is the method employed by amongst others, Sears[10] and Ferri and Baronti[11].

3.2.2.2 Flexible Wall Test Section

The flexible wall test section employs solid impervious, yet flexible, walls which adapt to the test section flow field by contouring as shown in Figure 3.5.

Considering a 2-D aerofoil in an infinite flow field as shown in Figure 3.6, it is evident that a streamtube can be formed by any two of an infinite number of streamlines. If the walls of a test section could be adapted to follow this streamtube, the test section boundary interference on the model would be eliminated provided that the streamtube was infinitely long and enclosed the model. At this condition, neglecting the wall boundary layer for

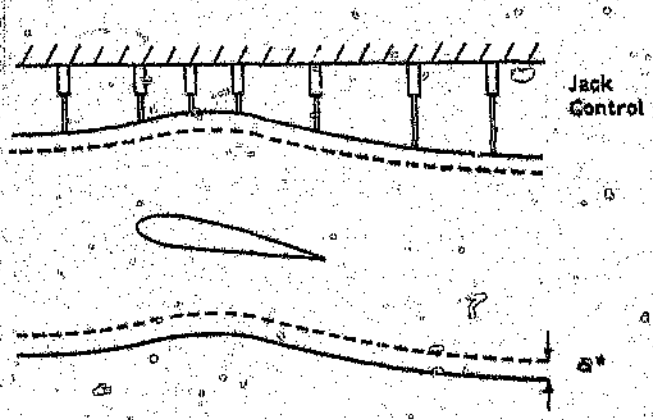

Figure 3.5: Flexible wall test section.

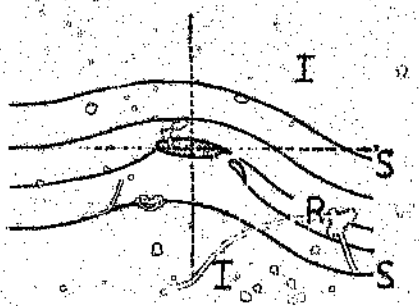

Figure 3.6: The principle of test section streamlining.

the moment, the walls of the test section could be viewed simply as substitutes for streamlines, and the walls are adapted to be streamlined. The shape of the streamlined walls would vary for different model speeds, loading and configuration, therefore the walls of such an adaptive wall test section would have to be flexible, but only in single curvature.

Let the infinite flow field be considered in two parts, namely inside (region R), and outside (region I) a streamtube which does not intersect the boundary layer or wake of the aerofoil.

Considering firstly the flow exterior to S, in region I, the flow is fully defined if the direction of flow is known everywhere along the wall. The flow now being fully defined, all other flow variables can be derived.

Considering the flow interior to S, in region R, it is obvious that the boundary conditions of R can only match those of I, where they meet at S, if the flow field is unconfined.

Again, the above arguments lead directly to a means of eliminating wall boundary interferences. If the flow exterior to S can be computed (this being relatively simple since the flow is inviscid), and the boundary variables of the flow interior to

S are measured, the two can only be matched if the interior flow field is unconfined. This method of adapting a test section has been used by, amongst others, Goodyer[2,13], Wolf[7,14] and Lewis[9].

3.2.3 Advantages of Adaptive Wall Tunnels

A properly designed adaptive wall wind tunnel will virtually eliminate wind tunnel boundary interferences, something which cannot always be achieved with a rigid wall tunnel. In addition to the elimination, or significant reduction, of boundary interferences, the adaptive wall test section has distinct advantages over conventional tunnels.[9]

3.2.3.1 Higher Reynold's Number

Eliminating wind tunnel boundary interference allows the test section height to be decreased, or the model size to be increased, both actions resulting in a reduction in the ratio of test section height to model chord (h/c). Conventional wind tunnels require large values of h/c to reduce the effects of boundary interference, thus the model is usually made significantly smaller than the test section. A small model necessarily implies a small Reynold's number for a given tunnel speed, flow density and viscosity, hence the Reynold's number capability of the tunnel is reduced.

3.2.3.2 Reduced Power Requirements

Normally, a large Reynold's number can be achieved by using a large model, but this requires a large wind tunnel to keep the boundary interference below acceptable levels. The adaptive wall wind tunnel allows large models to be tested in a small tunnel, therefore the maximum model Reynold's number can be exploited for minimum capital (depending on the added cost of wall control) and energy input. The importance of large test Reynold's numbers has long been recognised, but it has also become evident from recent research[10] that it is equally important to test the largest possible model, since this not only maximizes the Reynold's number, but also improves the accuracy of the model itself, resulting in a greater accuracy of the forces and moments measured in the wind tunnel. The latter argument lends itself most aptly to the use of adaptive wall tunnels since these allow the largest model to be tested in a given facility.

3.2.3.3 Rapid Data Availability

Since the data obtained from an adaptive wall wind tunnel is already correct, data processing time during test runs can be reduced. This is significant in real-time simulations where data can be used for further testing immediately.

3.2.3.4 Improved Flow Quality

Adapting the tunnel walls to emulate streamlines not only eliminates tunnel boundary interference, but also reduces secondary flows in the test section.[10] In 2-D aerofoil testing, a reduction of either the h/c ratio, or an increase in aerofoil aspect ratio, reduces the magnitude of secondary flows. Since the adaptive wall wind tunnel allows low values of h/c to be employed, wings of low geometrical aspect ratio to be used in testing that simulates aerofoils of infinite span.

3.2.3.5 Test Mode Versatility

Amongst others, Lewis[9] indicates that the adaptive wall wind tunnel allows six modes of operation.

1 **Closed Tunnel Mode**
This is the mode of operation of most rigid wall wind tunnels. The test section walls are straight and generate the flow field of an infinite array of images as shown in Figure 3.7.

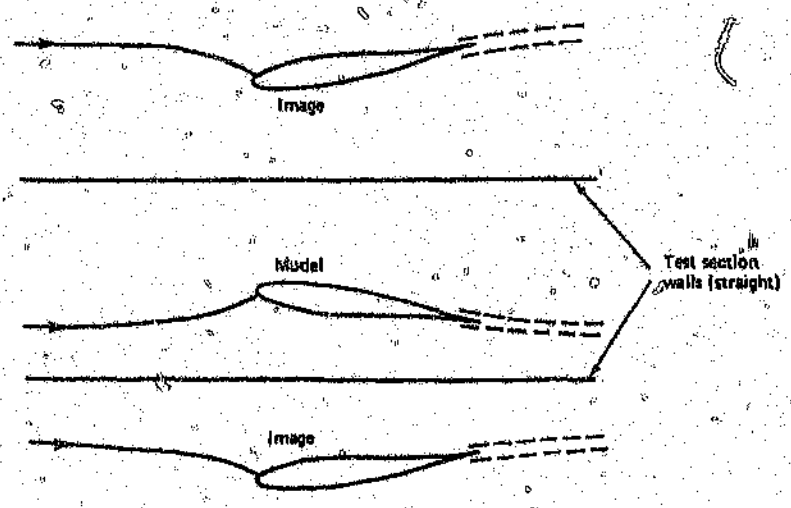

Figure 3.7: Closed tunnel mode.[9]

2 Open Jet Mode

This is the mode of operation of tunnels with an open, or free jet, as shown in Figure 3.8. The jet boundary is exposed to the atmosphere (or plenum chamber), and therefore experiences constant static pressure along its length.

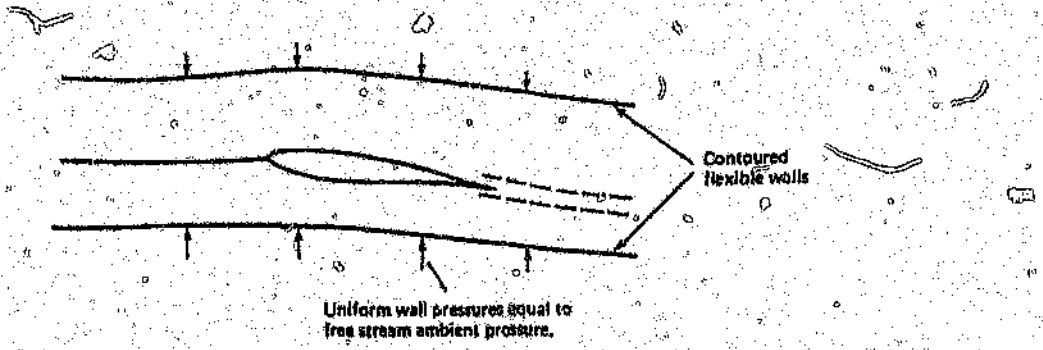

Figure 3.8: Open jet mode.[9]

3 Infinite Flow Field Mode

This is the most widely used mode of operation of the adaptive wall test section. The test section walls are contoured to emulate streamlines, yielding an infinite flow field, as shown in Figure 3.9.

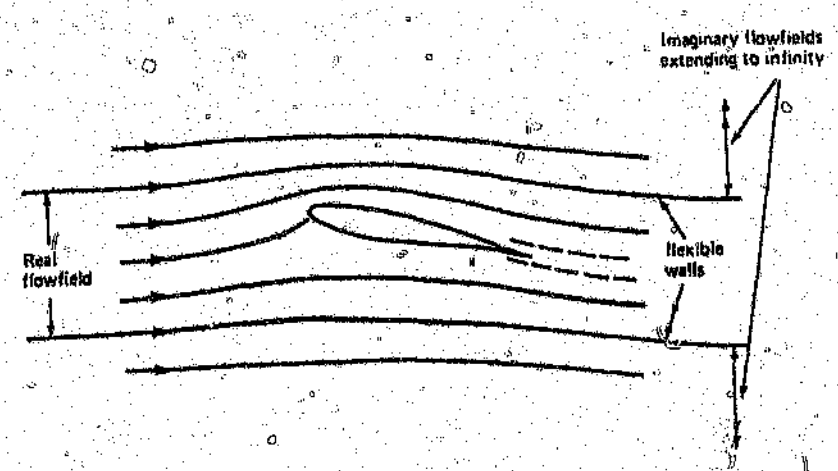

Figure 3.9: Infinite flow field mode.[9]

4 Ground Effect Mode

In ground effect mode, the flexible walled test section simulate a portion of the imaginary flow field generated by

a pair of models, one being the mirror image of the other, as shown in Figure 3.10.

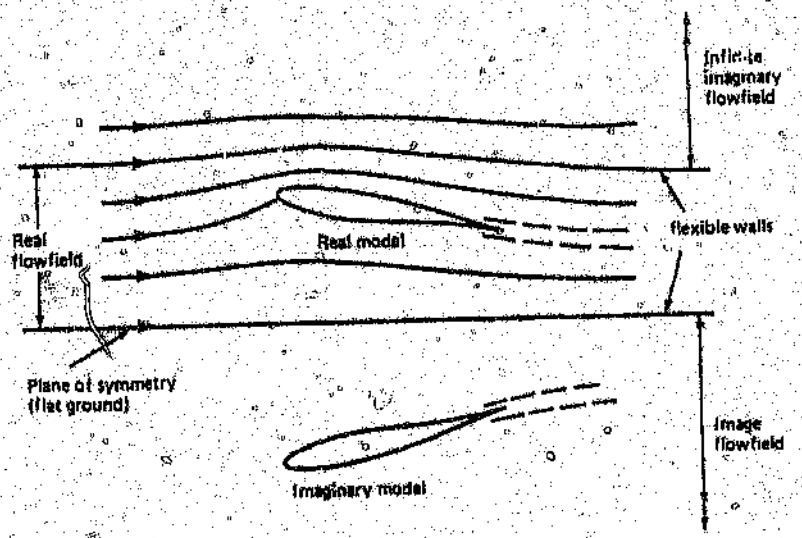

Figure 3.10: Ground effect mode.[9]

5 Cascade Mode

In cascade mode, the flexible walled test section simulates a portion of flow in an infinite cascade of aerofoils. Usually only one aerofoil is situated in the test section (to obtain maximum Reynold's number), the bottom and top walls being identical. The streamlining criterion of the walls is that they have the same shape and pressure distribution, as shown in Figure 3.11.

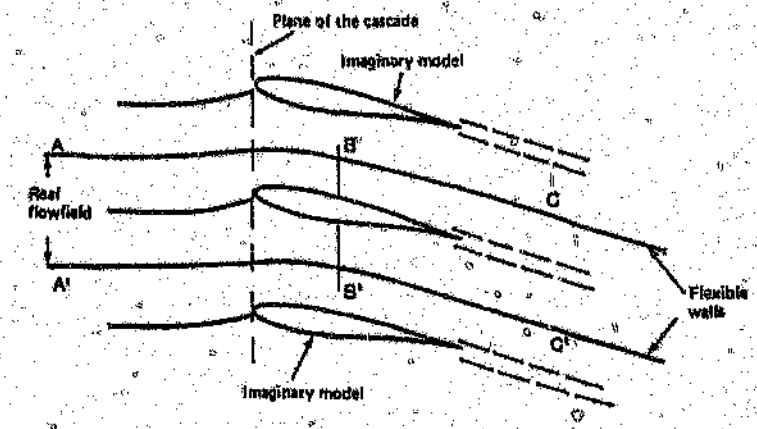

Figure 3.11: Cascade mode.[9]

6 **Steady Pitching Mode**

In steady pitching mode it is possible to simulate various rates of model pitch rate using a stationary model. The streamlining criterion is the same as for the infinite flow field mode, except that an additional curvature about the tunnel centreline is introduced to simulate a pitching motion, as shown in Figure 3.12. Although not perfect, this method very closely approximates the real flow field.

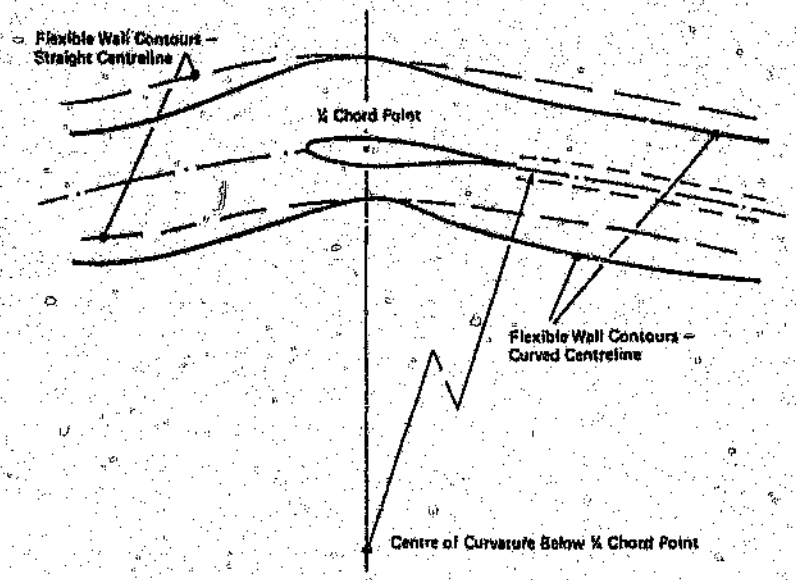

Figure 3.12: Steady pitching mode.[9]

3.2.4 Disadvantages of Adaptive Wall Tunnels

The adaptive wall wind tunnel also has some inherent disadvantages.[9]

3.2.4.1 Operational Aspects

Since the wall streamlining procedure is an iterative process, a large proportion of the available tunnel operating time is spent positioning the walls. This non-productive time can be reduced by using wall streamlining strategies with a higher convergence rate, or by structuring the tests in such a way as to require minimal wall movement from test to test.

3.2.4.2 Increased Cost and Complexity

The primary disadvantage of the adaptive wall wind tunnel is the added complexity and cost of flexible and continuously adjustable walls. Such walls require mechanical as well as electronic and

computer control, which adds to the capital contribution of the project costs. Future adaptive wall test sections may allow dynamic testing, and this will require even faster and more expensive control. However, if the walls are positioned to the mid-position of the dynamic mode, wall interference may prove to be minimal, and certainly less than in conventional tunnels.

3.2.5 Wall Streamlining Strategy

The success of any adaptive wall wind tunnel depends largely on the degree of certainty with which the walls can be positioned.[7] Data obtained from the tunnel can only be good if the flow field created by the tunnel approaches that of an unconstrained flow field, ie. a freestream. Several strategies have been proposed and tested, each with their own merits and shortcomings. The more generally accepted wall streamlining strategies are listed below.

3.2.5.1 The NPL Strategy

This approximate strategy was employed by NPL in the 1940's to allow transonic blockage to be reduced.[9] The method is based on the observation that corrections for boundary interference for open and closed test sections are generally of equal magnitude, but opposite in sign. It was later analytically confirmed that streamlines in an unconfined flow always lie approximately halfway between boundaries of constant static pressure (open test section) and straight boundaries (closed test section). The NPL strategy therefore required the walls to be laboriously set to satisfy the condition of constant wall pressure, after which the walls were moved to a position halfway between this position and the straight wall position, at which stage data could be acquired.

3.2.5.2 The Potential Flow Strategy

This strategy models the aerofoil by means of a doublet and free vortex in a potential freestream.[9] These two elementary flows allow the effects of size and lift to be modelled, a Zhukovsky transformation sometimes being used to give shape to the aerofoil. Since the tunnel walls are in the far (inviscid) flow field of the aerofoil, only pressure terms are relevant, these being well represented by the above model. Also, since the effect of the elementary flows is inversely proportional to the distance from their centres, the streamlines at the tunnel walls will change little if a system of distributed doublets and vortices is used to model the aerofoil. This strategy allows the walls to

be positioned immediately if lift values (from a previous data point) are known.

3.2.5.3 Self-Streamlining Strategy

The tunnel wall flow field (ie. an inviscid flow with a predictable boundary layer that can be accounted for) is modelled using a computational method. Since the position of the wall is known, an inviscid pressure distribution along the wall can be calculated. The actual wall pressures are then measured, and compared to the calculated values. The wall is correctly streamlined when the measured and calculated pressures are equal. This method is very attractive since it does not require any knowledge of the model being tested.[7] The accuracy of the streamlining procedure is, however, very sensitive to the accuracy of the wall position and pressure measurements. Due to the iterative nature of this strategy, considerable time is spent acquiring each data point. Modern computational methods, notably those introduced by Judd[15], have been developed which reduce the number of iterations from more than ten to less than two.

3.3 The CCTB Concept

As elucidated in Chapter 1, it is possible to use the tail boom of the conventional helicopter in a more direct and efficient way for the purpose of counteracting the main rotor torque. The tail boom of a conventional helicopter is usually a bluff body in cross-section, and in the presence of a large main rotor downwash experiences a negligible sideward force. Circulation control by blowing through tangential slots causes the tail boom to produce a usable sideward force, this being the underlying idea of the CCTB concept. The effect of CC on the tail boom is to keep the flow on the suction surface attached longer than would normally be the case, resulting in a circulatory flow about the cylinder. This circulatory flow leads directly to the production of a sideward force by the cylindrical tail boom.

The attachment of a jet to an adjacent convex surface is generally referred to as the Coanda effect[4], named after the Rumanian inventor who discovered it in 1910. It is worthy of mention that the effect was actually described by Young[16] as early as 1800, but was only thoroughly investigated almost a century later. The Coanda effect can be effectively employed in the generation of circulation around an aerofoil, resulting in a significant increase in lift.

3.4 Circulation Controlled Aerofoils

Nurick[4] gives a detailed account of the various analytical, computational and experimental methods employed to predict the behaviour of circulation controlled aerofoils. Only the more relevant experimental and theoretical work will be discussed in detail.

3.4.1 Analytical Methods

Dunham[17] developed a method to predict the lift generated by a CC circular cylinder. His method uses a potential flow analysis to predict the pressure distribution around the cylinder. A turbulent boundary layer calculation, based on Spalding's unified boundary layer theory, is then performed on the top and bottom surfaces of the cylinder to establish the point at which both separate. Thwaite's condition, ie. similar static pressures at the upper and lower surface rear separation points, is enforced to close the equations. Referring also to Figure 3.13, the actual procedure employed by Dunham is as follows.

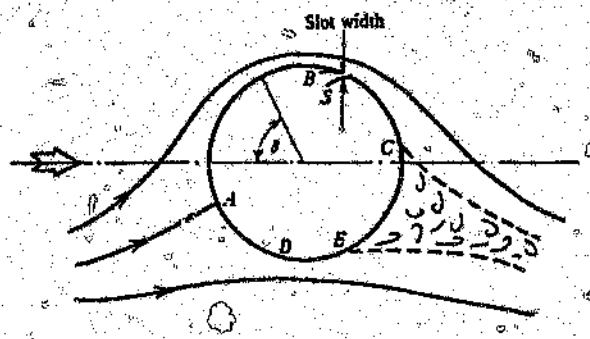

Figure 3.13: Dunham's CC cylinder (schematic).[17]

1. The lift coefficient is specified and the pressure distribution calculated.
2. Starting at the forward stagnation point (A), the lower surface laminar boundary layer (A-D), transition (D), and turbulent boundary layer (D-E) up to separation are calculated.
3. Starting at the forward stagnation point (A), the upper surface laminar and turbulent boundary layer, as well as the effect of the wall slot (B), is calculated. This step is repeated until the boundary layer separates at C with the same pressure as the lower surface boundary layer.

Dunham compared his theoretical predictions to his own experimental work, as well as work done by Jones and Buckingham[18], and Lockwood[19]. The various researchers used different ratios of slot thickness to cylinder diameter. Dunham used values ranging between 0.0017 and 0.0087, Jones and Buckingham used values between 0.005 and 0.01, and Lockwood used a single value of 0.001.

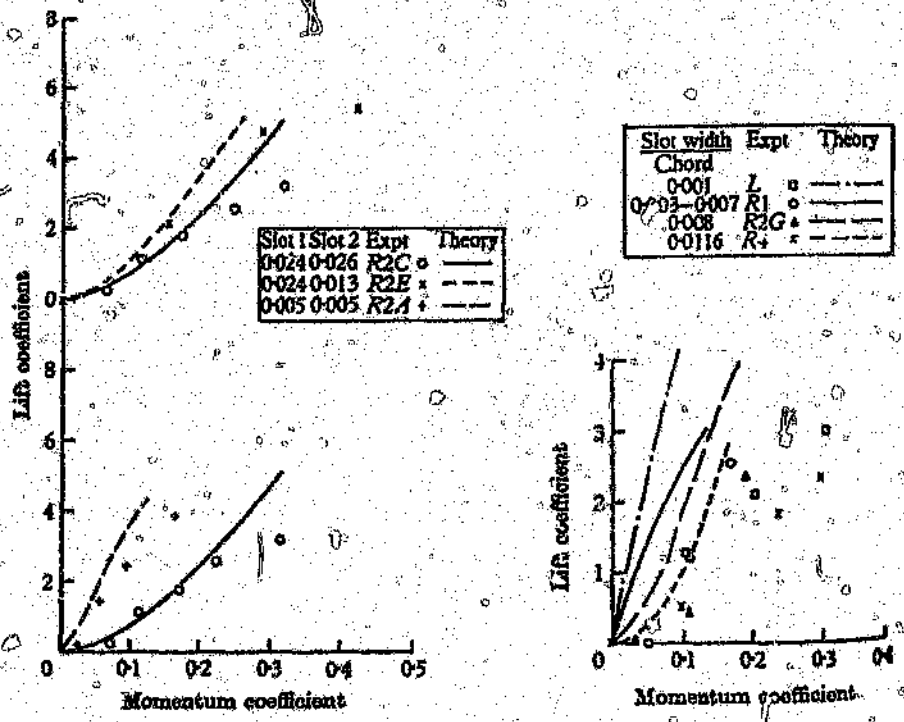

Figure 3.14: Effect of t/c on the variation of C_l with C_μ.[17]

Figure 3.14 shows some typical curves of C_l versus C_μ curves for different ratios of slot thickness to cylinder diameter (t/c). Whereas the experimental data suggests a square root type relationship between C_l and C_μ, it can be seen that the theory predicts something between a linear or a square relationship. It is evident that the theoretical predictions do not fit the data particularly well.

Sun, Pai and Chopra[20] developed a method to predict the aerodynamic forces on an elliptical CC aerofoil. Use was made of a potential flow model to determine the pressure distribution, including the effect of the separated wake, on the surface of the ellipse. The development of the boundary layer and wall jet was calculated using a finite difference method. An iterative technique combining the potential flow model and the boundary

layer calculation was used to determine the aerodynamic forces for a given jet momentum coefficient. The correlation between experimental results and theoretical predictions was not very good, as shown in Figure 3.15.

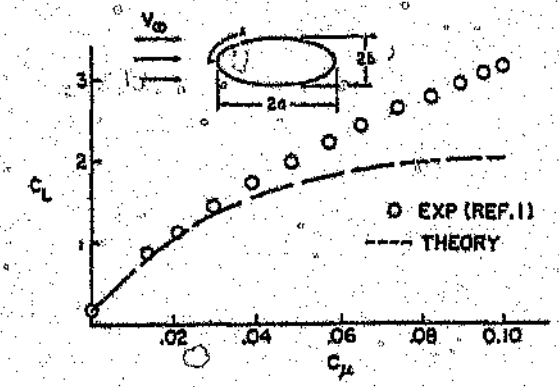

Figure 3.15: Variation of C_l with C_μ for an ellipse.[20]

3.4.2 Experimental Methods

The experimental work done by Lockwood[19] is by far the most comprehensive found, and will be dealt with in some detail since it provides many trends and starting points. Lockwood tested a single cylinder which had 8 equally spaced tangential surface slots spaced 45° apart. These slots could be opened or closed as desired to obtain a large number of slot configurations. The cylinder could also be rotated about its axis to increase the variation in slot positions. Lockwood used only one slot thickness ($t/c_o = 0.001$), which is quite small when compared to other CC research on cylinders.[17]

There is, however, one large difference between the work of Lockwood and the present CCTB research. Lockwood envisaged the use of CC to enable hypersonic aircraft to land and take-off at low speeds. This concept uses the long and slender aircraft fuselage as a high aspect ratio wing of large span at landing and take-off by slewing the wing perpendicular to the direction of flight. If sufficiently high lift coefficients, and lift to drag ratios, could be obtained, such a design could be quite effective. Since the space inside the fuselage would be needed to accommodate payload or fuel, the cross-section of the ducts supplying air to the blowing slots would have to be small compared to the fuselage cross section area. For this reason the air would be ducted at high pressure, ie. high density, resulting

in high slot velocities. Since it is the momentum of the ejected air which re-energizes the boundary layer, ejecting the air at high speed implies a low mass flow rate of, but unfortunately a large residual kinetic energy in, the blowing fluid. The slot thickness on Lockwood's CC model was very small (t/c = 0.001), and very high blowing momentum coefficients were used. It is therefore inevitable that the slot jet velocity of his tests was very high. The CCTB is essentially an empty duct, therefore the entire cross-section is available to transport air to the slots. The air is therefore ducted at low pressure, ie. low density, implying that the ejection velocity, and hence the residual kinetic energy in the slot-jet, is low.

Lockwood's main conclusions were:

1 Very high lift coefficients (up to 24) can be obtained.

2 The lift coefficient increases rapidly with increasing slot momentum coefficient at low momentum coefficients, but less rapidly at higher momentum coefficients. To illustrate the point, for a given configuration, at low slot momentum (C_μ = 0.15) C_l = 5, while at high slot momentum (C_μ = 6) C_l = 24.

3 For slots covering less than half the circumference of the cylinder, the slot positions greatly influence the maximum lift coefficient that can be attained.

4 For slots covering less than half the circumference of the cylinder, the trailing slot position was found to be most important factor as far as maximum lift was concerned. Maximum lift was obtained if this position was close to what would ordinarily be considered to be the trailing edge of the cylinder. Moving the trailing slot further back results in a rapid loss of lift.

5 For a large number of slots distributed almost completely around the cylinder, the maximum lift attained was low.

Figure 3.16 shows one of Lockwood's more successful slot configurations. It can be seen that one of the curves exhibits a very high maximum lift coefficient, but also require a high blowing momentum coefficient.

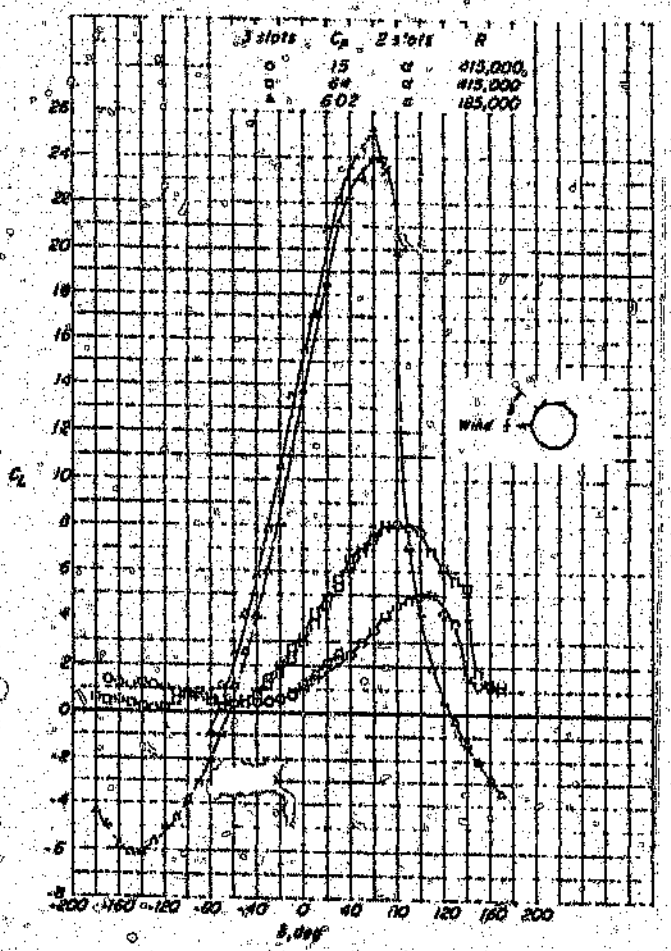

Figure 3.16: C_l vs C_μ. Cylinder with 2 slots 90° apart.[19]

4 Design of Equipment

A significant amount of equipment was developed for the purpose of testing high lift circulation controlled aerofoils not subject to wind tunnel boundary interference effects. Since the design of each component is intrinsically linked to its function, the two aspects will be dealt with concurrently. The design and description of equipment can be divided broadly into the following areas.

1 Description of adaptive wall wind tunnel.
2 Wind tunnel calculations.
3 Circulation controlled cylinder, balance and air supply.
4 Data acquisition and control system.
5 Software.

Figure 4.1 shows a schematic plan and side view of the wind tunnel. This figure will help to clarify photographs of the tunnel.

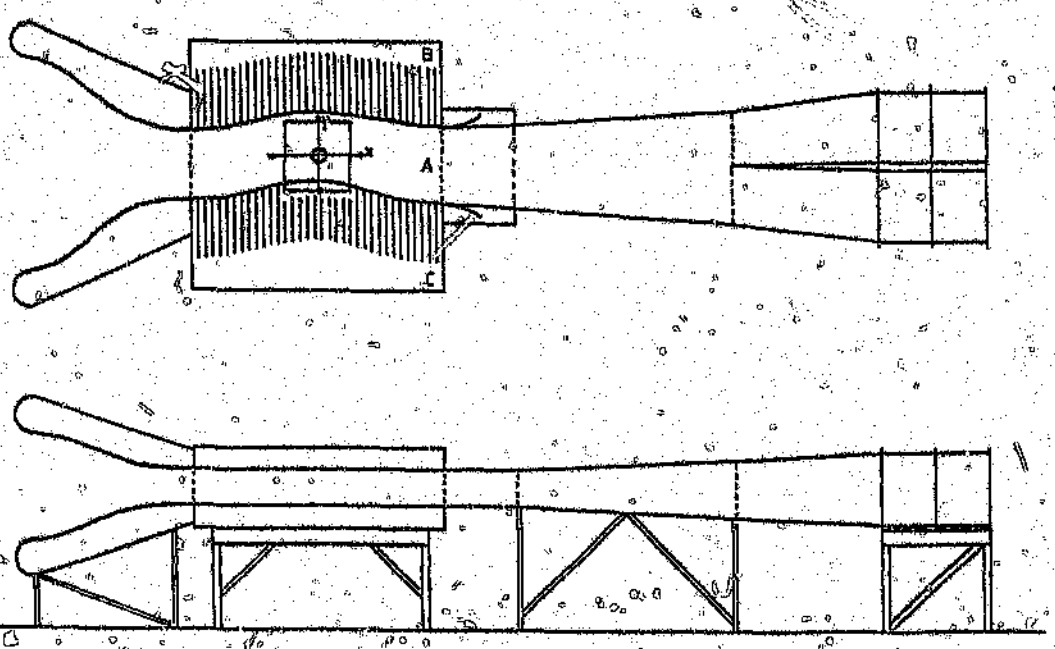

Figure 4.1: Plan and side view of the adaptive tunnel.

The wind tunnel was designed to a large extent using the methods outlined by Rae and Pope[6]. The adaptive wall test section required additional design, and use was made of design recommendations by Wolf[7].

4.1 Description of Wind Tunnel

The complete wind tunnel, viewed obliquely from in front and behind, is shown in Plate 4,1 and Plate 4,2. The various wind tunnel components and mechanisms will be discussed in detail, moving from the front of the tunnel to the rear.

4.1.1 Inlet Contraction

The purpose of the inlet contraction is to accelerate stationary, or slow moving, flow uniformly to the test section velocity. Flow entering the test section should have constant static and dynamic pressure across the test section, ie. constant total pressure. In addition, the process of accelerating the flow should involve as few losses as possible. Since the flow is accelerating, it generally experiences a favourable pressure gradient, reducing the possibility of flow separation. However, local flow separation can occur if there are regions of discontinuous curvature on the inlet surface profile, or if a severe adverse pressure gradient is encountered. Such flow separation will prevent constant dynamic pressure from being achieved across the test section.

Rae and Pope[6] give various guidelines for the design of axi-symmetric contractions, but these are not directly applicable to the case of a rectangular cross-section. Since no design guidelines could be found for rectangular sections, it was decided to use the inlet profile of another wind tunnel having a similar test section aspect ratio. A suitable inlet, namely that of a boundary layer investigation rig, was found and copied.

The inlet contraction consists of an internal wooden frame made up of streamwise profiled ribs and perpendicular stringers. This structure is covered on the inside and the outside by a masonite skin, which forms the smooth surface required on the inside of the contraction. The inlet is supported on a tubular steel space frame. Plate 4,1 shows a view of the inlet contraction and its supporting frame.

4.1.2 Inlet Honeycomb

A 150mm thick slab of aluminium honeycomb material can be inserted between the inlet contraction and the test section inlet, to reduce flow angularity and transverse velocity variations. The honeycomb is housed in a wooden holder, and can be easily be removed from the tunnel. Another separate 'dummy'

holder without honeycomb can be inserted, thus allowing the tunnel to be run either with or without honeycomb flow straightener between the inlet contraction and the test section. Running the tunnel without honeycomb allows a low tunnel turbulence level to be achieved due to the large contraction ratio of the inlet contraction. Running the tunnel with honeycomb yields straight flow, but at the cost of increased tunnel turbulence and decreased tunnel speed. Plate 4,3 shows the test section inlet with its two (honeycomb and 'dummy') removable honeycomb holders.

4.1.3 Test Section

The test section is essentially a large box housing 52 actuator driven slides, as well as two flexible sheet metal side walls, between two plane and parallel top and bottom walls. Figure 4.1 shows a plan view of the test section, and indicates how the 52 slides and flexible side walls are employed to achieve a continuous and variable flow channel, designated A. The flexible side walls are not physically attached to the slides, instead they are held against the slides by a pressure difference across the walls. This pressure difference is achieved by pumping air out of regions B and C such that the pressure in these regions is lower than that in region A. The test section height is a constant 0.5m throughout, while the entrance and exit widths are fixed at 1.1 and 1.1m respectively, allowing the test section to be positioned between a rigid inlet contraction and diffuser. The slope (in the X-Y plane) of the side walls at the test section inlet and exit is zero, thus any side wall shape satisfying the conditions of inlet and exit width and slope is allowable.

The test section outer shell consists of rigid top, bottom, front, rear and side walls. The outer shell is sufficiently stiff to support the large suction forces generated inside the test section by both the test section flow and the flexible wall suction.

4.1.3.1 Rigid Top and Bottom Walls

The test section top and bottom walls are supported by a laminated pine beam superstructure, which gives them the required stiffness to withstand the large pressure loads created by the test section flow, as well as the flexible side wall attachment scheme. Plate 4,4 shows a side view of the test section, revealing the laminated pine beam superstructure above and below

the test section, as well as the outer side walls.

The test section top and bottom walls have large windows (900mm by 900mm) in their centres, allowing optical measurements (LDV) and observations (smoke, tufts etc) of the model, as well as its far flow field, to be made. Details of the structural analysis performed to determine the stiffness of the top and bottom walls can be found in Section 4.2.2.

4.1.3.2 Flexible Side Walls

The flexible side walls are made of 0.8mm galvanized steel sheet. The side walls are rigidly attached to the test section at its inlet, and are able to slide in curved pockets at the test section exit to accommodate changes in arclength of the side walls. The side walls are pressure tapped along their centre-lines at intervals of 250mm, with a total of 12 pressure tappings per wall. The pressure tappings have a orifice diameter of 1mm, and a volute diameter and depth of 5mm and 3mm respectively. Silicone tubing, with a nominal internal diameter of 1mm, running towards the test section inlet transfers the pressure of each tapping to a multi-tube alcohol manometer. The top and bottom edges of the flexible walls are sealed by means of triangular-section foam strips, which also prevent the sheet metal side walls from scraping the wooden floor and ceiling of the test section. Plate 4,5 shows the (straight) flexible walls as well as the triangular corner strips.

4.1.3.3 Slides

The slides are amongst the more important parts of the adaptive wall test section. There are two types of slides, 26 short ones capable of 300mm of movement, and 26 longer ones which move up to 400mm. The short slides are found in region B of Figure 4.1, while the longer slides are found in region C. Plate 4,6 shows one of the shorter slides, with its accompanying actuator.

Each slide is guided by two teflon rollers on its bottom edge, as well as a slot in its top edge. The rollers run on profiled aluminium tracks in the test section, while the slot in the top edge is guided by a tubular steel rail. The front end of the slide, ie. that portion in contact with the flexible wall, is radiused to accommodate changes in the side wall slope, as well as being recessed at its centre to provide space for the pressure tapping tubing. Attached to the rear end of the slide is the

actuator leadscrew nut. The nut is adjustable in the vertical direction, allowing vertical misalignment between the actuator and the slide to be accommodated.

4.1.3.4 Actuators

Plate 4,7 is a view an actuator. The actuator consists of a back plate, a drive motor, a bearing and coupling, a leadscrew, as well as a potentiometer. Each actuator back plate is bolted to the outside of one of the rigid side walls of the test section via horizontal slots. These slots allow horizontal misalignment between the actuator and its accompanying slide to be accommodated. The actuator drive motor is also attached to the back plate, making each actuator a single unit with its own motor, leadscrew, potentiometer and attachment plate.

The electric drive motor is a 12VDC automobile windscreen wiper motor. These motors have a worm reduction gearbox which yields a high output torque at low rotational speed (typically 1 Hz). Each motor draws between 1A and 2A to overcome the mechanical resistance of the actuator.

The actuator bearing, coupling and leadscrew are also shown in Plate 4,7. A bearing is formed by the shoulder of the coupling and the actuator back plate. Two locking nuts allow the axial play of the bearing to be adjusted. A dog-clutch coupling allows for radial and axial misalignment between the drive motor and the back plate bearing. The leadscrew is a M20 threaded rod and has a pitch of 2.5mm.

The potentiometer allows the axial position of the slide to be determined. A worm reduction gear (45:1 and 60:1 for short and long slides respectively) converts the rotary position of the leadscrew to the 3-turn range of the potentiometer. The potentiometer is spring loaded onto the leadscrew to eliminate backlash. Due to its design, axial play in the actuator bearing does not affect the potentiometer. Axial backlash between the leadscrew and slide's leadscrew nut is not a problem since the slide only experiences wall suction forces in one direction.

4.1.3.5 Actuator Power Supplies

Four 220VAC/12VAC transformers are used to supply current to the 52 actuators. The output of the transformers is rectified, and then smoothed by means of two 4,7mF capacitors. Each actuator is

controlled by two relays, ie. one for on/off, and one for forward/backward. These relays are controlled by the PC via an I/O card and solid-state Darlington relay amplifier circuits. Plate 4,4 is a side view of the test section and clearly shows the power supplies and relay boards.

To overcome a hunting problem with the actuators, the 12VDC power supply is only used to move the slides to a position close to the desired position. A 6VDC power supply then moves the slides to their final positions. The 6VDC supply is obtained by passing the 220VAC input to the 4 transformers through a 220VAC/110VAC transformer. The current drawn by the motors is similar at 12VDC and 6VDC, therefore there is no danger of burning the transformers out by reducing the input voltage from 220VAC to 110VAC.

4.1.3.6 Wall Suction Fan

A small centrifugal fan is used to position the flexible test section walls firmly onto the front edge of the slides. The fan has a maximum operating pressure of 1000 Pa, which is sufficient to deform the flexible walls in small curvature, but insufficient to cause excessive waviness in the wall. The structural analysis presented in Section 4.2.2 shows that a maximum wall waviness of 75 microns is caused by a pressure differential of 1000 Pa across the wall. The fan has a sufficiently large flow rate capacity to enable the walls to be sucked into position very rapidly, in the order of 1 second. The fan exhaust is ducted back into the wind tunnel at the diffuser inlet, thus the fan merely maintains a constant differential pressure across the walls, and does not have to account for the change in test section pressure at different tunnel speeds. The exhaust air is ejected into the diffuser in the streamwise direction by ejector nozzles. The wall suction fan pressure and flow rate characteristics can be found in Appendix D3.

4.1.4 Exit Honeycomb

Honey comb material can be inserted between the test section and the diffuser in exactly the same fashion as with the inlet honeycomb. This is done to ensure that swirl effects, caused by the fans, do not propagate upstream into the test section. The tunnel also has a 'dummy' rear holder, thus allowing the tunnel to be run without the rear honeycomb in position. Again, when using the rear honeycomb, the tunnel speed is reduced.

4.1.5 Diffuser

The purpose of the diffuser is to slow down the high speed test section flow before it enters the fans. As the flow is slowed down, its pressure increases, thus the flow experiences an adverse pressure gradient. Flow separation is possible if the adverse pressure gradient is too steep. The optimum diffuser therefore slows down a given flow in the shortest distance, with the greatest pressure recovery. Rae and Pope[6] recommend an equivalent conic diffuser half angle of 5°. This means that the rate of change of cross-section area with axial distance of the diffuser should be the same as that of a cone with a half angle of 5°. Details of the diffuser design are given in Section 4.2.1.4.

4.1.6 Control Room

The tunnel control room is situated in the empty space below the diffuser. Plate 4,8 shows the PC that controls the tunnel (on the left) as well as another PC and some power supplies. The tunnel is normally operated from the control room, the operator only having to leave the room to make adjustments to the model.

4.1.7 Tunnel Drive Fans

Four 38 inch diameter Woods Aerofoil Fans (General Electric Company) are used to power the wind tunnel. The three-phase electric fans operate at 380V and 29A, giving a maximum power rating of 21 BHP each. The fans are arranged into two side-by-side contra-rotating tandem pairs, a configuration that allows the swirl at maximum power to be minimized.

The tunnel is usually run using only the two front fans, but for increased power, the two rear fans can also be switched on. A frequency inverting speed control system allows the angular velocity of the two front fans to be continuously varied between 0 and 100% of their maximum speed, whereas the two rear motors are switched directly on line. This combination of electrical connection allows the speed range of the tunnel to be continuously varied between 0 and 100%. This is achieved by varying the tunnel power from 0 to 50% using only the front motors, and then switching on the rear motors to achieve the remaining 50 to 100% variation in the tunnel power. Pressure verses flow rate characteristics for the contra-rotating tandem combination, as well as the single fan, are given in Appendix D1.

4.2 Wind Tunnel Calculations

The calculations used to determine the size and power requirements of the tunnel are discussed first, followed by a short structural analysis of the critical tunnel components.

4.2.1 Tunnel Power and Size

The design of wind tunnels is generally dictated by two mutually contradictory factors, namely, the size of test section required and the financial resources available. Since the tunnel drive fans usually make up a large portion of the cost of building the tunnel, the tunnel power is usually limited by the funds available. For this particular project the fans were donated, therefore the available tunnel power was not a variable. The only real variables were the test section size and speed, again two mutually contradictory quantities.

Low speed wind tunnel tests are performed at a low test Mach number, but in order to simulate full-scale effects properly, a high Reynold's number capability is required. Rae and Pope[6] recommend a tunnel size and speed that will produce a model Reynold's number per foot (approximately 0.3m) of over 10^6. For air at ambient pressure and temperature this Reynold's number corresponds to a tunnel speed of 60 m/s. At this speed the Mach number is approximately 0.2, which will make the flow virtually incompressible. The tunnel size was thus chosen so that the tunnel could achieve a speed of over 60 m/s with the available power.

The energy ratio (ER) of a wind tunnel is defined as the ratio of the energy of the air at the jet to the input energy. This ratio typically has values ranging between 3 and 7, indicating that the amount of stored energy in the airstream is considerably greater than the input energy for any given time interval. It is desirable to obtain as high an energy ratio as possible, since this implies a minimum power input for a given tunnel speed and cross-section area. The tunnel energy ratio is given as

$$ER_t = \frac{(qAV)_t}{\eta P} \qquad (4.1)$$

where q = dynamic pressure of the jet, A = jet area, V = jet velocity, η = fan efficiency, P = input power and the subscript t refers to the test section.

4.2.1.1 Tunnel Losses

Using the method by Wattendorf as outlined in Rae and Pope[6], the static pressure loss in each section of the wind tunnel can be estimated. The tunnel is assumed to have a circular cross-section, the equivalent circular area at each section of the generic tunnel being the same as the area at each station in the actual tunnel. The coefficient of loss is defined by

$$K_0 = \frac{\Delta p}{q} \frac{q}{q_0} \qquad (4.2)$$

where Δp is the local static pressure loss, q is the local dynamic pressure and q_0 is the dynamic pressure of the jet.

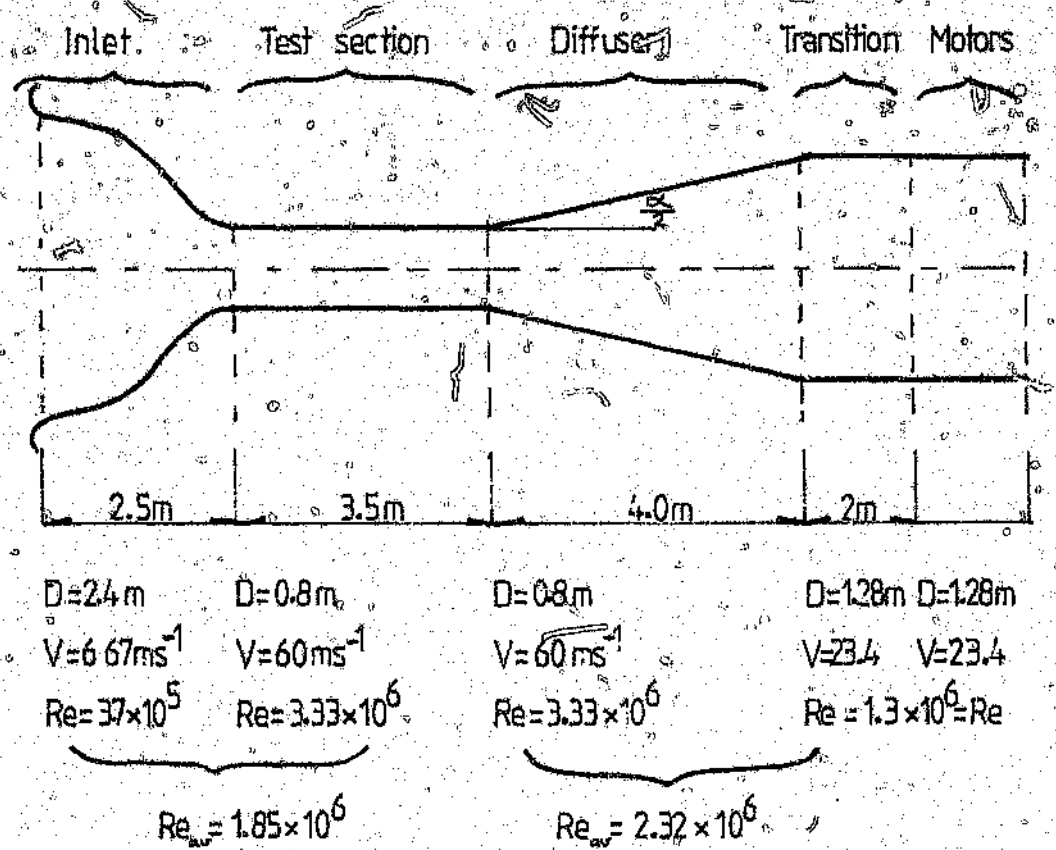

Figure 4.2: Schematic diagram of the generic tunnel.

Figure 4.2 shows a schematic representation of the generic tunnel having the same relevant dimensions as the actual adaptive wall tunnel. The diagram gives the equivalent diameter as well as the Reynold's number per metre (based on a jet velocity of 60 m/s)

at the each interface between tunnel components.

4.2.1.2 Inlet Contraction

The losses in the contraction are assumed to be caused only by skin friction, this being reasonable since large scale separation (and hence pressure losses) will not occur. A simplified form of the loss coefficient is given by

$$K_0 = 0.32\lambda\frac{L_c}{D_0} \qquad (4,3)$$

where λ is the skin friction coefficient based on Reynold's number, L_c is the contraction length and D_0 is the equivalent jet diameter. Using the average of the contraction inlet and exit Reynold's numbers, ie. 1.85×10^6, yields $\lambda = 0.0105$ from Figure 4.3.

$$K_0 = 0.32\times0.0105\frac{2.5}{0.8} = 0.0105 \qquad (4,4)$$

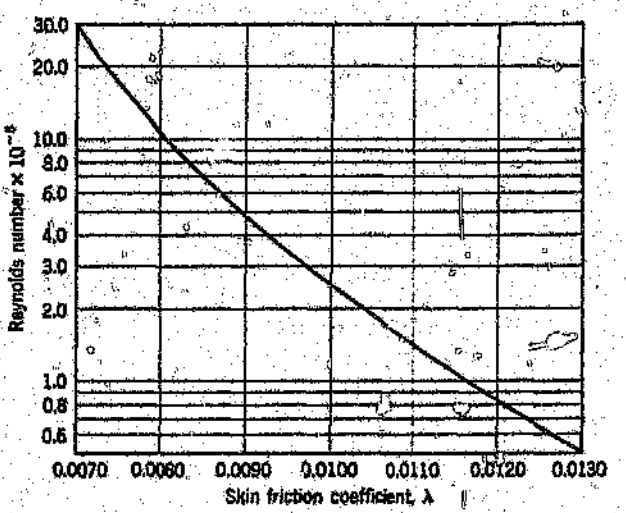

Figure 4.3: Skin friction vs Re.[6]

4.2.1.3 Test Section

The losses in the test section are purely frictional since there are no longitudinal pressure gradients. For smooth pipes the loss coefficient is given by

$$K_0 = \lambda \left(\frac{L_t}{D_0} \right) \qquad (4,5)$$

where L_t is the test section length. Using an average Reynold's number of 3.33×10^6 yields $\lambda = 0.0095$ from Figure 4.3.

$$K_0 = 0.0095 \times \frac{3.3}{0.8} = 0.0416 \qquad (4,6)$$

4.2.1.4 Diffuser

The losses in the diffuser are due to friction as well as expansion. The combined loss coefficient is given by

$$K_0 = \left(\frac{\lambda}{0.8 \tan(\alpha/2)} + 0.6 \tan(\alpha/2) \right) \left(1 - \frac{D_0^4}{D_2^4} \right) \qquad (4,7)$$

where $\alpha/2$ is the diffuser half-angle and D_2 is the diffuser exit equivalent diameter. Using an average Reynold's number of 2.32×10^6 yields $\lambda = 0.01$ from Figure 4.3.

$$K_0 = \left(\frac{0.01}{0.8 \times 0.06} + 0.6 \times 0.06 \right) \left(1 - \frac{0.8^4}{1.28^4} \right) = 0.207 \qquad (4,8)$$

4.2.1.5 Transition

Using the same loss coefficient equation as the test section, the losses in the transition from square to round are purely frictional, and given by

$$K_0 = \lambda \frac{L_{tr}}{D_0} \qquad (4,9)$$

where L_{tr} is the transition length. Using an average reynold's number of 1.3×10^6 yields $\lambda = 0.011$ from Figure 4.3.

$$K_0 = 0.011 \times \frac{2}{0.8} = 0.0275 \qquad (4,10)$$

Using the definition of K_0 from equation 4.2, it can be shown that

$$ER_t = \frac{1}{\sum K_0} \qquad (4,11)$$

It is now possible to sum the losses in the tunnel, and hence calculate the tunnel energy ratio.

$$ER_t = \frac{1}{\sum K_0} = \frac{1}{0.2867} = 3.5 \qquad (4,12)$$

The tunnel energy ratio allows the power input to the tunnel to be calculated.

$$ER_t = \frac{(0.5\rho V^2 A W)_t}{\eta P} \qquad (4,13)$$

There are two fans with 21 BHP motors each, providing a total of 31.3 kW. Assuming $\rho = 1$ and $\eta = 0.7$, and using ER = 3.5, the jet velocity is found to be 67 m/s.

There is therefore sufficient power to run the tunnel up to speeds of 65 m/s. In fact, basing the local Reynold's number on a jet velocity of 60 m/s as done above, will result in loss coefficients that are larger than they should be. The above analysis therefore errs on the safe side. The error is however small since the skin friction coefficient, λ, is not very sensitive to relatively small changes in Reynold's number. The argument is further reinforced by the fact that the tunnel energy ratio is not a function of jet velocity or Reynold's number, only the tunnel geometry.

4.2.2 Structural Considerations

Being an open circuit tunnel with its fans situated at the tunnel exit, the static pressure within the tunnel is smaller than atmospheric pressure at all stations. In regions where the air velocity is high, considerable pressure loads are imposed on the tunnel top, bottom and side walls, and since these loads are directed inwards, away from any support structure, the structural design is more critical. The structural design is dictated primarily by stiffness considerations, strength limits rarely being reached.

Apart from the tunnel drive fans, the test section is the only portion of the wind tunnel that has moving parts, ie. the actuator slides and flexible walls. For this reason the test section outer shell must be sufficiently stiff so as not to interfere with the movement of the mechanisms inside it. The structural analysis therefore dealt exclusively with the deflections of the test section since this was the most critical section of the wind tunnel. Aspects covered were the stiffness of the test section beam superstructure, the stiffness of the test section ceiling and floor panels as well as the waviness of the flexible test section side walls.

For a maximum pressure loading of 5000 Pa, corresponding to a tunnel speed of 100m/s, a maximum deflection of the test section superstructure of 0.044mm was obtained. Subject to the same loading, the floor and ceiling panels have a maximum deflection of 0.12mm. If the flexible walls are sucked onto the actuator slides by a pressure differential of 1000 Pa, the maximum waviness in the flexible wall is 0.075mm. It can therefore be seen that the deflections of the test section walls are negligible when compared to the test section dimensions. Numerical details of the structural analysis can be found in Appendix C.

4.3 Model and Balance

4.3.1 Model

The 200mm diameter circulation controlled cylinder has four longitudinal slots, positioned 70°, 105°, 140° and 175° from the cylinder leading edge. The slots eject fluid tangentially onto the circular surface, and are individually adjustable from 0mm to 5mm. The adjustment of each slot is effected by opening the slot to the desired gap width, and then tightening a draw-bar, allowing the slots to be adjusted accurately and swiftly. Plate 4.9 and Plate 4.10 show the cylinder with its adjustable slots, as well as its location with respect to the wind tunnel balance.

Air is supplied to the slots via a perforated inner cylinder, which in turn obtains its air supply from the balance. The perforated inner cylinder also transfers the mechanical loads from the model to the balance. The longitudinal velocity component of the fluid ejected from the slots is kept to a minimum by the straightening effect of the six bulkheads which

connect the model outer surface to the perforated cylinder. The above consideration is important since any longitudinal flow component in the ejected fluid will make the flow field around the model less two-dimensional.

4.3.2 Balance

A two-component balance supports the model in the test section and allows the lift and drag forces experienced by the model to be measured. A side view of the balance is shown in Plate 4,11. The flexures of the balance are designed in such a way as to allow only movement in the lift and drag directions. Load cells restrict this movement, therefore lift and drag are measured directly. The load cells are rated to a maximum load of 3000N in the lift direction and 1500N in the drag direction.

4.3.3 Circulation Control Air Supply

A medium pressure centrifugal fan is used to supply circulation control air to the model. The fan is powered by a 7,5 kW three-phase induction motor, and can supply a volumetric flow rate of 0.5 cubic metres per second at 7,5 kPa. Since the fan motor speed is constant, variations to the output flow rate and pressure of the fan are achieved by throttling the downstream side of the fan by means of an integral discharge damper. Plate 4,12 shows the circulation control blower with its discharge throttling valve. Pressure verses flow rate characteristics for the fan are given in Appendix D2.

4.3.4 Orifice Plate

A D, D/2 orifice plate, designed according to BS 1042[25], is situated 5m downstream of the CC blower, and is used to measure the flow rate of air entering the CC aerofoil. There are two orifice diameters, namely 100mm and 125mm, which can be selected depending on the flow rate expected. The orifice plate has four 1mm tappings upstream and downstream of the plate, the four tappings being combined into a single tube by a manifold ring. Details of the orifice plate design, as well as its operating constants, can be found in Appendix A.

4.4 Data Acquisition and Control

4.4.1 Transducers

There are three types of transducers, namely load cells, pressure transducers and position transducers.

4.4.1.1 Load Cells

Two load cells are used to measure the model lift and drag. The load cells were designed and supplied by Load Cell Services, Pretoria. The load cells are rated to 3000N and 1500N for lift and drag respectively, and each have their own mains (220VAC) power supply and signal amplifier. The amplifier outputs analog data via a 0-10V voltage system, as well as a 5-20mA current system. The current system was employed since it allows long leads to be used from the amplifier to the data acquisition system, without introducing noise problems. A 500 ohm resistor is used to convert the 4-20mA current signal into a 2-10V voltage signal, which is compatible with the A/D system.

4.4.1.2 Pressure Transducers

Three Rosemount differential pressure transducers, model 1151DP, are used to measure the following:

p_1 Boom pressure and orifice upstream pressure.
p_2 Tunnel static pressure.
p_3 Orifice plate differential pressure.

The pressure transducers employ a 2-wire current system to power the device as well as transmit the data. Voltages ranging from 12VDC to 45VDC can be used to power the device. The current based data transmission system allows long leads to be used to the data acquisition without introducing noise problems. A 500 ohm resistor converts the 4-20mA current signal into a 2-10V voltage signal, which is compatible with the A/D system.

4.4.1.3 Position Transducers

Fifty-two Bournes precision potentiometers are used to measure the displacement of the adaptive wall actuators. The potentiometers have a nominal resistance of 1000 ohms and an independent linearity of 0.025%. A 9VDC power supply is used to power the potentiometers, but the regulation of this voltage is not critical since the data acquisition system effectively only measures the resistance of the potentiometer. This is achieved by measuring both the applied voltage and the potentiometer wiper

voltage. The ratio of these two voltages is then only a function of the potentiometer and system resistance, and independent of the applied voltage. All voltage signals are transmitted to the A/D system by a shielded cable to avoid noise interference.

4.4.2 A/D System

An Eagle Electric PC30D A/D card, in conjunction with a PC81 input multiplexer, is used to convert 0-10V analog voltages into a twelve bit binary number. The input multiplexer is powered and controlled by the data acquisition card, and was selected for its compatibility with the A/D card. 4.7μF capacitors, inserted between the multiplexer inputs and ground, were used to reduce electrical noise caused by the motor speed control. Demonstration software supplied by Eagle Electric in the form of numerous procedures, was used to write the tunnel operating software.

4.4.3 I/O System

An Eagle Electric PC192 I/O card is used to output 5V TTL digital signals. These signals are used to switch solid state Darlington relays, which in turn activate electro-mechanical relays controlling the adaptive wall actuators.

4.5 Software Design

The software developed can be broadly divided into three groups, namely calibration, operating and utility software. All software can be found on disk in Appendix F.

4.5.1 Calibration Software

Software was developed to simplify the calibration procedure for the entire wind tunnel system. This software allows the tunnel walls (position transducers), pressure transducers and load cells to be calibrated. The calibration data is later processed by a least squares regression, yielding operating constants for all the transducers.

4.5.1.1 Raw Data Acquisition

The physical calibration of the transducers yields raw data.

4.5.1.1.1 Position Transducers

The program WALLCALI.EXE requests the operator to manually position all the slides to a known position. Position

measurements are then taken by the A/D system. The program then requests the operator to move the slides to the next position, the process being repeated until all the known positions have been covered. The raw data is stored in files UPPER.000, UPPER.166, UPPER.333, UPPER.500, UPPER.666 and UPPER.833 for the short slides, and LOWER.n16, LOWER.000, LOWER.166, LOWER.333, LOWER.500, LOWER.666, LOWER.833 and LOWER.100 for the long slides.

4.5.1.1.2 Load Transducers

The program LOADCALI.EXE prompts the user for the magnitude of the known weights that are being used to separately load the lift and drag load cells. The A/D system records all the load measurements, and stores the data in the files LIFTCALI.DAT for lift, and DRAGCALI.DAT for drag.

4.5.1.1.3 Pressure Transducers

The program PRESCALI.DAT prompts the user for the magnitude of the known pressures that are being applied to each pressure transducers. The A/D system records pressure measurements, and stores the data in the files PRESCAL1.DAT, PRESCAL2.DAT and PRESCAL3.DAT.

4.5.1.1.4 Tunnel Speed Calibration

The program CALSPEED.EXE prompts the user for a desired tunnel speed. The tunnel walls are then adjusted to give a zero longitudinal pressure gradient. The tunnel static pressure and true pitot velocity are then measured, and stored in the file SPEEDCAL.DAT.

4.5.1.2 Data Processing

Once all the raw data have been obtained, they are processed so that they can be used by the tunnel operating software.

4.5.1.2.1 Position Transducers

The program CALIBRAT.EXE is used to read in all the raw position data files, ie. UPPER.* and LOWER.*, and then apply a least squares quadratic regression to the readings of each transducer. The resulting three constants per transducer are stored in the file CALIBRAT.DAT, for use by the tunnel operating software.

4.5.1.2.2 Load and Pressure

The program CALTRANS.EXE reads in the raw load and pressure data files, ie. LIFTCALI.DAT, DRAGCALI.DAT and PRESCAL*.DAT. A least squares linear regression is applied to the data of each transducer, the resulting two constants for each transducer being stored in the file CALTRANS.DAT. This file is used by the tunnel operating software.

4.5.1.2.3 Tunnel Speed

The program SPEEDPRO.EXE reads in the raw tunnel speed data, ie. SPEEDCAL.DAT, and fits a least squares linear regression to the data. The resulting two constants are stored in the file SPEEDPRO.DAT, for use by the tunnel operating software.

4.5.2 Operating Software

The program MAINPROG.EXE controls the operation of the tunnel during normal testing. This program automatically positions the wind tunnel side walls, and then acquires data from the various transducers. The operating software performs the following tasks to initialize the tunnel and hardware.

1 Initialize the A/D and I/O cards.
2 Prompt the user for ambient atmospheric conditions.
3 Prompt the user for orifice plate and slot sizes.
4 Read in transducer zero values.
5 Read in calibration constants for all transducers.

Once the tunnel and hardware has been initialized, the following tasks are performed to obtain each data point.

1 Prompt the user for tunnel streamlining parameters.
2 Calculate wall positions and boundary layer thickness.
3 Position walls.
4 Acquire data.

4.5.3 Utility Software

The utility software was developed to aid the user with certain tasks that are not absolutely necessary for the operation of the tunnel.

4.5.3.1 Velocity Traverse

The program VELOPROF.EXE requests the user to position the pitot tube at a certain test section transverse position. Tunnel static and pitot velocities are then recorded every 0.1s for a total of

60s. The velocities of 36 stations are recorded in the files VELOPRO1.DAT through to VELOPR36.DAT.

4.5.3.2 Relay Checking

The operation of the all the tunnel relays can be verified using the program RELAYCHK.EXE. This program switches each relay on and off in a manner that is discernable by the user. If there are any irregularities in the pattern of the clicking sounds, one or more of the relays is faulty.

4.5.3.3 Data Acquisition

The data acquisition system, as well as the transducers, can be checked without running the entire tunnel operating software. The program AQUIDATA.EXE reads in all the transducer values, and displays them on the screen. In this way, the response of transducers to applied loads and so forth, can be observed. The transducers can also be stored on the file AQUIDATA.DAT.

4.5.3.4 Wall Pressure Calculation

In order to be able to plot the predicted wall pressure distribution, the program CALCPRES.EXE calculates the wall pressures for any given tunnel speed, lift coefficient, drag coefficient and slot blowing volumetric flow rate. The effect of wall pressure tapping movement, as a result of a changing wall curvature and hence arclength, is taken account of by the algorithm.

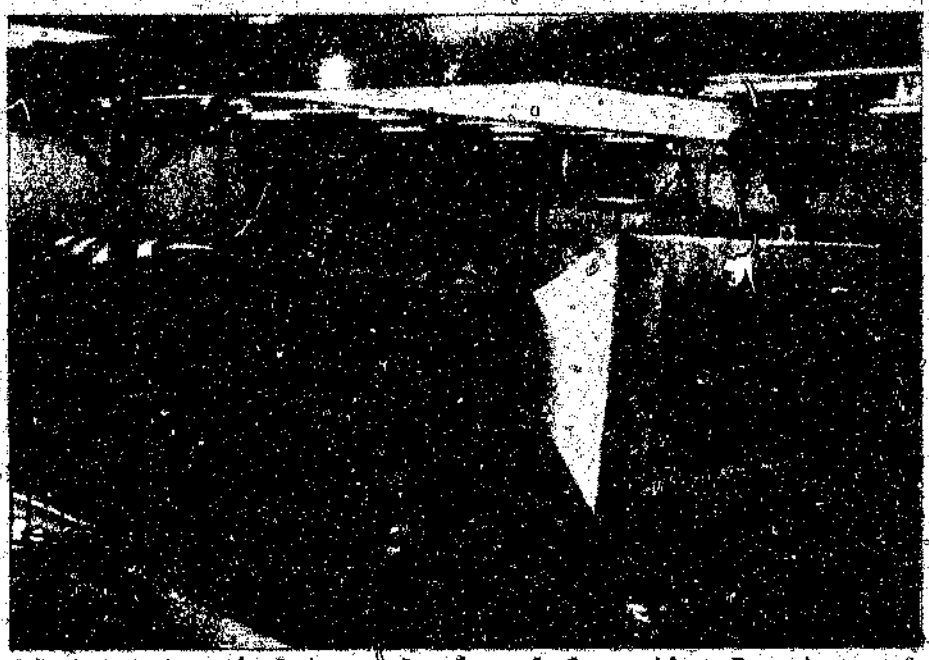

Plate 4,1: Wind tunnel viewed from the front.

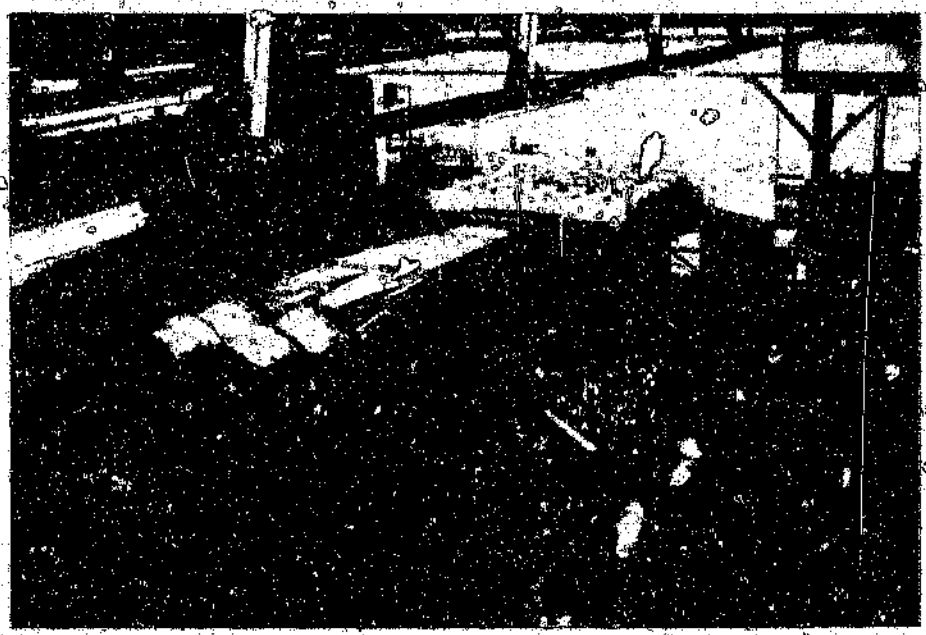

Plate 4,2: Wind tunnel viewed from behind.

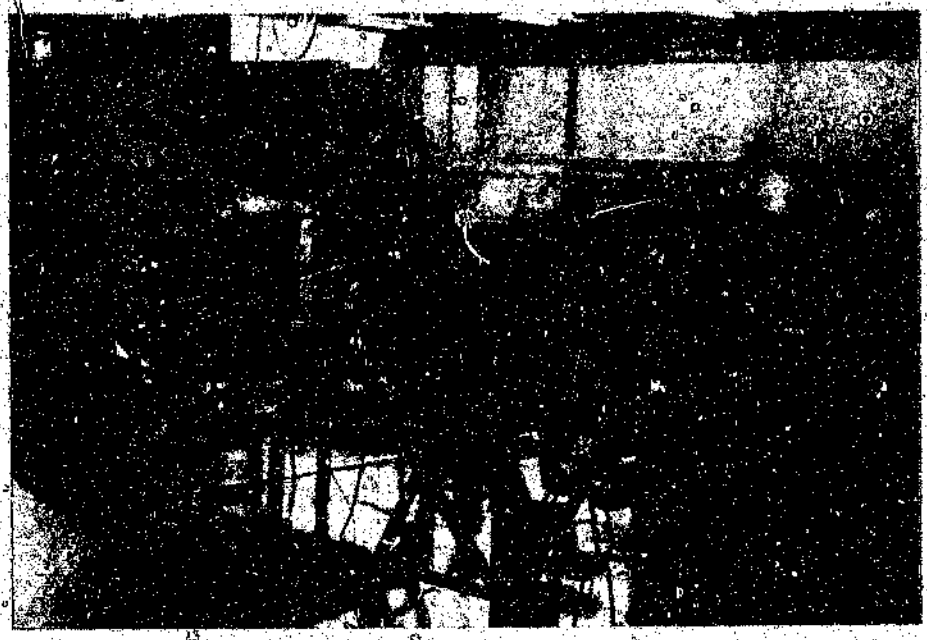

Plate 4,3: Test section inlet.

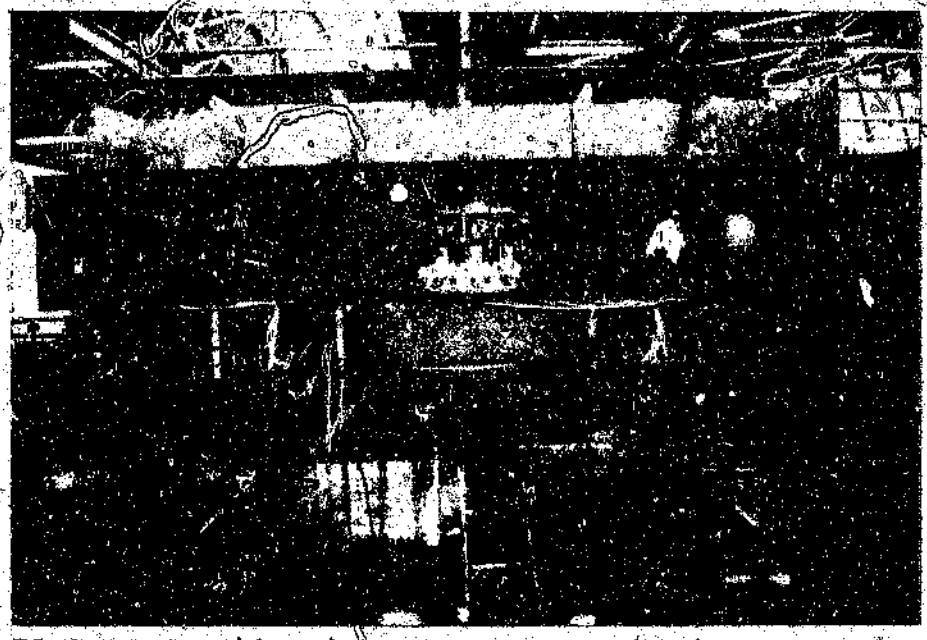

Plate 4,4: Side view of the test section.



Plate 4.5: Internal view of the test section.

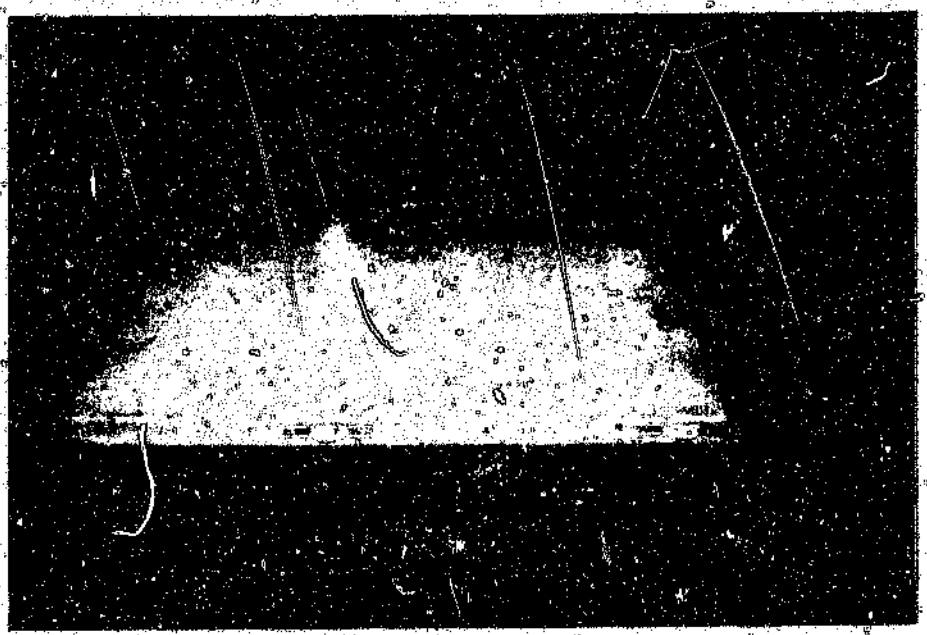

Plate 4.6: View of a slide.



Plate 4,7: View of an actuator.

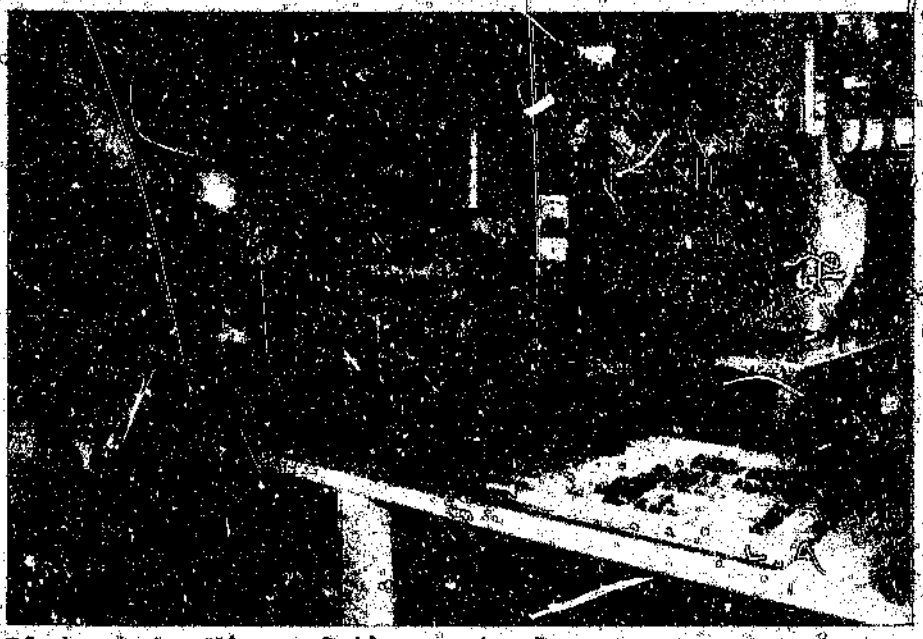

Plate 4,8: View of the control room.

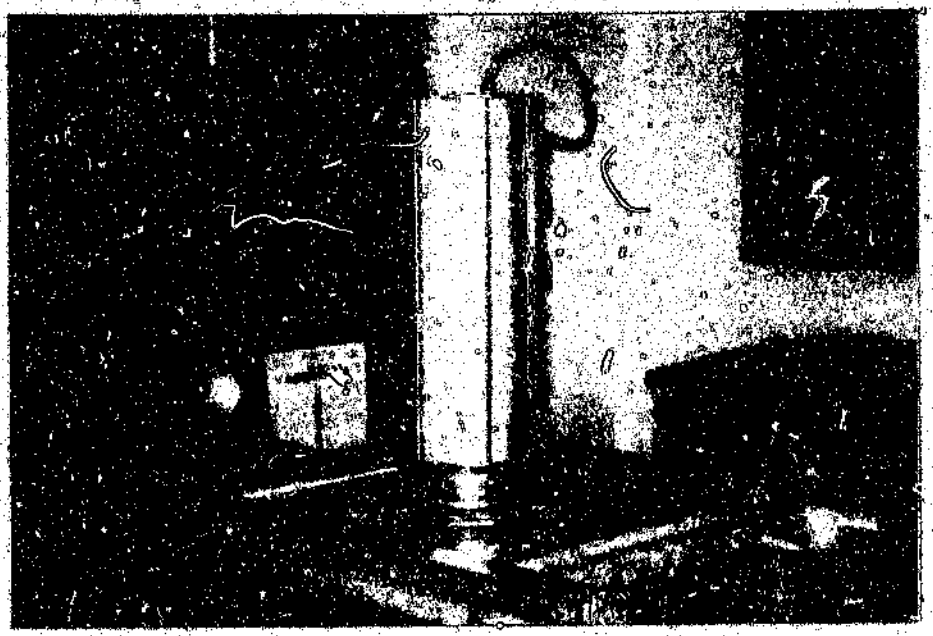

Plate 4,9: View of the CC cylinder.

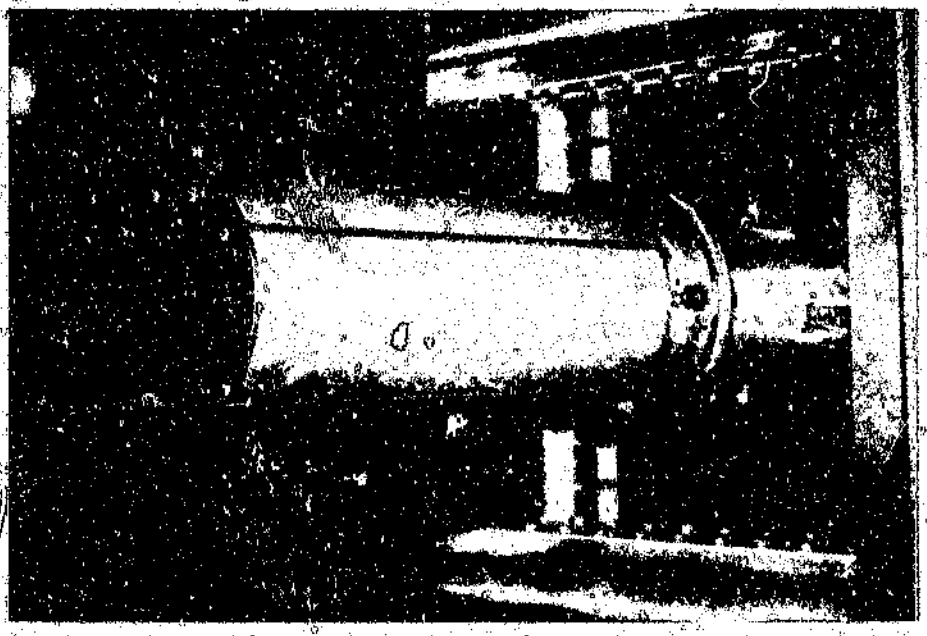

Plate 4,10: View of the blowing slots.

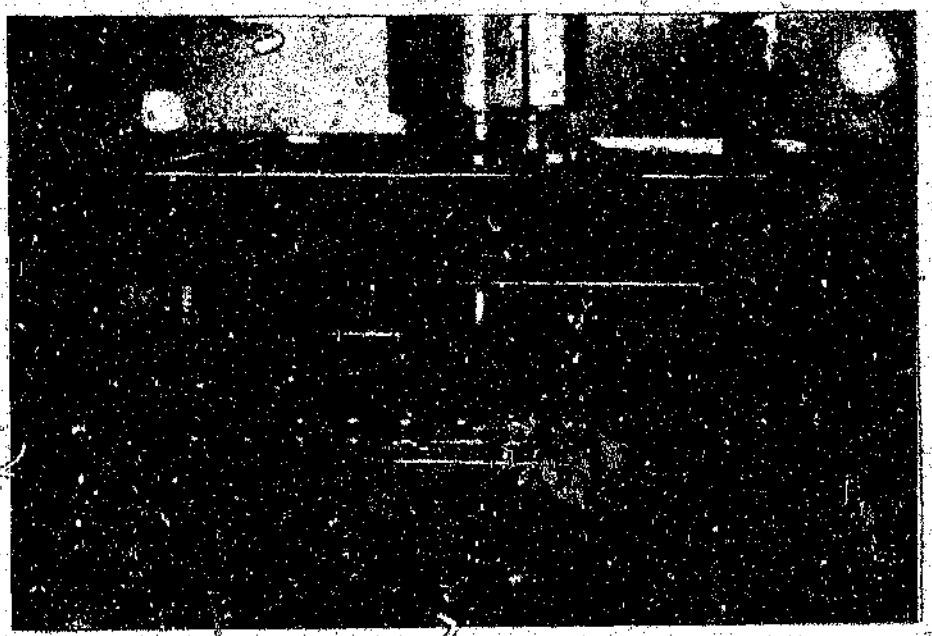

Plate 4,11: View of the balance.



Plate 4,12: Circulation control blower.

5 Theoretical Analysis

The theoretical analysis deals with the development of the streamlining algorithm, as well as a dimensional and an error analysis.

5.1 Wall Streamlining Theory

In order to streamline the walls to the correct positions, an inviscid, incompressible potential flow analysis is used to model the effect of lift, drag and fluid addition on a cylinder in a freestream. It was decided to use a potential flow analysis since the theory is simple, especially when applied to a circular cylinder. Since the tunnel walls are in the inviscid flow field of the aerofoil, considering only pressure and inertia forces to find the streamlines in this region is a sufficiently good approximation.

Lewis[9], whose work focused on transonic adaptive wall testing, found that a potential flow solution was adequate for subsonic testing, especially if the effects of aerofoil thickness and camber were taken into account by means of a Zhukovsky transformation.

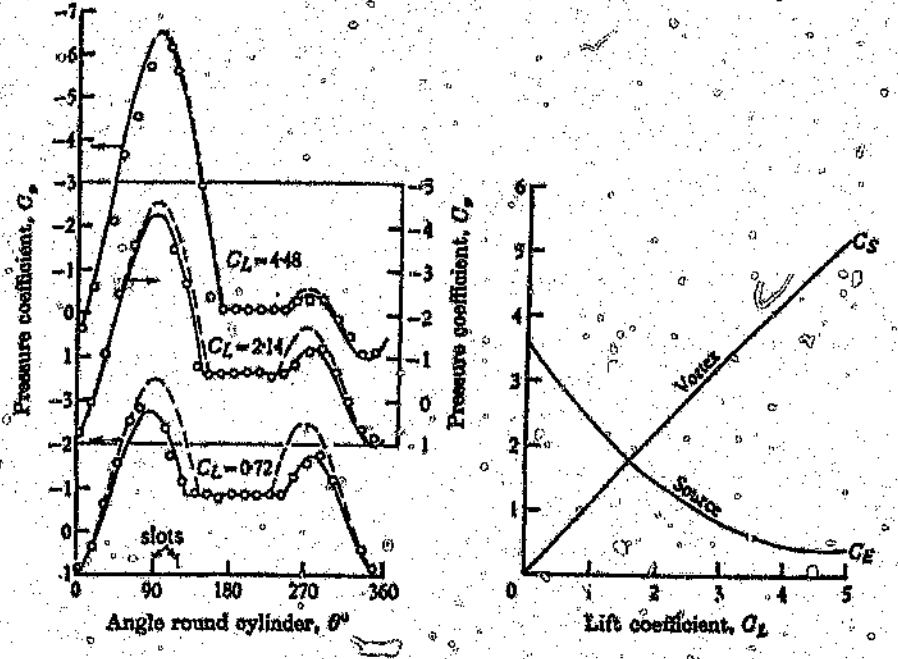

Figure 5.1: Pressure distribution about cylinder.[17]

Dunham[17] found that the pressure distribution about a lifting cylinder can be accurately predicted by means of a simple potential flow analysis, with drag being modelled as an additional source flow. The left hand graph of Figure 5.1 shows the measured and predicted pressure distribution about a lifting cylinder. The dots are experimental points, while the solid and dotted lines are predicted pressure distributions calculated with and without a source flow in the potential flow model, respectively. It can be seen that the solid line matches the experimental points almost perfectly. If the pressures can be matched so closely in the vicinity of the model, it is very likely that the far flow field pressure prediction will be very accurate. In other words, if a potential flow model is used that takes into account the effects of lift and drag (caused by viscous shear or separation), the streamline shapes predicted are very likely to be correct.

There is one difference between the theoretical model used by Dunham, and the one used in this research. Whereas Dunham uses empirical values for the vortex, C_s, and source, C_s, strength, as given in the right hand graph of Figure 5.1, the strengths of these elementary flows used in the present research is based on theoretical considerations.

Suppose a lifting body of arbitrary geometry is flying in an real, incompressible and unconfined flow field. If an imaginary boundary is drawn around the body such that it is in the inviscid far flow field of the body at all points, ie. not passing through regions with notable viscous forces except the wake, the only evidence to be found outside that boundary that the body is lifting is a circulatory flow of strength $L/(\rho U)$[22]. Similarly, the only evidence that can be found outside the boundary that the body has drag, is that the uniform flow field has been displaced to allow for the slower moving wake of the body. This displacement is the same as that created by a source of strength $D/(\rho U)$[6] in an inviscid flow field.

These two observations are still not sufficient to describe the flow field completely, since the geometry of the body will influence the shape of the streamlines, ie. the circulatory and source effects are distributed. At very great distances from the body, however, the flow will be fully defined since the effect of vortex and source distribution will be zero as a result of the $1/r$ nature of the two elementary flows.

For the present research, the geometry of the body is known, and is easily represented by a doublet in the freestream. Since the tunnel walls are not very close to the body, this representation of the model geometry is probably sufficient to obtain realistic streamline shapes. The cylinder is therefore represented as the sum of a doublet to represent the model geometry, a source to represent the model drag, and a vortex to represent the model lift. The addition of fluid by the CC slots is modelled as an additional source.

5.1.1 Potential Flow

Karamcheti[21], amongst others, gives a detailed derivation of the concepts of the stream-function, the main results now being reiterated. Streamlines are represented by lines of constant stream-function, since there is no flow across a streamline.

5.1.1.1 Elementary Flows

For the uniform stream, Ψ is given by

$$\psi(x,y) = -Vx + Uy \qquad (5,1)$$

For a source centred at the origin, Ψ is given by

$$\psi(x,y) = \frac{q}{2\pi}\arctan\left(\frac{y}{x}\right) + c \qquad (5,2)$$

For a doublet centred at the origin, Ψ is given by

$$\psi(x,y) = \frac{\mu}{2\pi}\frac{y}{x^2+y^2} \qquad (5,3)$$

For a line vortex centred at the origin, Ψ is given by

$$\psi(x,y) = \frac{-k}{2\pi}\ln\left(\sqrt{x^2+y^2}\right) + c \qquad (5,4)$$

5.1.1.2 Combined Flow

The stream-function for a flow consisting of all four the elementary flows listed above is merely the sum of the above stream-functions. For a stagnation point at r = a, ie. to obtain a circular streamline corresponding to the closed circuit r = a, it can be shown that

$$\mu = 2\pi U a^2 \qquad (5,5)$$

It can also be shown lift per unit span is equal to

$$L = \rho U k = \frac{1}{2}\rho U^2 d C_l \qquad (5,6)$$

Since d = 2a, k can be derived from equation 5.6.

$$k = U C_l a \qquad (5,7)$$

It can be shown that drag is given by

$$D = \rho U q_{drag} = \frac{1}{2}\rho U^2 d C_d \qquad (5,8)$$

Since d = 2a, the source strength representing the cylinder drag, q_{drag}, is given by

$$q_{drag} = U C_d a \qquad (5,9)$$

However, since the source represents the effects of both drag and fluid addition, an additional term representing fluid addition is added. This term is written in the same units as source strength, ie. fluid added per unit span. Thus q_{total} is the sum of q_{drag} and q_{slot}, the complete equation for source strength being given by

$$q_{total} = U C_d a + \frac{Q_{slot}}{b} \qquad (5,10)$$

where Q_{slot} is the net volumetric flow rate leaving the slots of the aerofoil and b is the aerofoil wingspan.

The combined stream-function is given by

$$\psi = Uy + \frac{q_{total}}{2\pi}\arctan\left(\frac{y}{x}\right) - \frac{\mu}{2\pi}\frac{y}{x^2+y^2} + \frac{k}{2\pi}\ln\left(\sqrt{x^2+y^2}\right) = C \qquad (5,11)$$

where q_{total}, μ and k are taken from equations 5.10, 5.5 and 5.7 respectively.

5.1.2 Newton - Raphson Method

In order solve the constant stream-function for y in terms of x, it is necessary to use a numerical method since the equations cannot be written explicitly. Applying the Newton - Raphson method for the solution of the roots of equation 5.11 requires that the equation be written as

$$f(y) = 0 = \psi(x,y) - C \qquad (5,12)$$

The Newton - Raphson method gives successive approximations of y to be

$$y_i = y_{i-1} - \frac{f(y)}{f'(y)} \qquad (5,13)$$

where f'(y) is given by

$$f'(y) = U + \frac{q}{2\pi} \frac{1}{\left(1+\frac{y^2}{x^2}\right)} - \frac{\mu}{2\pi} \frac{(x^2-y^2)}{(x^2+y^2)^2} + \frac{k}{2\pi} \frac{y}{(x^2+y^2)} \qquad (5,14)$$

The final value of y is obtained when the difference between successive approximations of y is less than a certain error tolerance.

5.2 Dimensional Analysis

A dimensional analysis, using Buckingham's π theorem, was performed to establish the relevant dimensionless groupings to be used in the reduction of the test data. Table 5.1 gives 8 variables which could affect the data. They are the aerodynamic forces experienced by the model, slot momentum, slot power, boom pressure, slot flow rate, air density, tunnel velocity and the size of the model. The latter 3 variables were taken to be independent, leaving the other 5 variables as dependent variables. The indices of the fundamental dimensions, ie mass, length and time, for each variable are given in the table. The indices relevant to each variable are given below the variable.

Table 5.1: Dependent and independent variables.

	Force	Momen	Power	p_{slot}	Q_{slot}	ρ	U	d
M	1	1	1	1	0	1	0	0
L	1	1	2	-1	3	-3	1	1
T	-2	-2	-3	-2	-1	0	-1	0

Each dependent variable can be written as a dimensionless parameter, π, if the data is reduced by the groupings given below.

Force

$\rho^a\ U^b\ d^c = M^0\ L^0\ T^0$

$M\ L\ T^{-2}\ \ M^a\ L^{-3a}\ \ L^b\ T^{-b}\ \ L^c = M^0\ L^0\ T^0$

Exponents of M: $1 + a = 0$

Exponents of L: $1 - 3a + b + c = 0$

Exponents of T: $-2 - b = 0$

Solving for a, b and c yields $a = -1$, $b = -2$, $c = -2$.

Thus $\pi_1 = \text{Force}/(\rho\ U^2\ d^2)$

Momentum

$\rho^a\ U^b\ d^c = M^0\ L^0\ T^0$

$M\ L\ T^{-2}\ \ M^a\ L^{-3a}\ \ L^b\ T^{-b}\ \ L^c = M^0\ L^0\ T^0$

Exponents of M: $1 + a = 0$

Exponents of L: $1 - 3a + b + c = 0$

Exponents of T: $-2 - b = 0$

Solving for a, b and c yields $a = -1$, $b = -2$, $c = -2$.

Thus $\pi_2 = \text{Momentum}/(\rho\ U^2\ d^2)$

Power

$\rho^a\ U^b\ d^c = M^0\ L^0\ T^0$

$M\ L^{-3}\ M^a\ L^{-3a}\ L^b\ T^{-b}\ L^c = M^0\ L^0\ T^0$

Exponents of M: $1 + a = 0$

Exponents of L: $2 - 3a + b + c = 0$

Exponents of T: $-3 - b = 0$

Solving for a, b and c yields $a = -1$, $b = -3$, $c = -2$.

Thus π_3 = Power/($\rho\ U^3\ d^2$)

Pressure

$\rho^a\ U^b\ d^c = M^0\ L^0\ T^0$

$M\ L^{-1}\ T^{-2}\ M^a\ L^{-3a}\ L^b\ T^{-b}\ L^c = M^0\ L^0\ T^0$

Exponents of M: $1 + a = 0$

Exponents of L: $-1 - 3a + b + c = 0$

Exponents of T: $-2 - b = 0$

Solving for a, b and c yields $a = -1$, $b = -2$, $c = 0$.

Thus π_4 = Pressure/($\rho\ U^2$)

Volumetric Flow Rate

$\rho^a\ U^b\ d^c = M^0\ L^0\ T^0$

$L^3\ T^{-1}\ M^a\ L^{-3a}\ L^b\ T^{-b}\ L^c = M^0\ L^0\ T^0$

Exponents of M: $a = 0$

Exponents of L: $3 - 3a + b + c = 0$

Exponents of T: $-1 - b = 0$

Solving for a, b and c yields $a = 0$, $b = -1$, $c = -2$.

Thus π_5 = Volumetric Flow Rate/($U\ d^2$)

Looking at π_3, π_4 and π_5, it can be deduced that power is the product of pressure and volumetric flow rate. Indeed, for an incompressible fluid, this is so. A dimensionless boom power can thus be obtained from the product of boom pressure and boom flow rate. It shall be seen in Chapter 9 that this is quite a useful parameter, since it can be used to compare the merits of various model configurations.

5.3 Error Analysis

An error analysis was performed to determine the uncertainty in the processed data as a result of transducer inaccuracy and resolution.

The lift and drag load cells have a independent linearity of 0.1% of the calibrated span. The lift load cell was calibrated from 0 - 1500N, while the drag load cell was calibrated from 0 - 600N. The maximum uncertainty in the outputs of the lift and drag load cells is therefore 1.5N and 0.6N respectively.

The pressure transducers have an independent linearity of 0.2% of the calibrated span. The three pressure transducers, ie. p_1, p_2 and p_3, were calibrated for a span of 2000Pa, 5000Pa and 7500Pa, respectively. The maximum uncertainty in the outputs of the three transducers is therefore 4Pa, 10Pa and 15Pa respectively.

Since the analog readings of the transducers have to be converted to digital values before they can be processed, the resolution of the A/D system must be found. For a 0 - 10V input, the A/D card generates a 12 bit digital output, implying a resolution of 1 part in 4096. However, the transducers output a current signal ranging between 4mA and 20mA, which is converted into a voltage ranging between 2V and 10V to be compatible with the A/D card. The final resolution of the A/D card is therefore only 1 part in (4/5x4096), ie. 1 part in 3277, or 0.03%. Since this resolution is smaller than the uncertainty in the outputs of the transducers, the accuracy of the measurements is not a function of the resolution of the A/D card.

The span and chord of the cylinder can be measured accurately to within 0.0005m, and since S = b x c, the uncertainty in S can be written as

$$\frac{\Delta S}{S} = \left|\frac{\Delta b}{b}\right| + \left|\frac{\Delta c}{c}\right| \qquad (5,15)$$

Using $\Delta b = 0.0005$, $\Delta c = 0.0005$, $b = 0.5$ and $c = 0.2$, yields $\Delta S/S = 0.0035$.

The dynamic pressure is obtained directly from the tunnel static pressure, therefore the uncertainties in dynamic and static

pressures are identical. The maximum uncertainty in the tunnel dynamic pressure is obtained using the lowest tunnel speed, which was 25 m/s. Using ρ_{air} = 1, c_1 = 312.5 and Δq = 4, yields $\Delta q/q$ = 0.0128.

The lift coefficient can be written as

$$C_l = \frac{L}{qS} \tag{5,16}$$

The uncertainty in C_l is given as

$$\frac{\Delta C_l}{C_l} = \left|\frac{\Delta L}{L}\right| + \left|\frac{\Delta q}{q}\right| + \left|\frac{\Delta S}{S}\right| \tag{5,17}$$

The maximum uncertainty in C_l will be obtained at the lowest measured lift, which was C_l = 1 or L = 31.25. Using $\Delta q/q$ = 0.0128, ΔL = 1.5 and $\Delta S/S$ = 0.0035, yields $\Delta C_l/C_l$ = 0.064 or 6.4%.

The drag coefficient can be written as

$$C_d = \frac{D}{qS} \tag{5,18}$$

The uncertainty in C_d is given as

$$\frac{\Delta C_d}{C_d} = \left|\frac{\Delta D}{D}\right| + \left|\frac{\Delta q}{q}\right| + \left|\frac{\Delta S}{S}\right| \tag{5,19}$$

The maximum uncertainty in C_d will be obtained at the lowest measured drag, which was C_d = 0.4 or D = 12.5. Using Δq = 0.0128, ΔD = 0.6 and $\Delta S/S$ = 0.0035, yields $\Delta C_d/C_d$ = 0.064 or 6.4%.

The orifice flow rate can be written as

$$Q = k\sqrt{\Delta p} \tag{5,20}$$

where k includes the orifice coefficients.

The uncertainty in Q is given as

$$\frac{\Delta Q}{Q}=\left|\frac{\Delta k}{k}\right|+\frac{1}{2}\left|\frac{\Delta p}{p}\right| \qquad (5,21)$$

The lowest flow rate measured was typically $0.1m^3/s$, corresponding to a differential pressure p = 180Pa. Since $\Delta p = 10$ and the error in the orifice coefficients are estimated to be below 1% or 0.001, $\Delta Q/Q = 0.029$ or 2.9%.

The momentum coefficient can be written as

$$C_\mu=\frac{Q^2}{\left(\frac{t}{c}\right)qS^2} \qquad (5,22)$$

The uncertainty in C_μ is given as

$$\frac{\Delta C_\mu}{C_\mu}=2\left|\frac{\Delta Q}{Q}\right|+\left|\frac{\Delta\left(\frac{t}{c}\right)}{\left(\frac{t}{c}\right)}\right|+\left|\frac{\Delta q}{q}\right|+2\left|\frac{\Delta S}{S}\right| \qquad (5,23)$$

The slot size can be measured to within 0.05mm, and since the smallest slot size used was 1mm, the uncertainty in t/c is 0.05. Using $\Delta Q/Q = 0.029$, $\Delta q/q = 0.0128$ and $\Delta S/S = 0.0035$, yields $\Delta C_\mu/C_\mu = 0.127$ or 12.7%.

U can be written as a function of the tunnel dynamic pressure as

$$U=k\sqrt{q} \qquad (5,24)$$

where k is a calibration constant. The uncertainty in U can be written as

$$\frac{\Delta U}{U}=\frac{1}{2}\left|\frac{\Delta q}{q}\right| \qquad (5,25)$$

Since $\Delta q/q = 0.0128$, $\Delta U/U = 0.0064$.

The power coefficient can be written as

$$C_{pow}=\frac{pQ}{qSU} \qquad (5,26)$$

The uncertainty in the power coefficient is given as

$$\frac{\Delta C_{pow}}{C_{pow}}=\left|\frac{\Delta p}{p}\right|+\left|\frac{\Delta Q}{Q}\right|+\left|\frac{\Delta q}{q}\right|+\left|\frac{\Delta U}{U}\right|+\left|\frac{\Delta S}{S}\right| \qquad (5,27)$$

The smallest boom pressure was approximately 600Pa. Using Δp = 15, $\Delta Q/Q$ = 0.029, $\Delta q/q$ = 0.0128, $\Delta S/S$ = 0.0035 and $\Delta U/U$ = 0.0064, yields $\Delta C_{pow}/C_{pow}$ = 0.077 or 7.7%.

The uncertainties in some of the calculated quantities is high, but it must be remembered that the values given above are the worst case. Readings taken at higher tunnel velocity, with greater lift and slot momentum will have a lower uncertainty. Since almost all the tests were comparative, the absolute accuracy of measurements less critical.

The large uncertainty in the lift and drag coefficients can be attributed to using load cells that had too great a span. The large uncertainty in the pressure related quantities, especially tunnel speed and orifice flow rate, can be attributed to the square-root nature of these quantities. Even though the span of the transducers was compatible with the magnitude of measurements taken, quantities of low magnitude had inherent uncertainty due to the very nature of the measuring technique, ie. the orifice plate or pitot tube.

In an attempt to reduce the uncertainty in the measurements, zero load and pressure readings were taken at the start of each test, these values being subtracted from subsequent readings. This procedure tends to reduce the uncertainty in the measured quantities, but it is difficult to predict by how much.

6 Calibration of Equipment

The confidence with which wind tunnel data can be presented is dictated to a large extent by how carefully the entire test facility is calibrated. To ensure the repeatability and accuracy of the entire wind tunnel calibration, it was decided to develop dedicated calibration software which would aid the operator in the calibration of the tunnel. The use of this software relieves the tunnel operator of the tedious task of remembering details of the calibration procedure, since the calibration software performs all the relevant measurements and merely prompts the user for any external inputs when these are required. The operator can therefore concentrate on other important tasks such as the qualitative observation, i.e. looking and listening for irregularities, of the calibration. All computer programs mentioned in this chapter can be found in Appendix F.

6.1 Wind Tunnel Calibration

6.1.1 Test Section Velocity Traverse

A velocity traverse of the test section was performed to establish the shape of the transverse velocity profile in the test section. Using the calibration program, 'VELOPROF.EXE', velocities at 36 stations, in a plane transverse to the tunnel axis at the centre of the test section, were measured.

Due to the unavailability of a total head rake, velocity could not be measured simultaneously at all 36 stations, therefore it was therefore decided to measure both the local dynamic pressure in the test section, as well as the tunnel static pressure at the test section inlet. The ratio of the dynamic pitot and static tunnel velocities yields a useful normalized parameter since its magnitude is not dependent on a temporally constant tunnel velocity, a condition that would be very difficult to realize, since the acquisition of the 36 readings was effected over a period of approximately an hour.

The local dynamic pressure was measured using an elliptic-head pitot tube in the arrangement shown in Plate 6,1. The tunnel static pressure was obtained from a ring of 8 static pressure tappings at the test section inlet. Due to slight variations of tunnel velocity with time (suspected to be due to local laminar flow separation occurring at the very forward edge of the inlet

contraction), it was decided to record velocities at each station over a relatively long period of 60 seconds. Measurements being taken at intervals of 0.1 seconds, the large number of readings being required to get an idea of the temporal variation of the flow velocity.

Figure 6.1 through to Figure 6.4 reveal some typical variations of pitot velocity, tunnel velocity and their ratio over 60 seconds, for 4 different transverse locations. Only these 4 velocity traces are shown because they are indicative of the type of variation that was observed in all the other velocity traces. The random velocity variations, probably caused by flow separation in the inlet contraction, can be seen quite clearly from these curves. It is observed that, apart from periods where the velocity suddenly decreases, the test section velocity remains quite constant with time.

Taking the arithmetic average of the velocity ratio over 60 seconds, and plotting it for all 36 stations, yields Figure 6.5. This plot shows the transverse variations in the test section velocity ratio at four different vertical positions ($z = -0.15m$ to $z = 0.15m$), and it can be observed that the greatest variation is only 0.5%, a quite acceptable level of transverse velocity variation according to Pope and Rae[6].

6.1.2 Test Section Flow Angularity

Due to the limited time available for calibration and testing, the angularity of the test section flow was not measured quantitatively. However, to obtain a quick indication of the flow angularity, it was decided to investigate the flow qualitatively by means of smoke flow visualization and the use of a tuft grid. Smoke flow visualization hinted at the possibility of flow separation on the left hand (if viewed from the front) lower lip of the inlet contraction. This separation was due to a surface curvature discontinuity, caused by a manufacturing error, on the lower surface of the inlet contraction in that region.

The tuft grid investigation confirmed this suspicion since the flow was generally well aligned everywhere in the test section, except for the short periods of tunnel speed instability. Plate 6,2 and Plate 6,3 show the tuft screen from two different perspectives, namely, from either side of the inlet contraction. If Plate 6,3 is carefully studied, the increased angularity in

the left hand bottom (if viewed from the front) corner can be observed. During periods of speed instability the flow was observed to have large and unsteady flow angularity in the lower left hand regions of the test section, this observation being in agreement with the evidence of the random temporal velocity fluctuations in the test section velocity traverses.

It was also noted that the tufts were very well aligned and steady as the tunnel speed was increasing, ie. when the tunnel drive power was increased, the opposite being true once the tunnel was slowed down. This indicates firstly that it is indeed the inlet contraction that is causing part or all of the tunnel temporal instability, and secondly that some small modification of shape at the inlet front edge may be all that is required to obtain a slightly more favourable pressure gradient in regions of separation. It should be noted that the inlet lip was designed as a radius to simplify manufacture, but from an aerodynamic point of view this is not very favourable. The fact that only the bottom lip seems to be causing trouble is comforting, since only this lip has a severe surface curvature discontinuity. If all surface curvature discontinuities are removed, ie. with filler, grinder and sandpaper, the tunnel temporal instability could be alleviated, or removed. If this does not rectify the matter, a new lip may have to be shaped. The latter operation would not be too difficult since the lip is not subject to any pressure loading of note, and a simple expanded polystyrene lip would be adequate, smoothness of curvature and surface being the major requirements.

6.1.3 Tunnel Turbulence Level

Due to the limited time available for testing, no direct measurements of the tunnel turbulence level were made. An indirect measurement was made in one of the later tests when the drag on the cylinder model, without circulation blowing, was measured. This test showed that the tunnel turbulence level is low, which can be expected since any (low) atmospheric turbulence level at the tunnel inlet will be reduced to a large degree by the high contraction ratio of the inlet contraction. The full details of this test are discussed in Section 9.2.1.

6.1.4 Wall Boundary Layer Correction

The effect of boundary layer growth on all four walls of the test section is accounted for by the displacement of the two side

walls of the test section to obtain a zero longitudinal pressure gradient down the length of the test section. It is assumed that the test section boundary layer is turbulent, and that it is not seriously distorted by pressure gradients created by the model. This is a reasonable assumption since pressure gradients in the region of the wall caused by the model will not be too steep. The turbulent boundary layer thickness, as suggested by Prandtl and Blasius, for a flow with zero pressure gradient is given by Douglas, Gasiorek and Swaffield[22] to be

$$\delta = 0.37 x Re_x^{-\frac{1}{5}} \qquad (6,1)$$

The boundary layer displacement thickness can be calculated using the following equation from Hoerner[23]. For a turbulent boundary layer, Prandtl's power law gives n = 7.

$$\delta^* = \delta \left(\frac{1}{1+n}\right) \qquad (6,2)$$

The final boundary layer displacement thickness equation for the tunnel walls is given by.

$$\delta^* = 0.04625 A (x-B) \left(\frac{\rho U (x-B)}{\mu}\right)^{-\frac{1}{5}} \qquad (6,3)$$

The boundary layer equation contains two constants, namely a magnitude coefficient A, and a shift value B. The magnitude coefficient accounts for the fact that the side wall is displaced to account for its own boundary layer as well as that of half of the top and bottom walls. For a test section with an aspect ratio (width to height) of 2, this coefficient should have a value of 3. Since the turbulent boundary layer starts somewhere in the inlet contraction, and not at the start of the test section, a shift value is introduced to indicate the apparent start of the test section.

Using a multiple tube alcohol manometer, it is possible to choose values for the two boundary layer coefficients for each tunnel speed such that the longitudinal pressure gradient is zero. Varying the magnitude coefficient allows the general slope of the longitudinal pressure profile to be adjusted, while adjusting the

shift coefficient allows the shape, ie. concave or convex curvature of the pressure profile to be varied. It was found that a magnitude coefficient of 3 and a shift coefficient of 2 yielded pressure profiles that were both flat and level for all tunnel speeds. The magnitude coefficient was as expected, and a shift coefficient of 2 indicates that the turbulent boundary layer starts 2m ahead of the test section centre, ie 0.25m ahead of the test section inlet. This makes sense since the boundary layer at the tunnel contraction exit would be thin, or in other words, an equivalent inlet with a zero longitudinal pressure gradient would be very short (0.25m). The fact that the two boundary layer coefficients are the same for various tunnel speeds is a useful finding since it means that the tunnel wall boundary layer can be accounted for with only two constants in a simple equation for all tunnel speeds. Plate 6.4 shows a typical wall pressure distribution after it has been corrected. There is some scatter in the readings which is probably due to slight waviness in the flexible walls. On average though, the distribution is satisfactory.

6.1.5 Tunnel Speed Setting

Once the test section boundary layer was accounted for, the tunnel was calibrated for speed. This was done by measuring the tunnel speed at the model location, ie. at the centre of the test section, by means of an elliptic head pitot tube, as well as the tunnel static ring pressure at the test section inlet. Readings were taken for velocities ranging from 0 to 55 m/s in increments of 5 m/s. Figure 6.6 shows true pitot velocity plotted against tunnel velocity (derived from tunnel static pressure by the Bernoulli equation). A least squares linear regression was performed on the data to obtain operating constants for the tunnel software. Figure 6.6 shows that the data has very little scatter, and that a linear fit is sufficient (standard deviation = 0.12%).

6.2 Data Acquisition Calibration

6.2.1 Position Transducers

The 52 wall position transducers (potentiometers) were calibrated with the aid of the calibration program, WALLCALI.EXE. The wall actuator slides were initially moved to known positions by means of an external power supply, after which the PC based A/D system recorded the transducer output for each potentiometer.

Since there are two types of slides, namely those in either Region I or Region II of Figure 4.1, the calibration of the wall position transducers was divided into two separate operations. The short slides were calibrated first by positioning all of them coincidentally at stations ranging from 0mm to 300mm in increments of 50mm. Once all the slides were in a given position, 1000 voltage readings of each potentiometer were recorded by the A/D system, the process being repeated until all the positions had been measured.

Once the short slides had been calibrated, the long slides were calibrated in a similar fashion, except that the positions ranged from -100mm through to 300mm in increments of 50mm.

Once the physical calibration had been completed, the raw calibration data for each transducer was fitted to a least squares quadratic regression by the processing program, CALIBRAT.EXE. This program automatically reads in all the relevant raw data files, processes the data to obtain three operating constants for each position transducer, and finally stores the operating constants in the file, CALIBRAT.DAT. This file is accessed by the tunnel operating software at tunnel start up, in order to obtain the calibration constants for the position transducers.

The raw calibration data can be found in the files UPPER.000, UPPER.166, UPPER.333, UPPER.500, UPPER.666, UPPER.833 and UPPER.100 (for the short slides); LOWER.N33, LOWER.N16, LOWER.000, LOWER.166, LOWER.333, LOWER.500, LOWER.666, LOWER.833 and LOWER.100 (for the long slides).

6.2.2 Pressure Transducers

The three pressure transducers were calibrated independently using an inclined leg alcohol manometer. The pressure ranges for the tunnel static pressure, orifice differential and boom manifold pressure were 2000, 5000 and 7500 Pa respectively.

The pressure transducer calibration was aided by the use of the calibration program, PRESCALI.EXE. This program prompts the user for 21 known pressures, usually twenty equal increments of the total transducer range as well as a zero reading, and then samples the relevant A/D channel 1000 times.
Before calibration could commence, the signal amplifiers of the

transducers had to be zeroed, and adjusted for the correct span. Being 4-20mA current devices, it was necessary to check that the zero pressure output did not drop below 4mA, and that the maximum pressure reading did not exceed 20mA. Additionally, since the A/D system requires voltages in a 0-10V range, the voltage output (generated by a 500 ohm nominal resistance resistor) at the A/D had to be checked to see that it did not exceed 10V.

The raw calibration data for the three pressure transducers is shown in Figure 6.7 through to Figure 6.9. A least squares linear regression was applied to the raw calibration data by the processing programme CALTRANS.EXE, yielding two operating constants for each pressure transducer. From the curves it can be seen that the data has very little scatter, and that a linear fit is sufficient (standard deviations of 0.05%, 0.04% and 0.12% respectively).

The raw calibration data can be found in the files PRESCAL1.DAT, PRESCAL2.DAT and PRESCAL3.DAT, while the processed calibration constants can be found in the file CALTRANS.DAT. This file contains the calibration constants for both the pressure transducers as well as the load cells, and is accessed each time the tunnel is started up.

6.2.3 Load Cells

The load cells were calibrated in situ using the balance calibration rig shown in Plate 6,5 and Plate 6,6. The balance is loaded in the lift and drag directions by means of weights hung beneath the balance as shown in Plate 6,7. Multi-strand steel cables (rated at 200 kg) transmit the tension loads, via pulleys, from the weights to a column inserted into the balance. The pulleys of the calibration rig can be adjusted vertically and horizontally, thereby making it possible to obtain tension precisely in the lift and drag directions.

Before calibration could commence, it was necessary to adjust the span and zero settings of the signal amplifiers. Since the amplifiers output a 4-20mA range, it was necessary to check that the signal did not drop below 4mA with no load, nor exceed 20mA at maximum load. Furthermore, since the A/D measures a 0-10V range, and since the resistor converting the current output to a voltage output only has a nominal resistance of about 500 ohms, it was necessary to check that the maximum load voltage at the

A/D did not exceed 10V. Once the amplifiers had been zeroed and ranged, the actual calibration could proceed.

The lift and drag directions were loaded independently, the outputs of both the lift and drag load cells being measured each time. The lift and drag directions were loaded with masses ranging from 0 to 150 kg, and 0 to 60 kg respectively, both in increments of approximately 4.5 kg.

The calibration program LOADCALI.EXE was used to acquire 1000 samples of each transducer output for each data point, the raw data being stored in the files LIFTCALI.DAT and DRAGCALI.DAT. The raw data of both the lift and the drag calibration is presented in Figure 6.10 and Figure 6.11.

A least squares linear regression was applied to the data to yield two operating constants per load cell. Referring to the calibration curves it is evident that the regressions fit well for both cases (standard deviations of 0.09% and 0.27% for the lift and drag load cells respectively), and that the unloaded load cell in each case has a constant output throughout the range of loading. This indicates that the two load directions are completely uncoupled, something which can be confirmed by inspection of the raw data. It is noteworthy that there is not so much as a 1 bit variation (in a range of 4096 bits) in the output of the unloaded load cell.

The processing program is called CALTRANS.EXE, and the processed constants are stored in CALTRANS.DAT, for use by the main tunnel operating program.

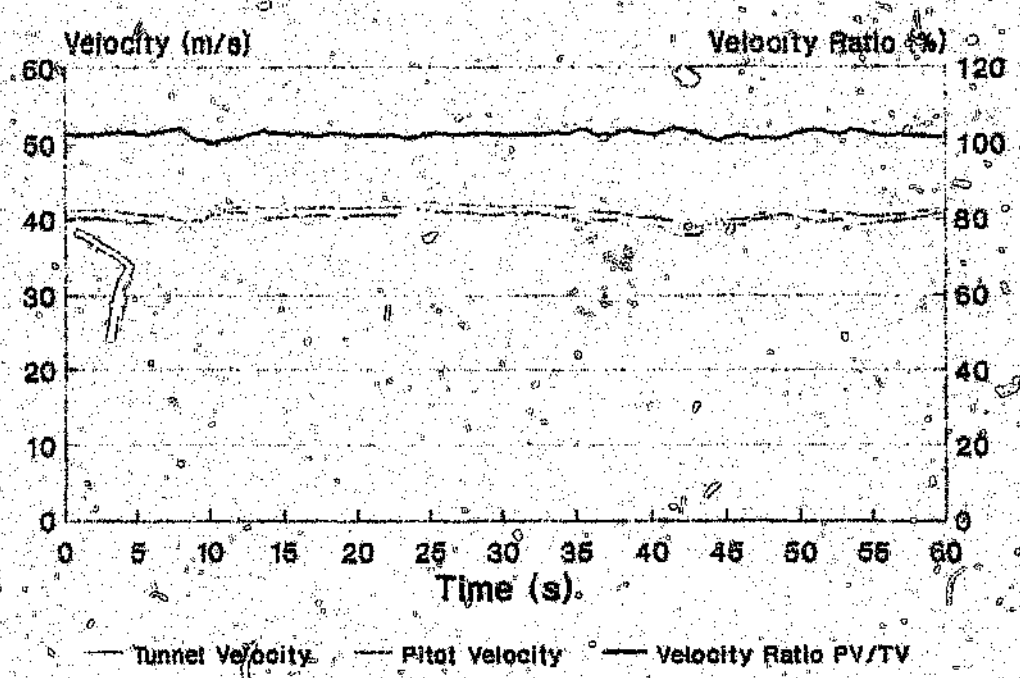

Figure 6.1: Test section velocity. y = -0.5m z = 0.15m

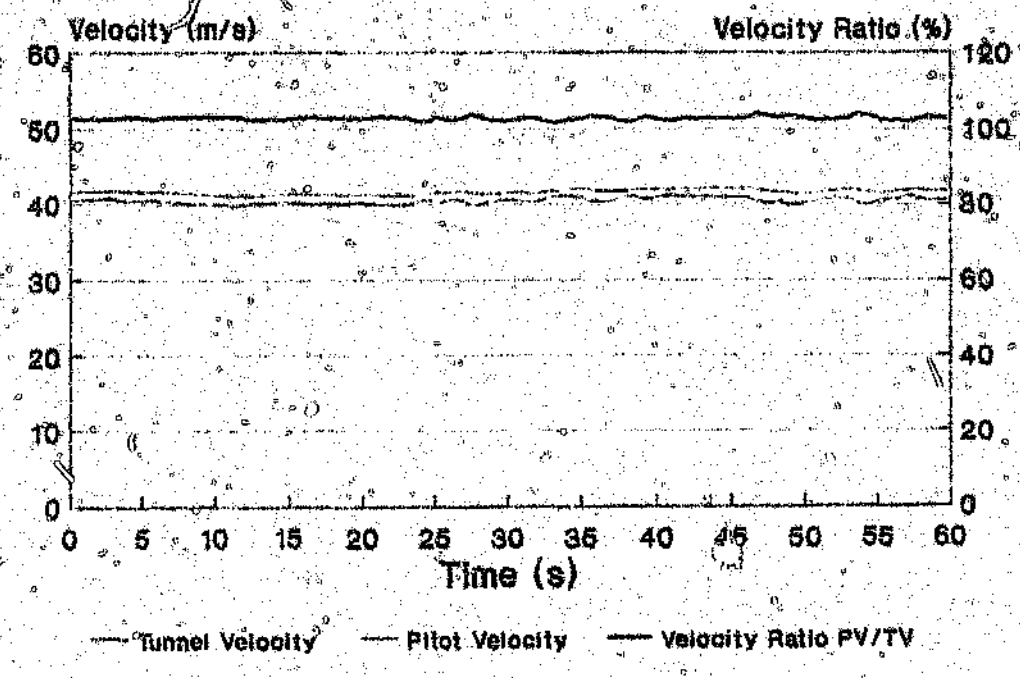

Figure 6.2: Test section velocity. y = -0.5m z = 0.05m

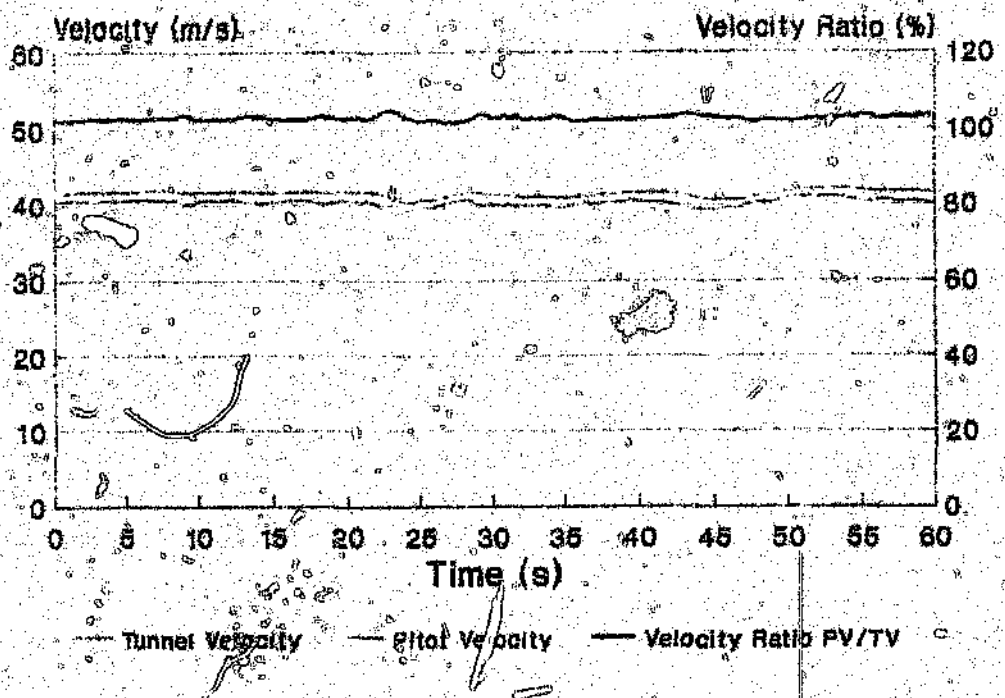

Figure 6.3: Test section velocity. y = -0.5m z = -0.05m

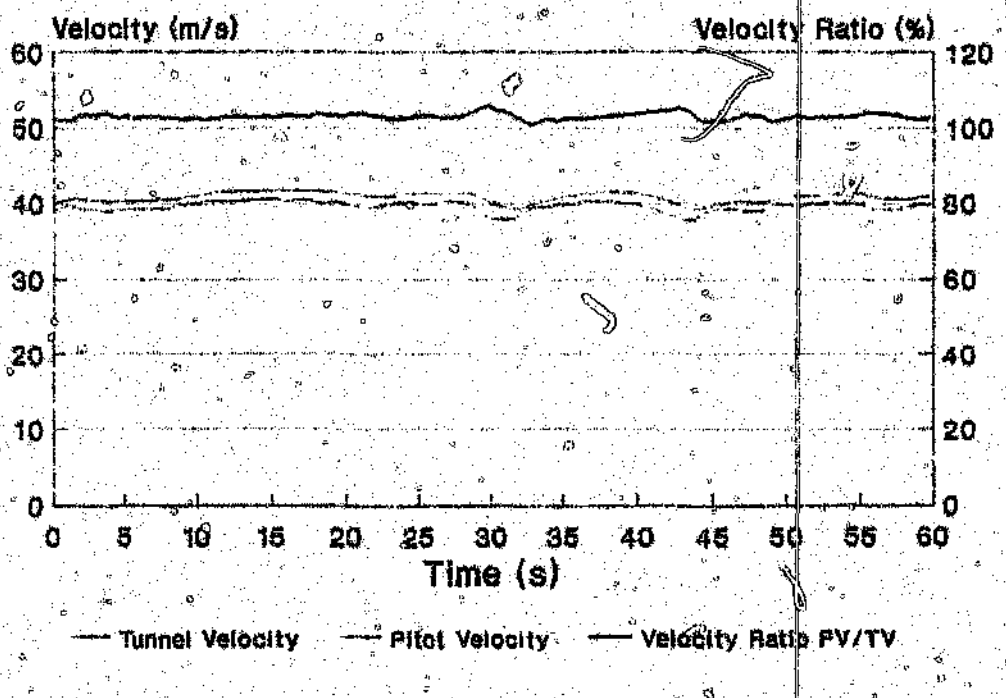

Figure 6.4: Test section velocity. y = -0.5m z = -0.15m

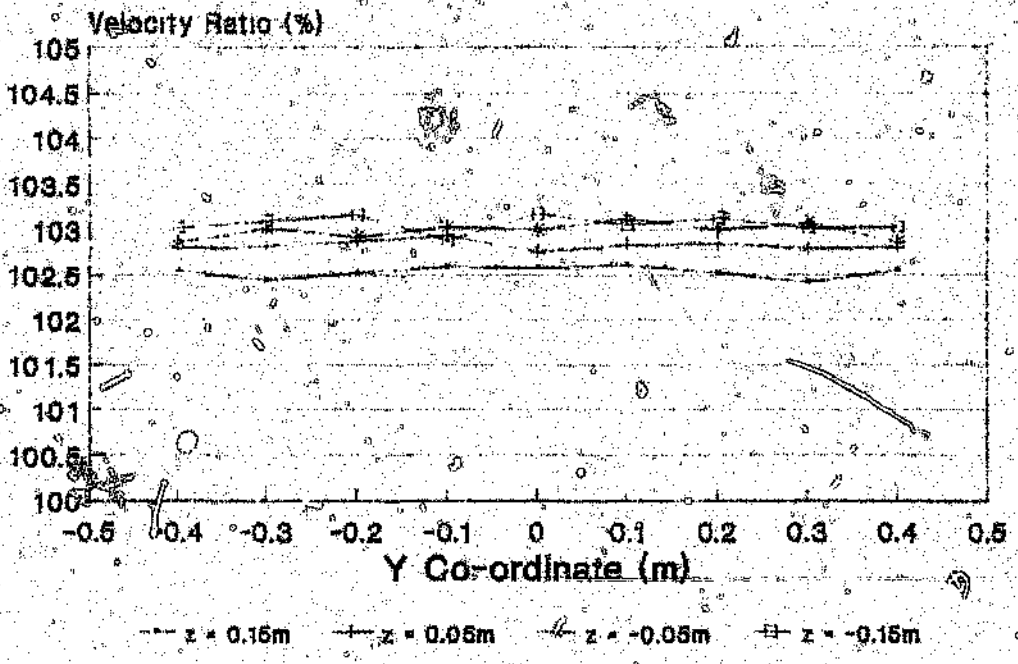

Figure 6.5: Test section velocity profiles.

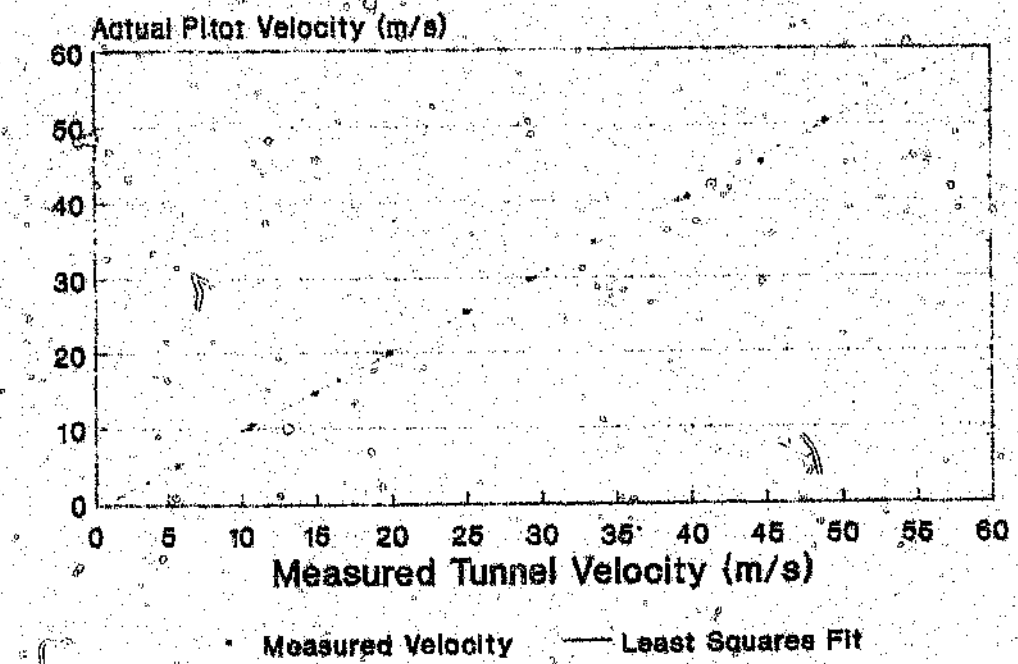

Figure 6.6: Tunnel speed calibration curve.

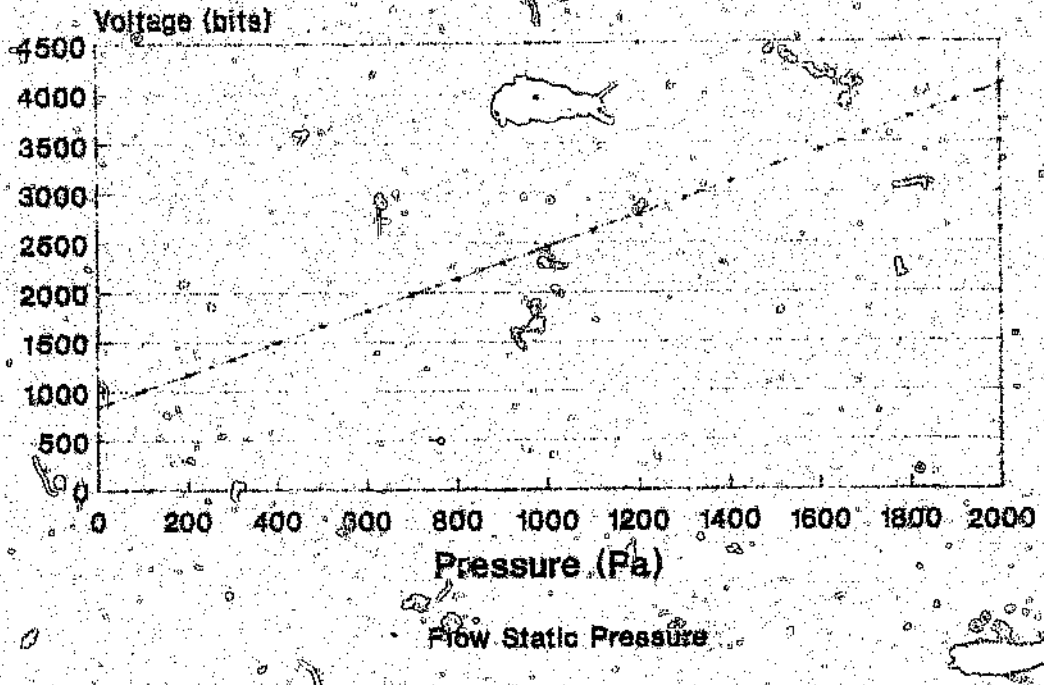

Figure 6.7: Pressure transducer calibration (p_1).

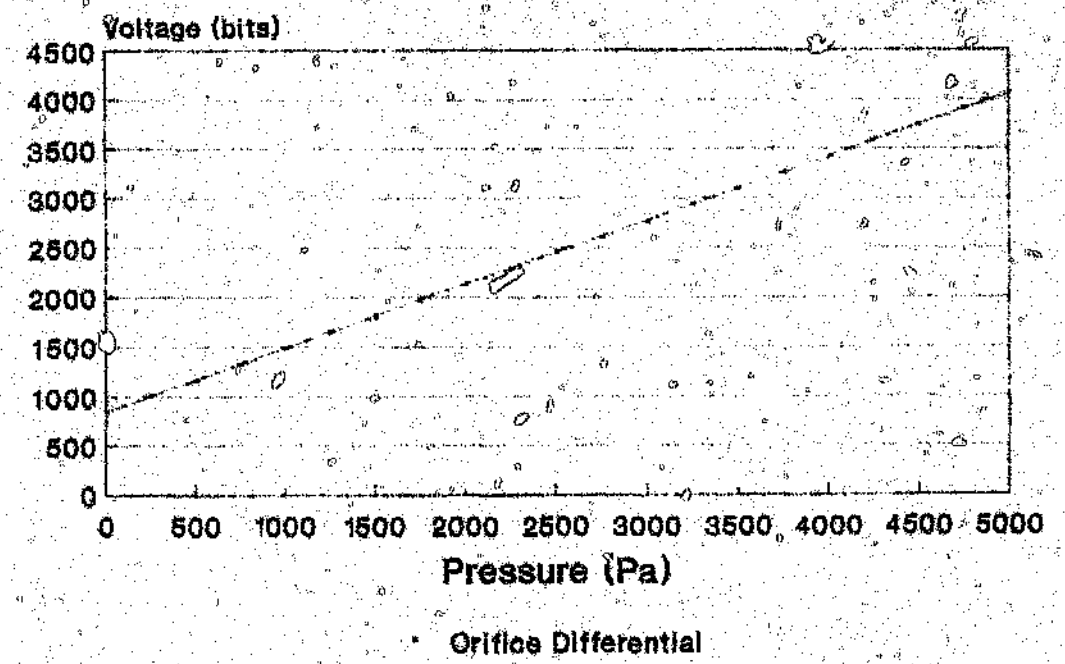

Figure 6.8: Pressure transducer calibration (p_2).

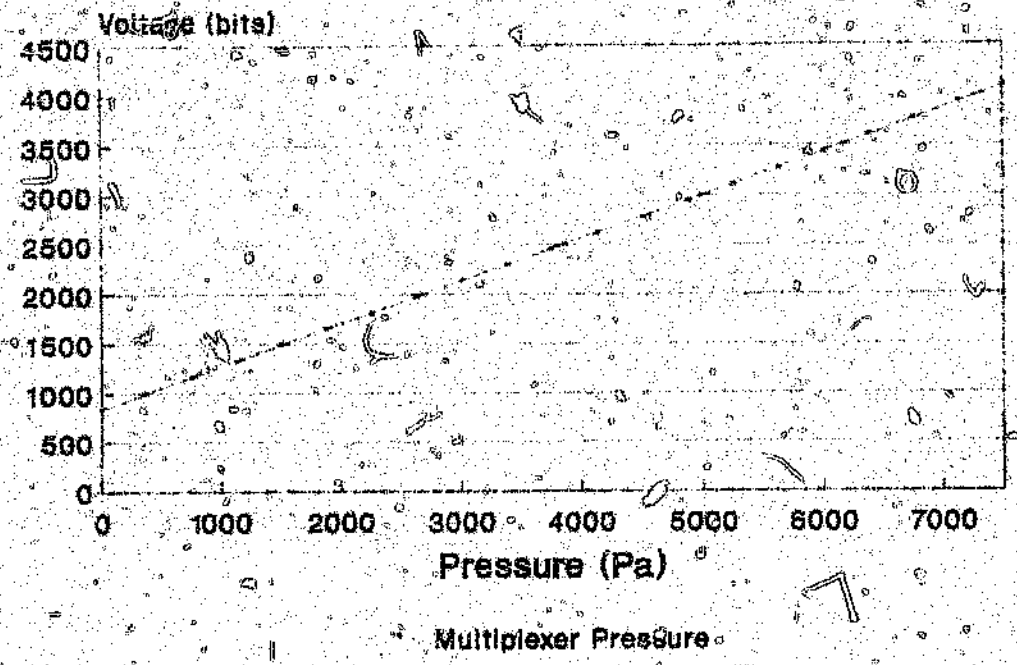

Figure 6.9: Pressure transducer calibration (p_3).

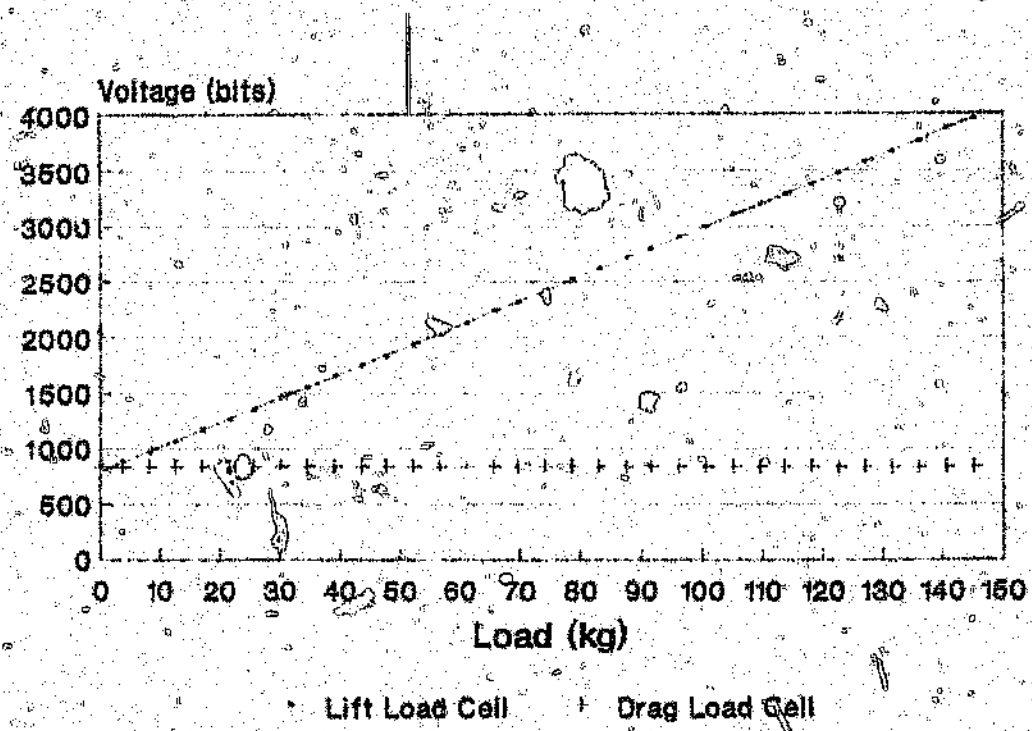

Figure 6.10: Lift load cell calibration curve.

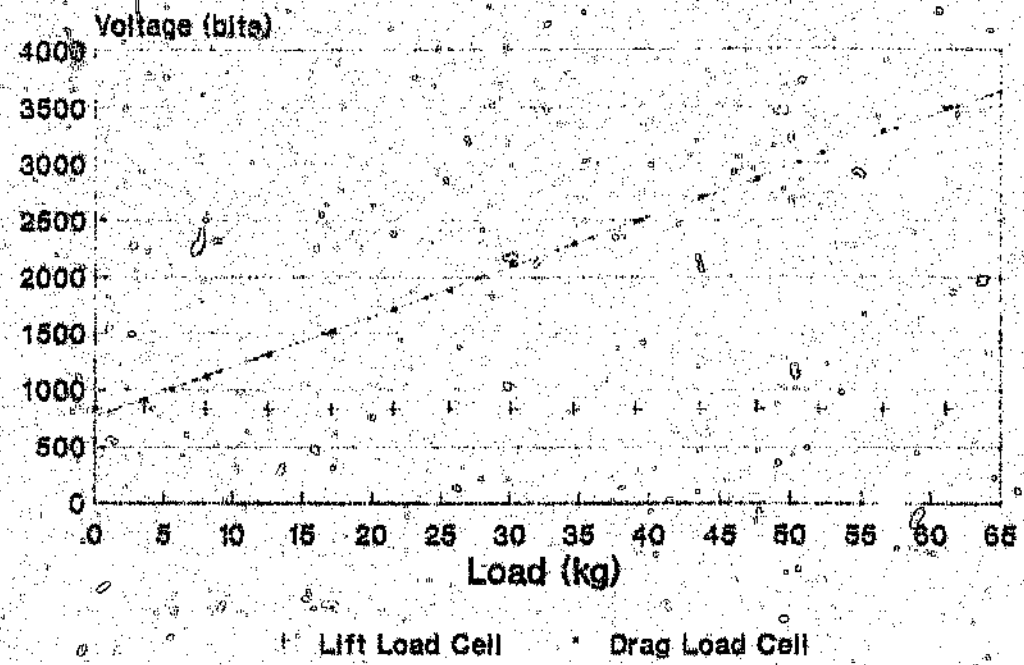

Figure 6.11: Drag load cell calibration curve.

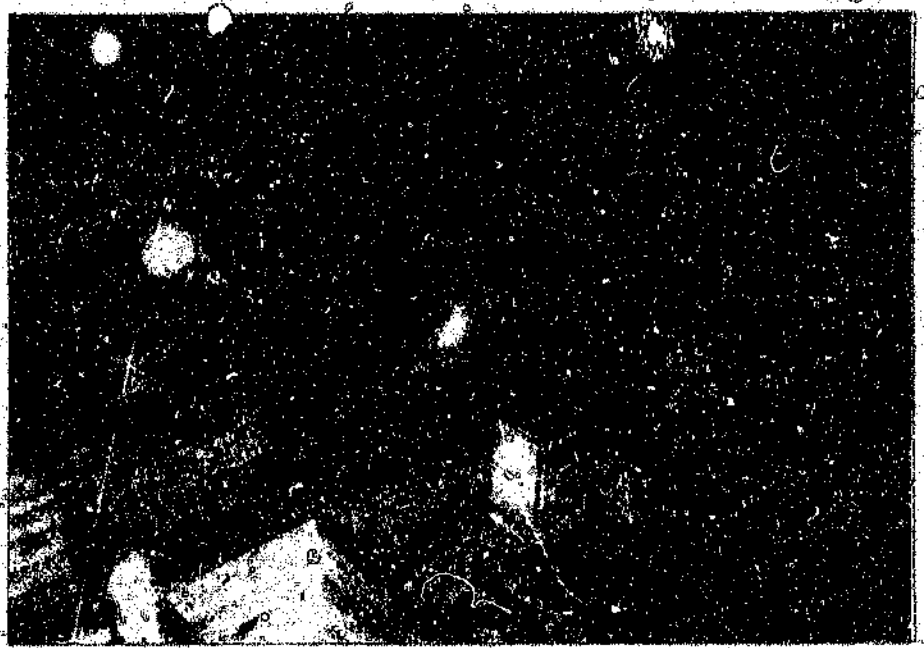

Plate 6,1: Velocity traverse arrangement.



Plate 6,2: Tuft screen right hand side.



Plate 6,3: Tuft screen left hand side.

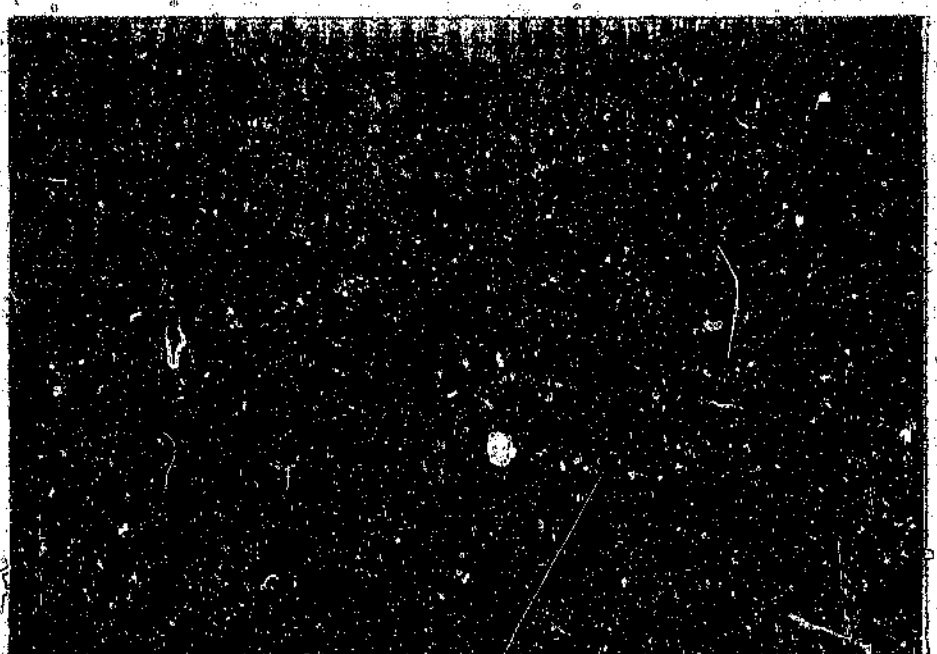

Plate 6,4: Corrected wall pressure distribution.

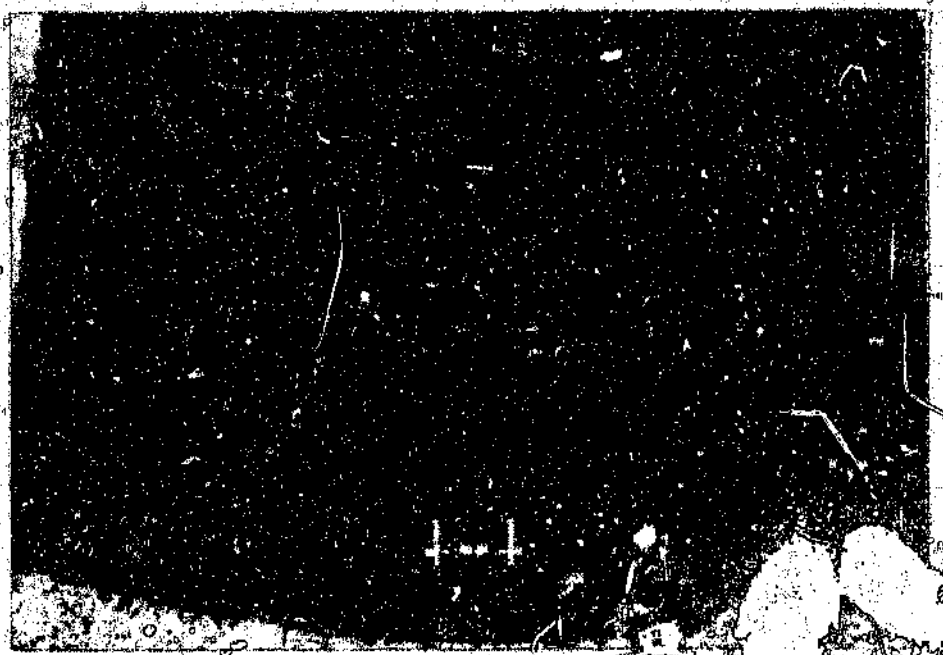

Plate 6,5: Top view of the calibration r

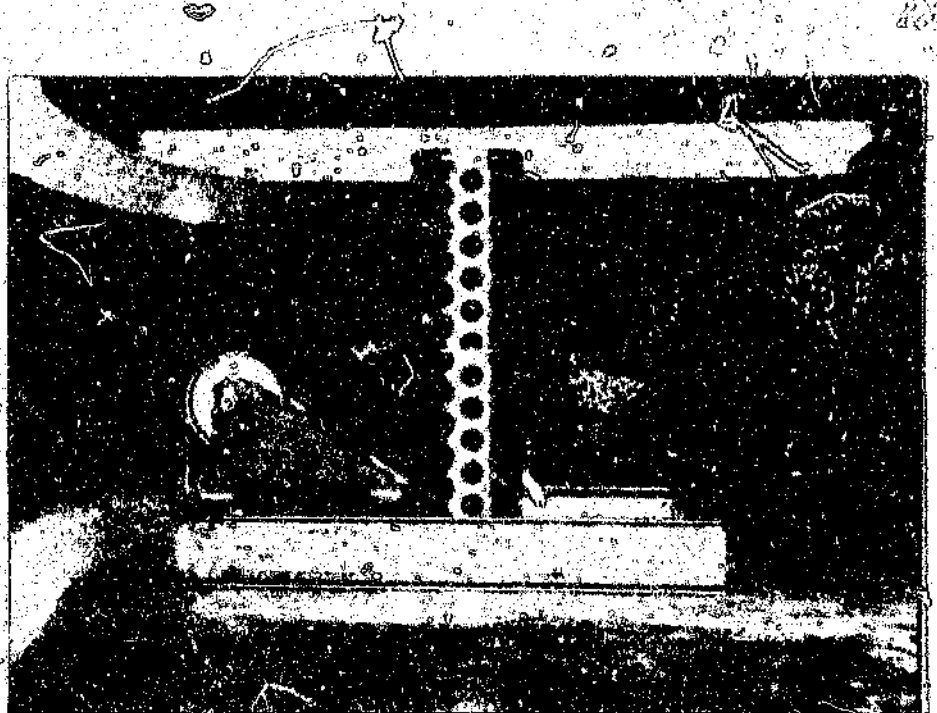

Plate 6,6: Front view of the calibration rig.

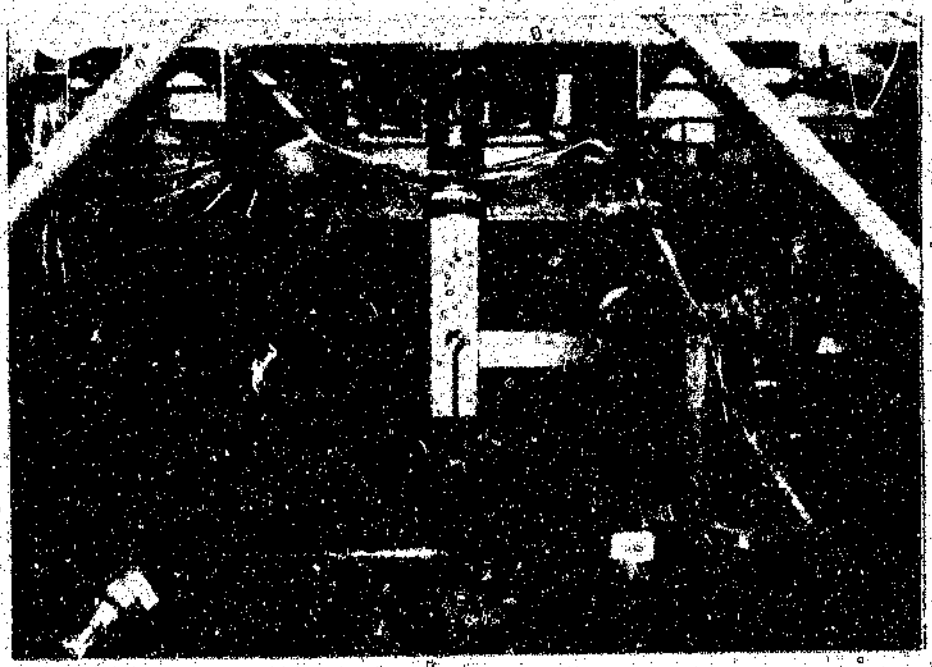

Plate 6,7: Loading the balance.

7 Experimental Procedure

A single test is defined as the acquisition of a series of data points with one particular model slot configuration. The test is usually done at a single tunnel speed. To obtain data points for various tunnel speeds, it is advisable to run different tests. This is done to avoid varying two independent variables in such a way as to result in a normalized data point that is identical to previous ones.

7.1 Tunnel initialization

1 Switch on all power supplies.
2 Boot up the PC and run MAINPROG.EXE.
3 Enter ambient pressure and temperature.
4 Enter orifice diameter and slot thickness.
5 Switch on the wall suction fan before running the tunnel drive fans. If this is not done, the flexible walls could get damaged by getting sucked into the tunnel.
6 Switch on the tunnel drive fans.
7 Switch on the CC blower.

7.2 Acquiring data

1 Enter the 4 predicted streamlining parameters, ie. tunnel speed U, C_l, C_d and slot flow rate Q, for a particular data point. If these are not predicted correctly, they can be altered in successive iterations. The walls will be positioned to the correct shape and real-time measured values of U, C_l, C_d and Q will appear on the screen.
2 The tests are usually done at constant tunnel speed, therefore adjust the tunnel drive fan speed until it matches the streamlining speed.
3 Adjust the CC flow rate by means of the discharge damper at the blower exit.
4 If the predicted streamlining parameters match the measured values of tunnel speed, C_l, C_d and slot flow rate, acquire the data point. If not, streamline the walls again with an updated set of streamlining parameters.

7.3 Terminating a test

1 Once sufficient data points have been acquired for a test, quit the operating program.

2 Switch off the CC blower and the tunnel drive fans.

3 Once the tunnel flow has stopped, switch off the wall suction fan.

4 If further tests are required, adjust the model, etc. When running MAINPROG.EXE again, make sure the flow in the tunnel has stopped completely since zero lift and drag readings are taken when the program is initialized.

5 If no further tests are required, switch off all power supplies as well as the PC.

8 Results

8.1 Adaptive Wall Wind Tunnel

8.1.1 Wall Streamlining Strategy

The streamlining data is given for two different tunnel speeds, and can be seen in Plate 8,1 through to Plate 8,5 for a tunnel speed of 30 m/s, and Plate 8,6 through to Plate 8,9 for a tunnel speed of 40 m/s. The plates display the measured wall pressure distributions by means of a multi-tube manometer connected to the wall pressure tappings. Superimposed on the measured pressure distribution is a predicted pressure distribution, represented by the multi-coloured curves.

8.2 Tests on CC Cylinder

8.2.1 Test Schedule

Table 8.1 shows the tests that were performed, in the sequence they were performed. Also shown are the tunnel speed, slot locations and slot sizes. θ is measured from the cylinder leading edge, having values ranging between 0° and 180° on the cylinder suction (upper) surface. Test number 26 is a drag test at tunnel speeds ranging from 0 to 55 m/s.

Table 8,1: Schedule of tests.

No	U	θ_1	θ_2	θ_3	θ_4	t_1	t_2	t_3	t_4	t_{tot}
	m/s	deg	deg	deg	deg	mm	mm	mm	mm	mm
001	25	70	105	140	175	1	1	1	1	4
002	30									
003	35									
004	25	70	105	140	175	2	2	2	2	8
005	30									
006	35									
007	25	70	105	140	175	3	3	3	3	12
008	30									
009	35									

No	U	θ_1	θ_2	θ_3	θ_4	t_1	t_2	t_3	t_4	t_{tot}
010	25	70	105	140	175	4	4	4	4	16
011	30									
012	35									
013	25	70	105	140	175	5	5	5	5	20
014	30									
015	35									
016	30	70	105	140	-	1	1	1	-	3
017	35									
018	30	70	105	140	-	2	2	2	-	6
019	35									
020	30	70	105	140	-	3	3	3	-	9
021	35									
022	30	70	105	140	-	4	4	4	-	12
023	35									
024	30	70	105	140	-	5	5	5	-	15
025	35									
026	-	-	-	-	-	-	-	-	-	-
027	20	70	105	140	-	5	5	5	-	15
028	25									
029	30									
030	35									
031	15	70	105	140	-	5	5	5	-	15
032	25	70	-	140	-	2	-	1	-	3
033	25	70	-	140	-	1	-	2	-	3
034	25	70	-	140	-	3	-	3	-	6
035	25	70	105	140	-	2	3	4	-	9
036	25	70	105	140	-	4	3	2	-	9

No	U	θ_1	θ_2	θ_3	θ_4	t_1	t_2	t_3	t_4	t_{tot}
037	25	70	105	140	-	3	4	5	-	12
038	25	70	105	140	-	5	4	3	-	12
039	25	50	85	120	-	3	3	3	-	9
040	25	60	95	130	-					
041	25	70	105	140	-					
042	25	80	115	150	-					
043	25	90	125	160	-					
044	25	50	85	120	-	3	-	3	-	6
045	25	60	95	130	-					
046	25	70	105	140	-					
047	25	80	115	150	-					
048	25	90	125	160	-					
049	25	100	135	170	-					

8.2.2 Processed Data

Data is processed by the tunnel PC before it is stored on disk. The unprocessed data is stored in the same file, but will not be presented in this report. The processed data is presented in the form of curves. Only curves relevant to the discussion have been presented.

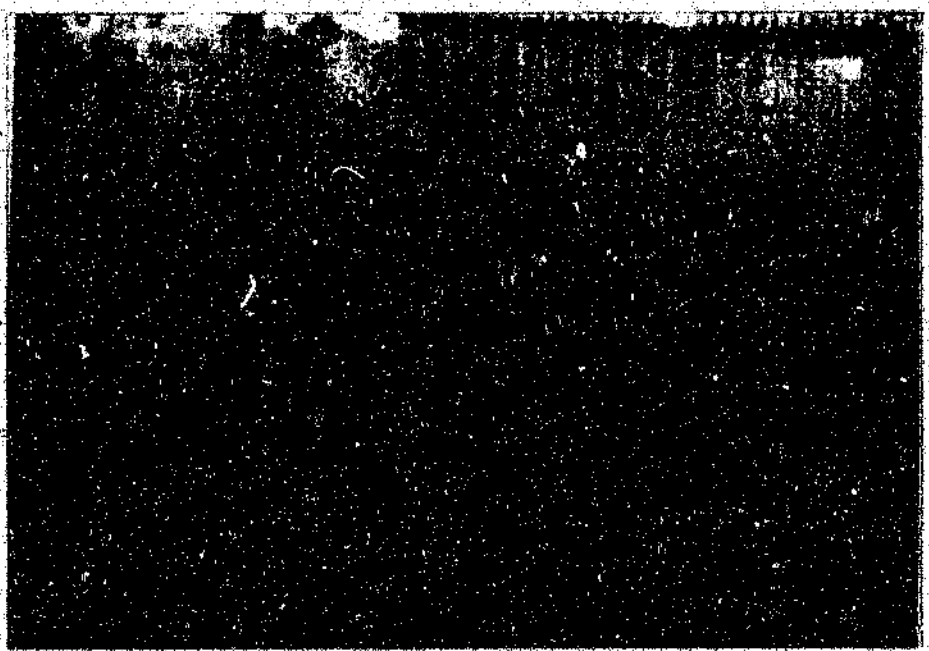

Plate 8,1: Wall pressures U=30 C_i=0.

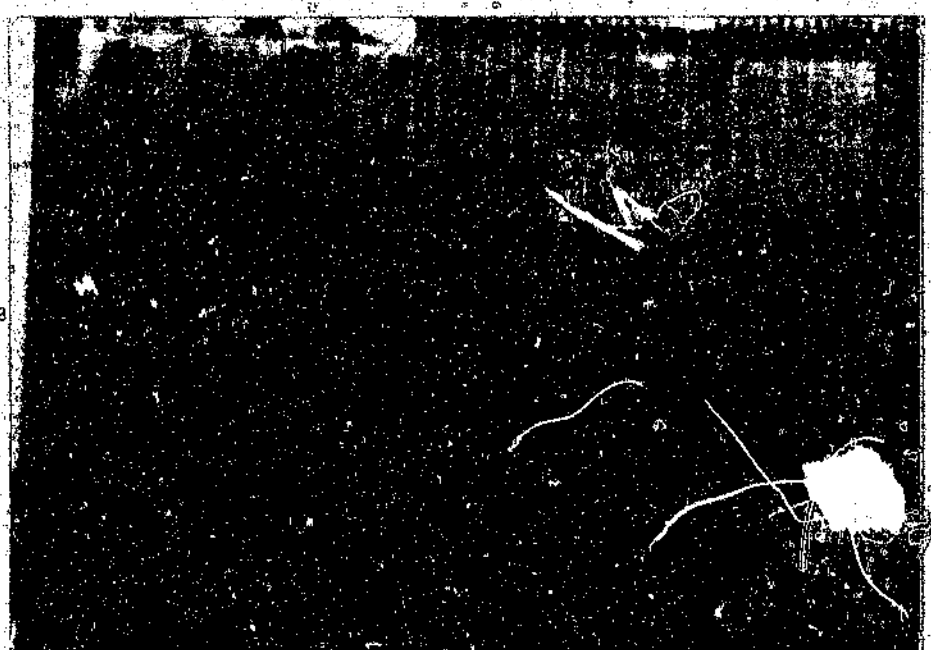

Plate 8,2: Wall pressures U=30 C_i=1.

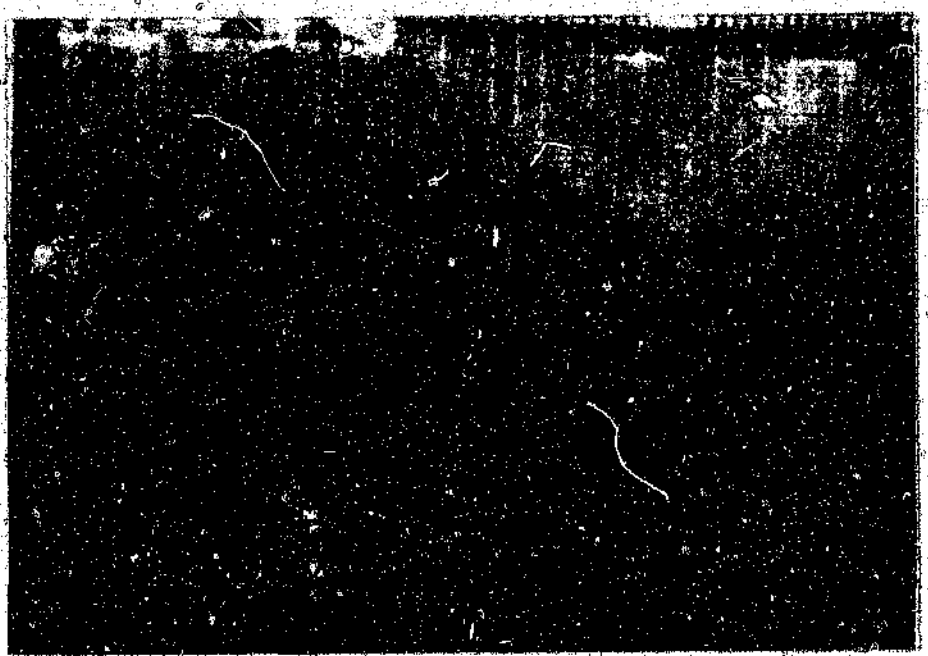

Plate 8,3: Wall pressures U=30 C_i=2.

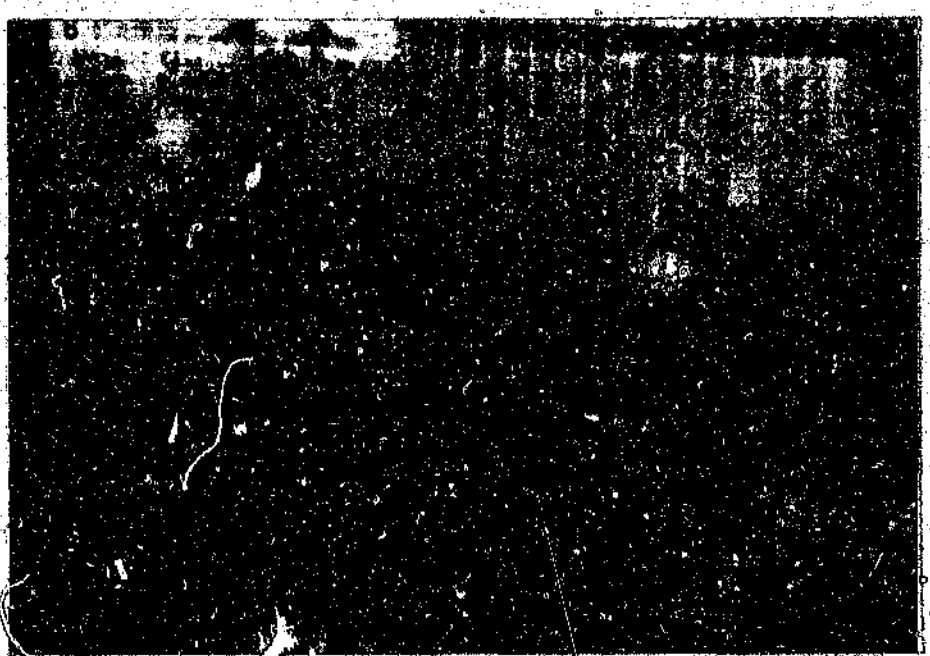

Plate 8,4: Wall pressures U=30 C_i=3.

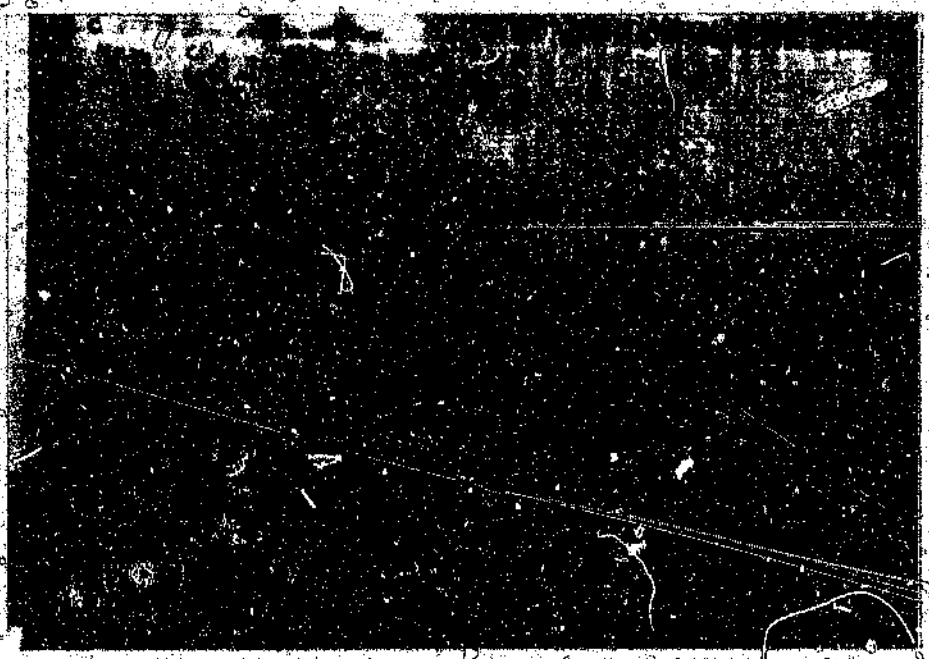

Plate 8,5: Wall pressures U=30 C_i=4.

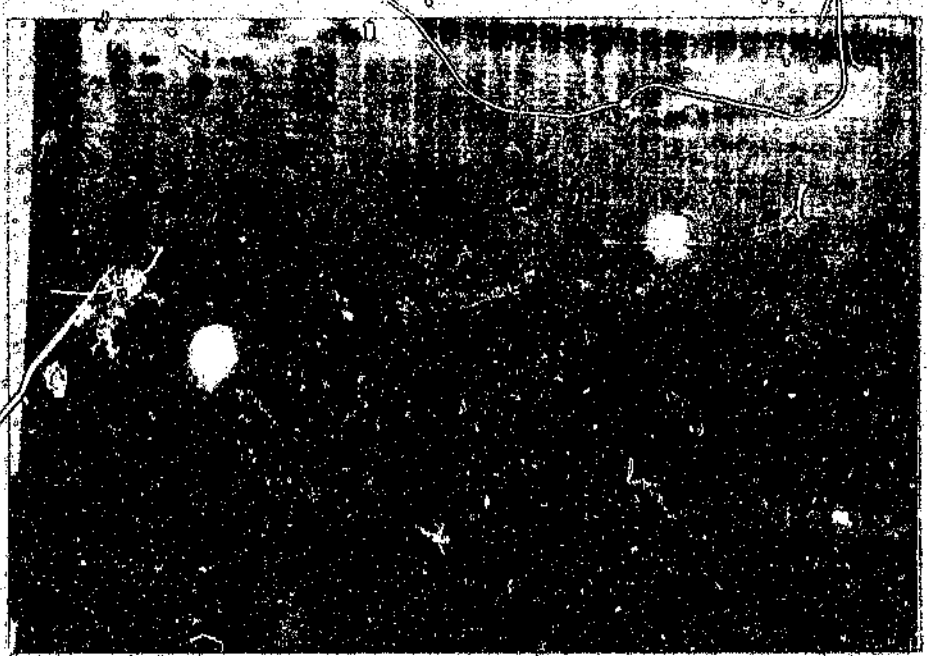

Plate 8,6: Wall pressures U=40 C_i=0.

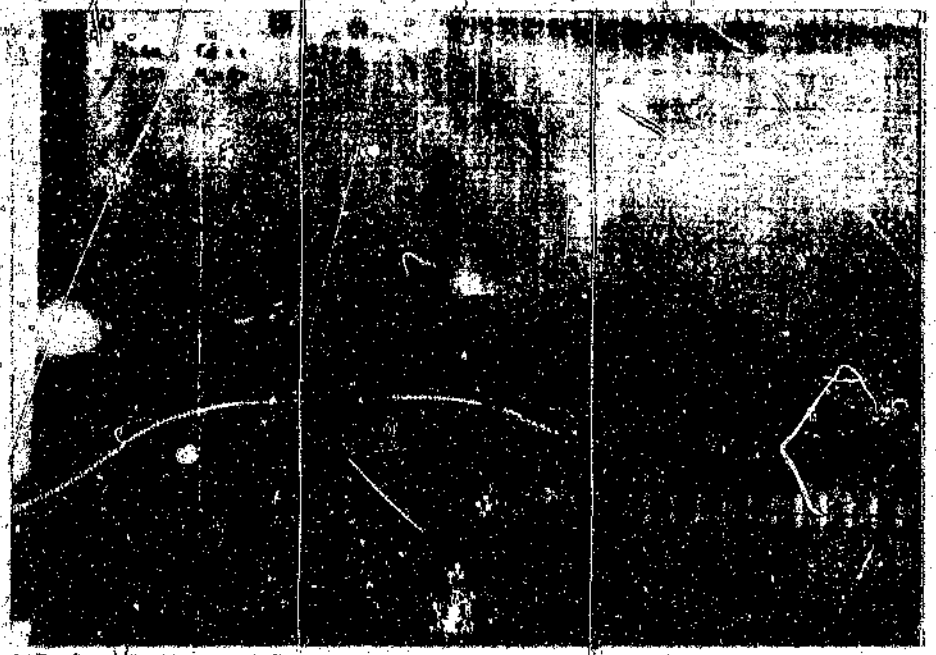

Plate 8,7: Wall pressures U=40 C_i=1.

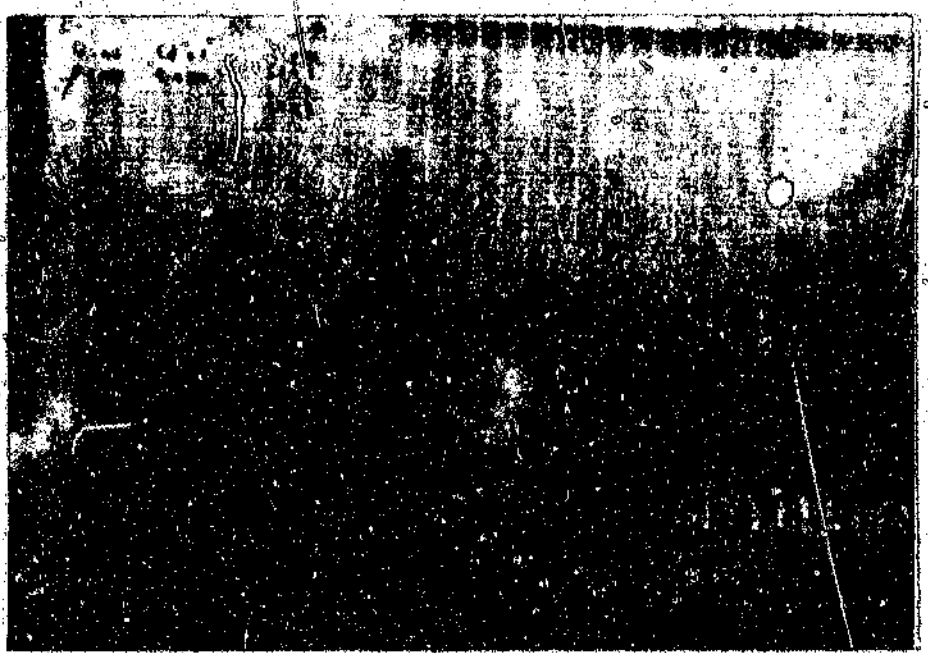

Plate 8,8: Wall pressures U=40 C_i=2.



Plate 8,9: Wall pressures U=40 C_i=3

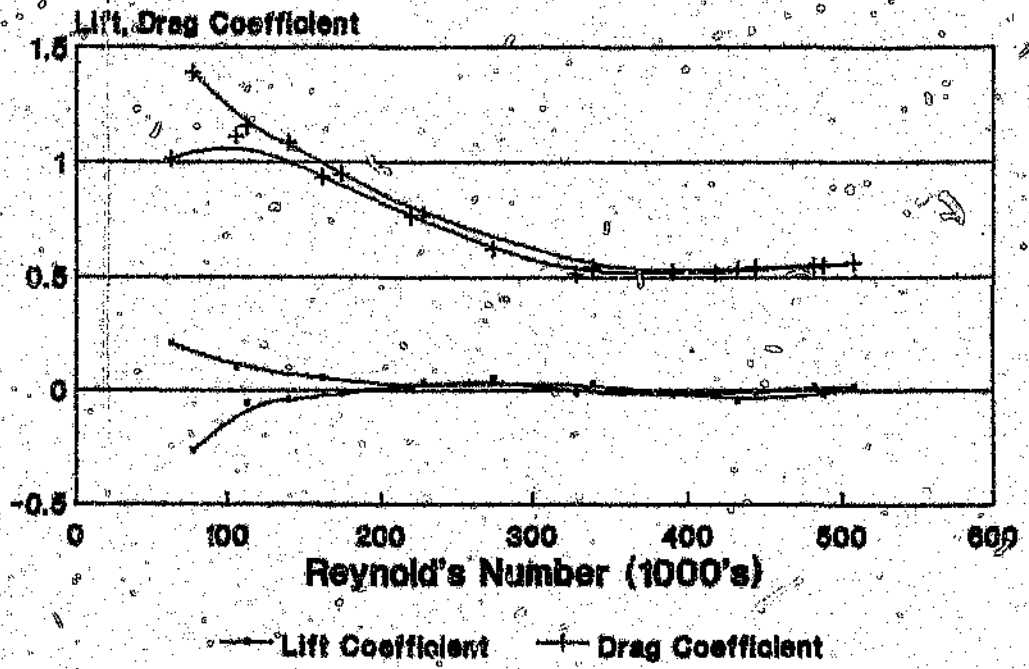

Figure 8.1: variation of C_d with Re_d.

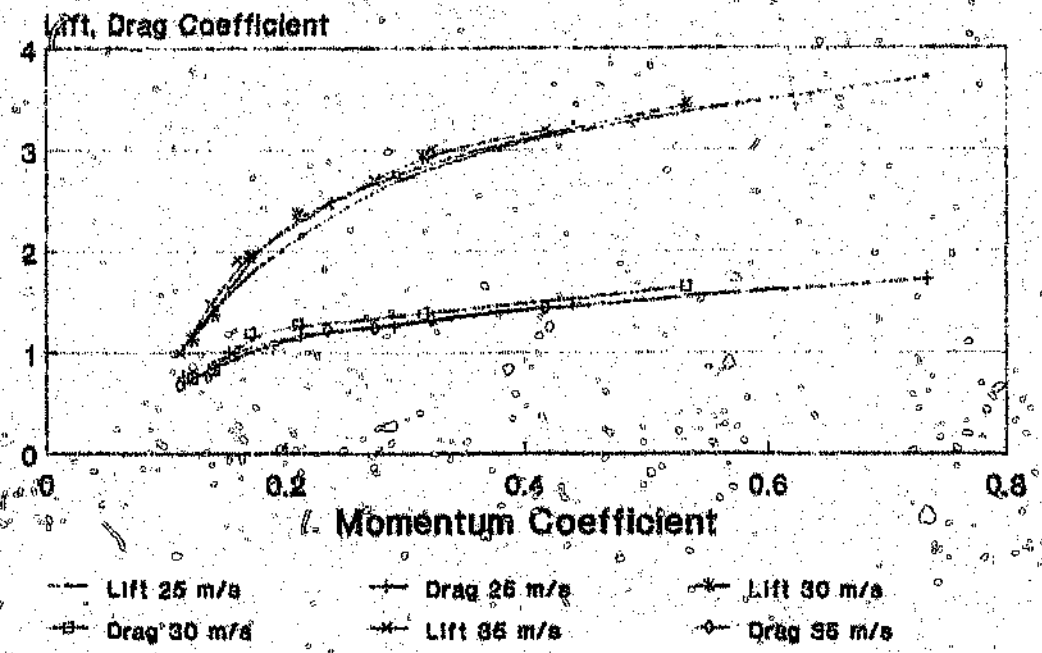

Figure 8.2: C_l, C_d vs C_μ. 70°,1; 105°,1; 140°,1; 175°,1.

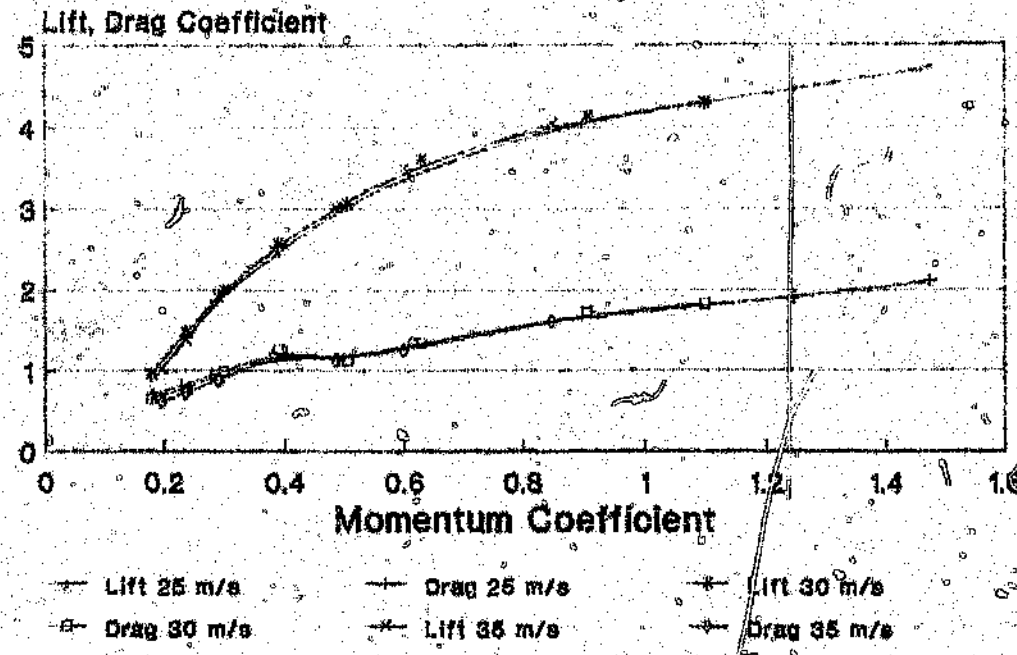

Figure 8.3: C_l, C_d vs C_μ. 70°,2; 105°,2; 140°,2; 175°,2.

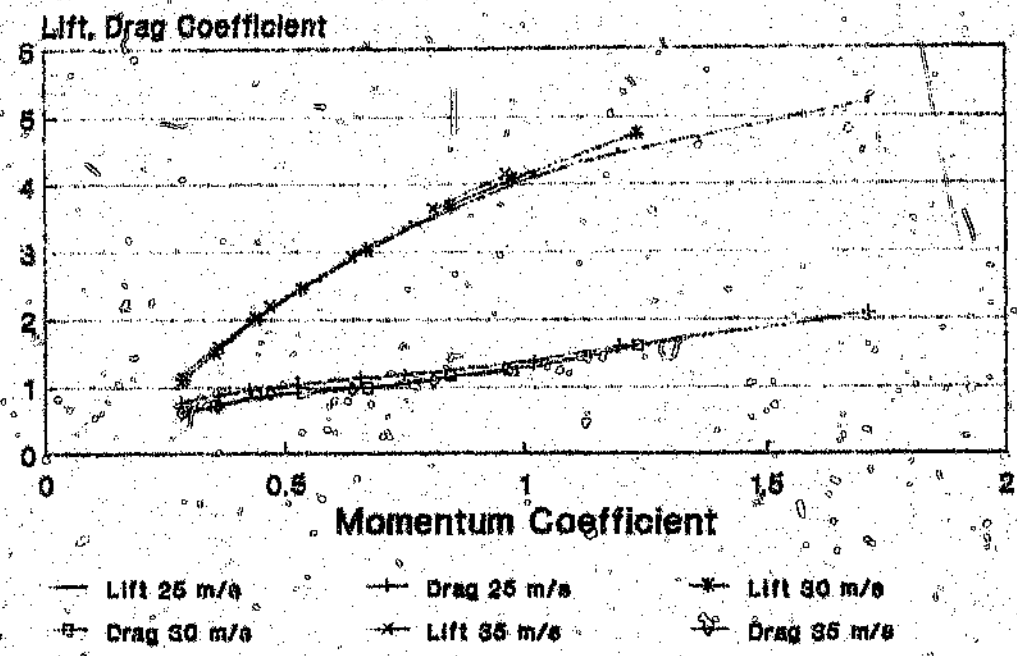

Figure 8.4: C_l, C_d vs C_μ. 70°,3; 105°,3; 140°,3; 175°,3.

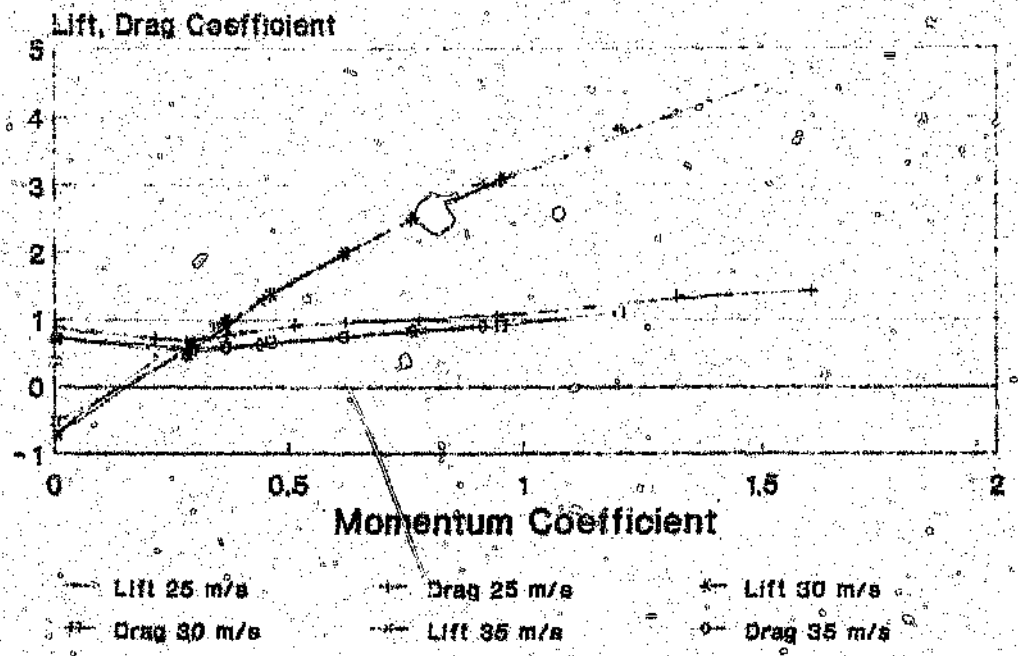

Figure 8.5: C_l, C_d vs C_μ. 70°,4; 105°,4; 140°,4; 175°,4.

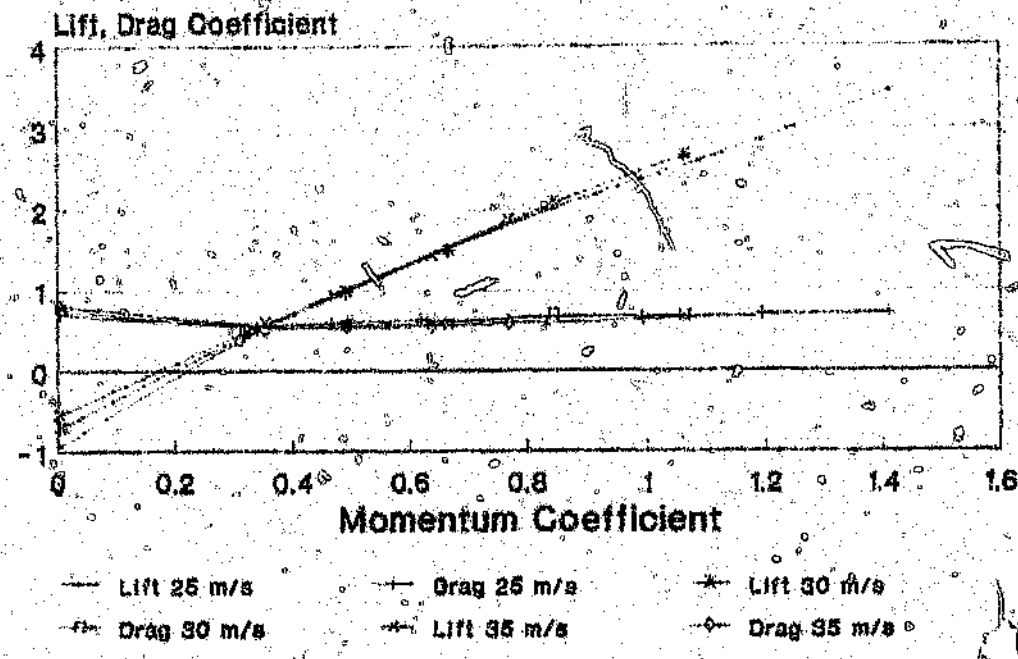

Figure 8.6: C_l, C_d vs C_μ. 70°,5; 105°,5; 140°,5; 175°,5.

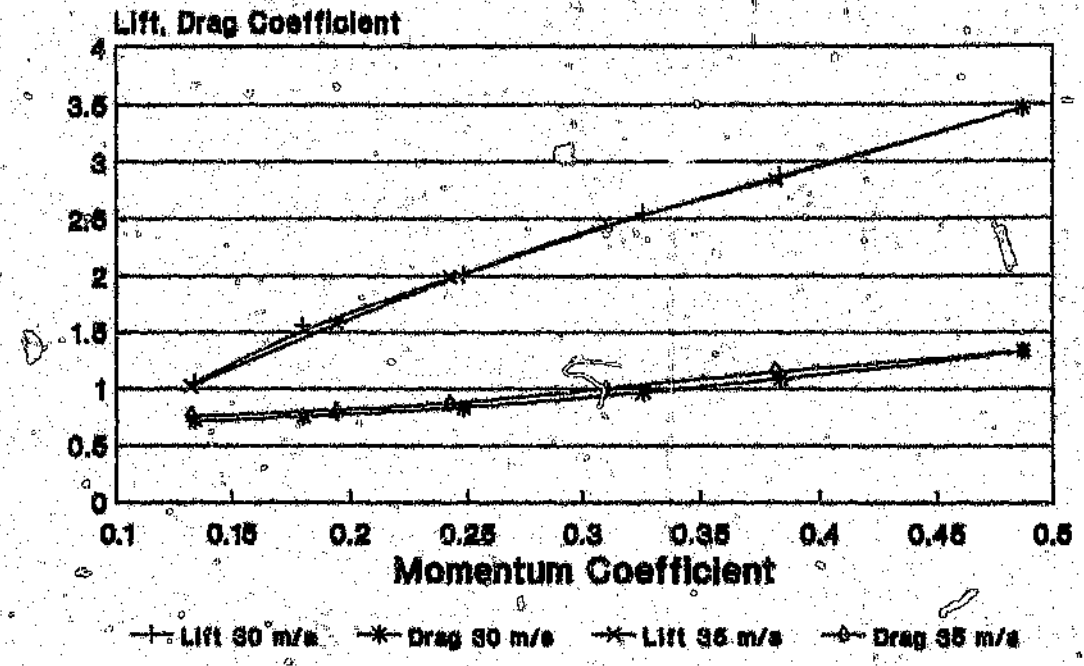

Figure 8.7: C_l, C_d vs C_μ. 70°,1; 105°,1; 140°,1.

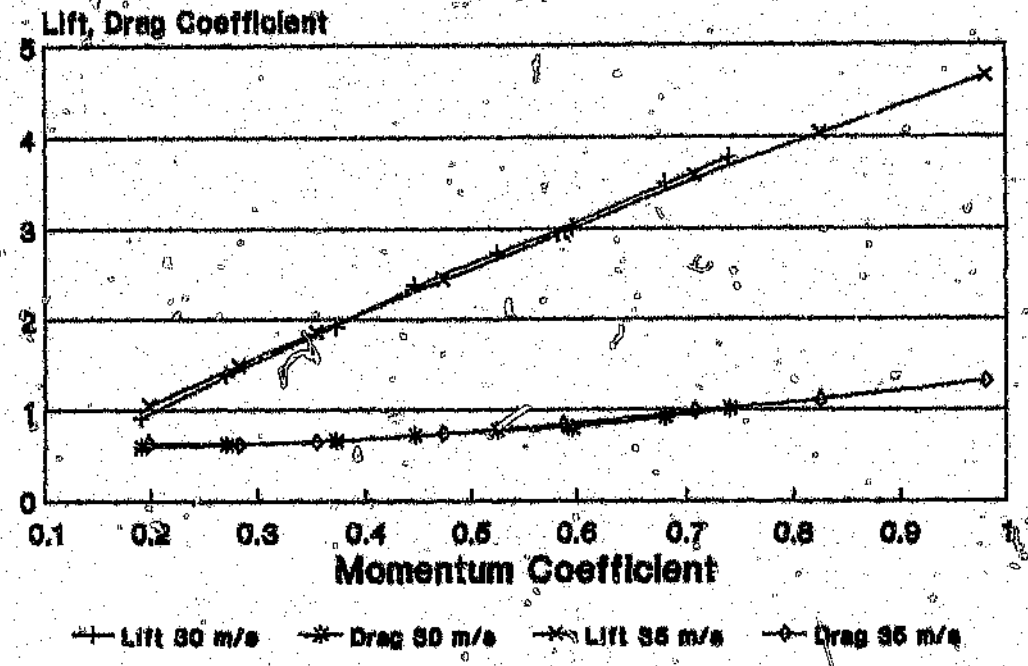

Figure 8.8: C_l, C_d vs C_μ. 70°,2; 105°,2; 140°,2.

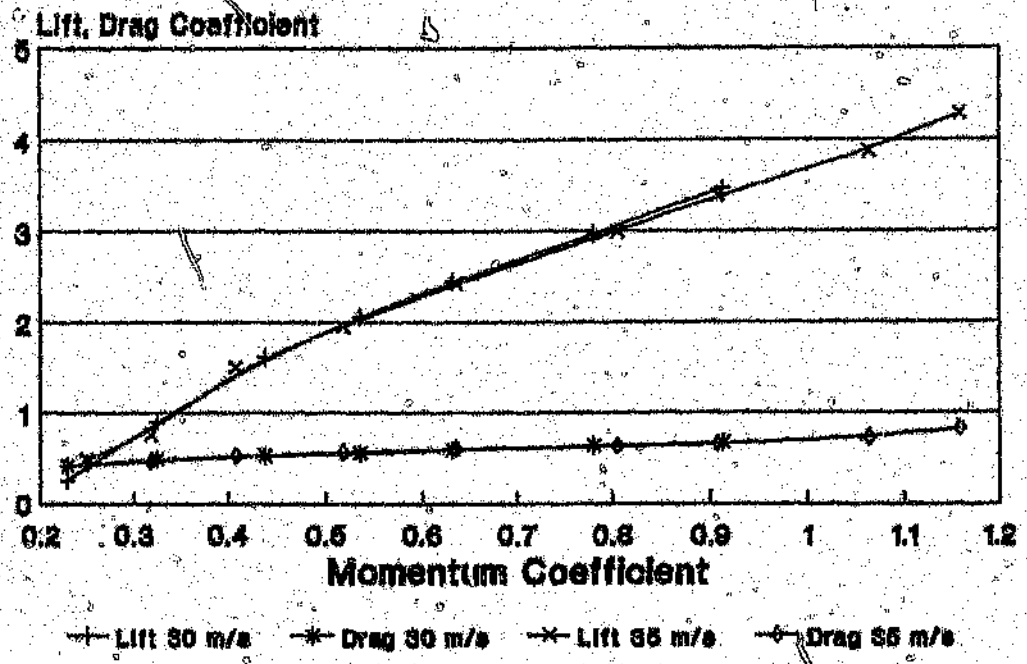

Figure 8.9: C_l, C_d vs C_μ. 70°,3; 105°,3; 140°,3.

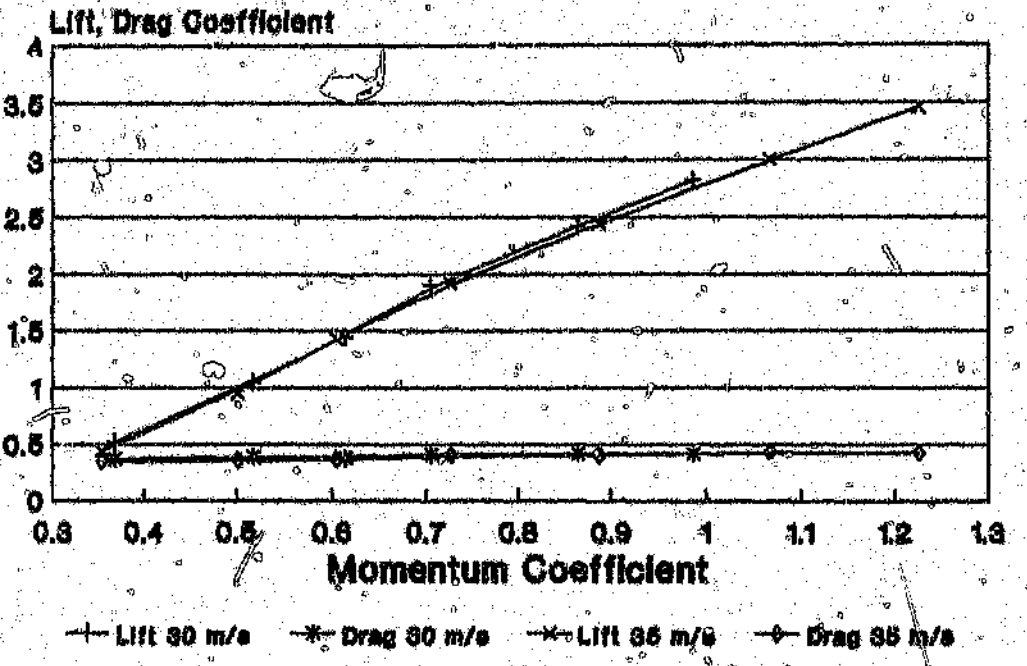

Figure 8.10: C_l, C_d vs C_μ. 70°,4; 105°,4; 140°,4.

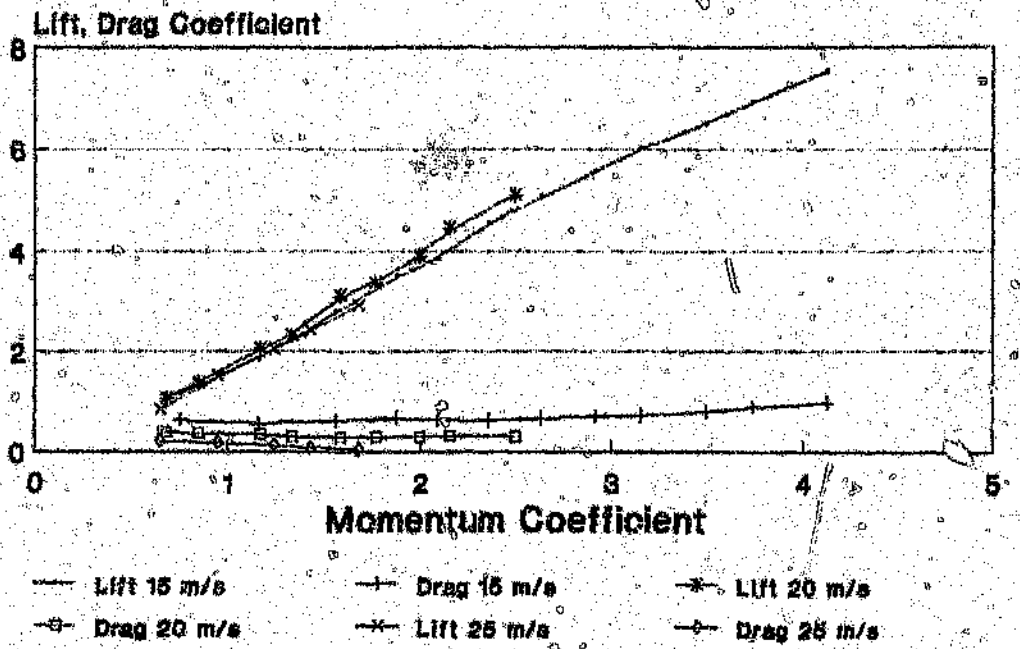

Figure 8.11: C_l, C_d vs C_μ. 70°,5; 105°,5; 140°,5.

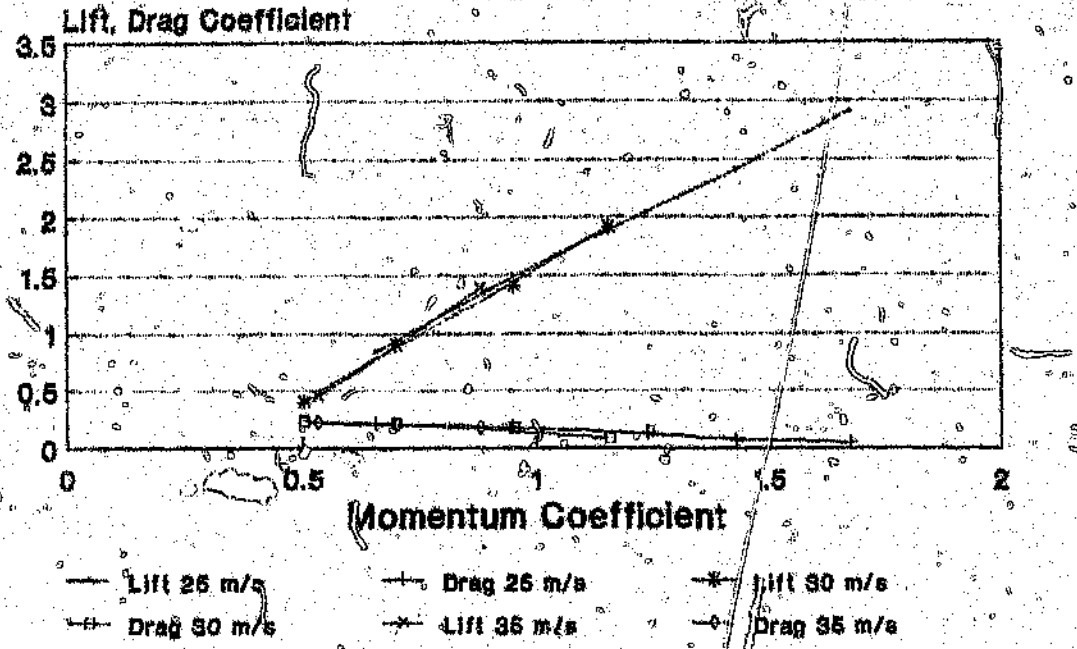

Figure 8.12: C_l, C_d vs C_μ. 70°,5; 105°,5; 140°,5.

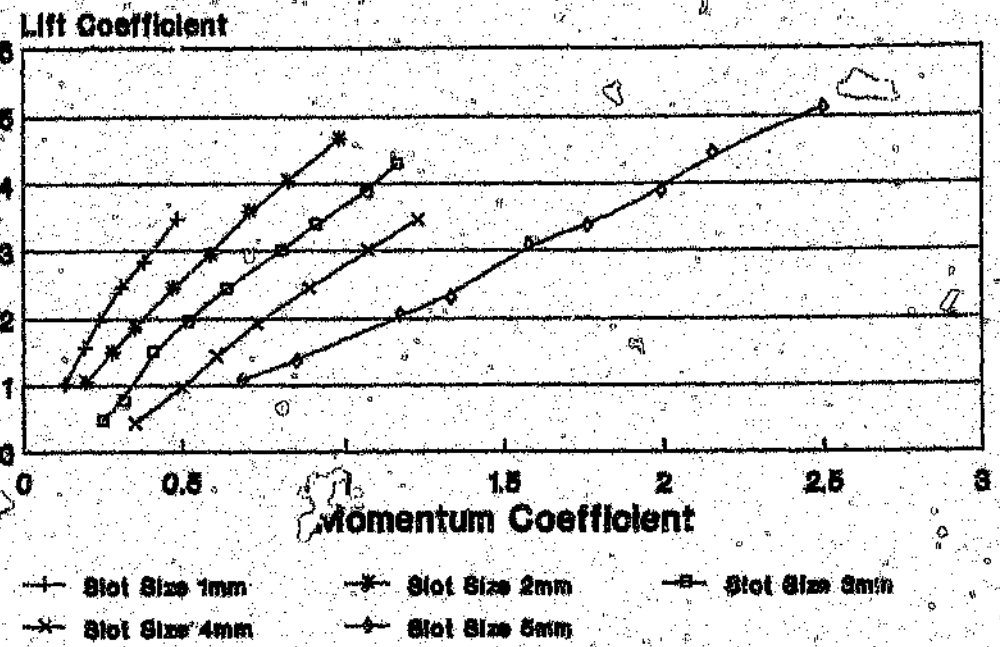

Figure 6.13: C_l vs C_μ. 3 slots. 70°; 105°; 140°.

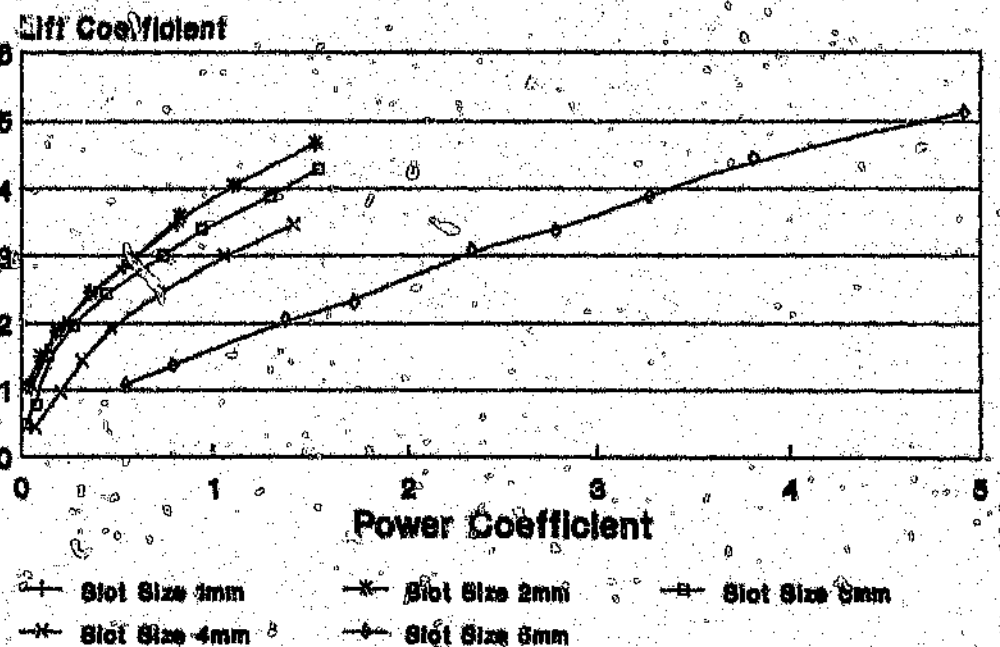

Figure 6.14: C_l vs C_{pow}. 3 slots. 70°; 105°; 140°.

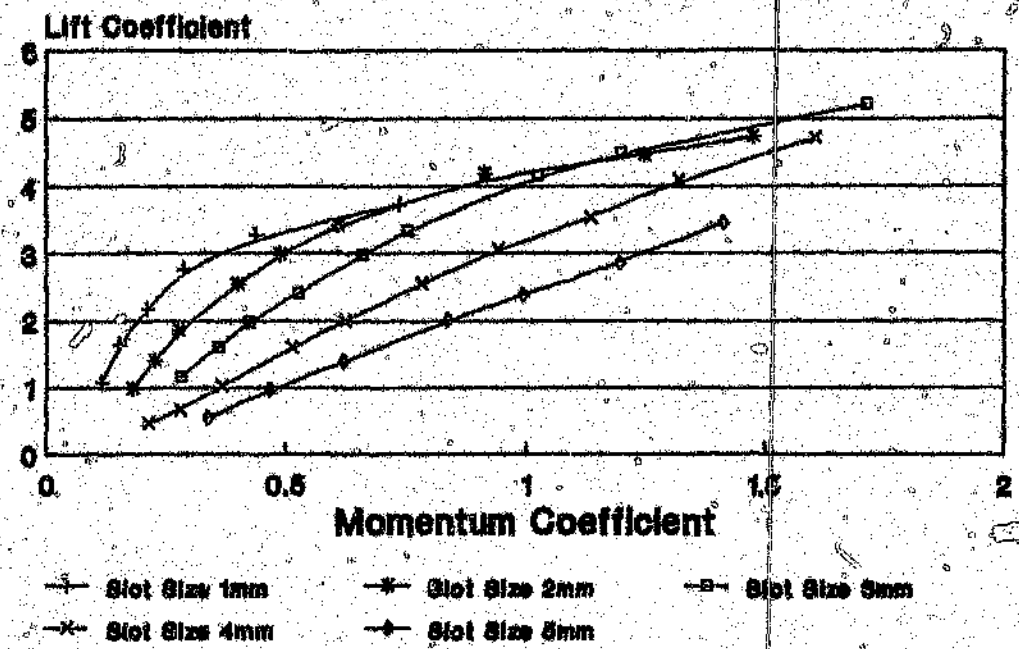

Figure 8.15: C_l vs C_p. 4 slots. 70°; 105°; 140°; 175°.

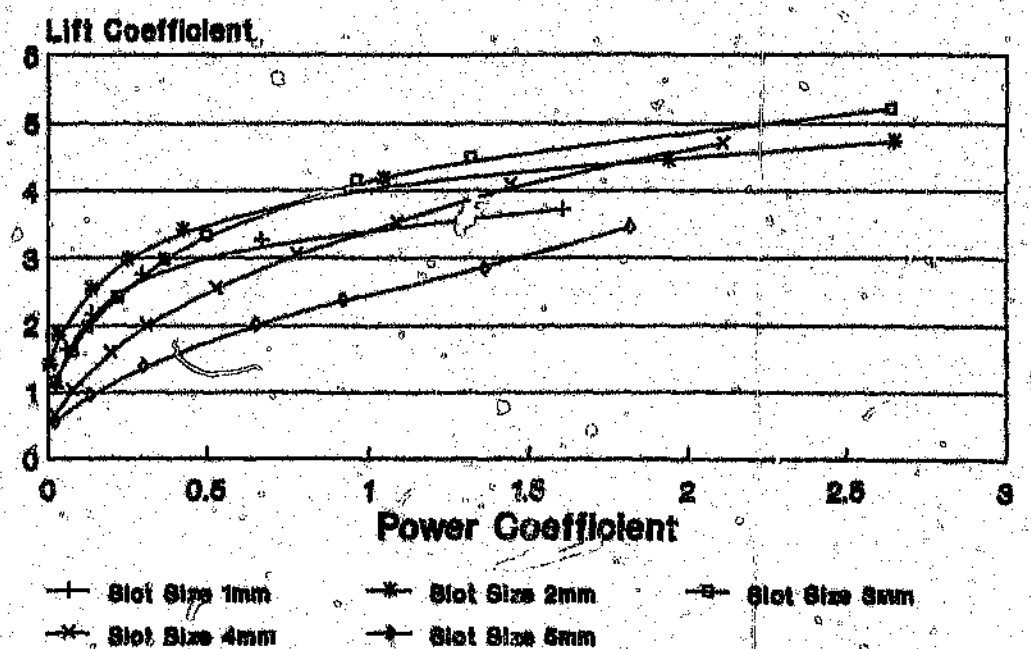

Figure 8.16: C_l vs C_{pow}. 4 slots. 70°; 105°; 140°; 175°.

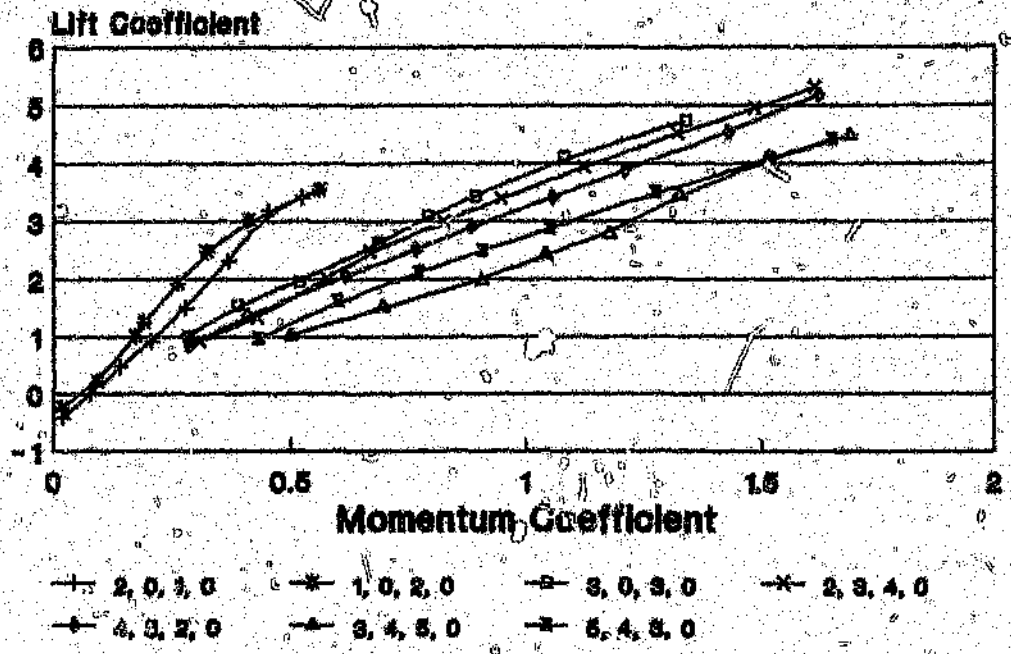

Figure 8.17: C_l vs C_μ. Slots at 70°; 105°; 140°; 175°.

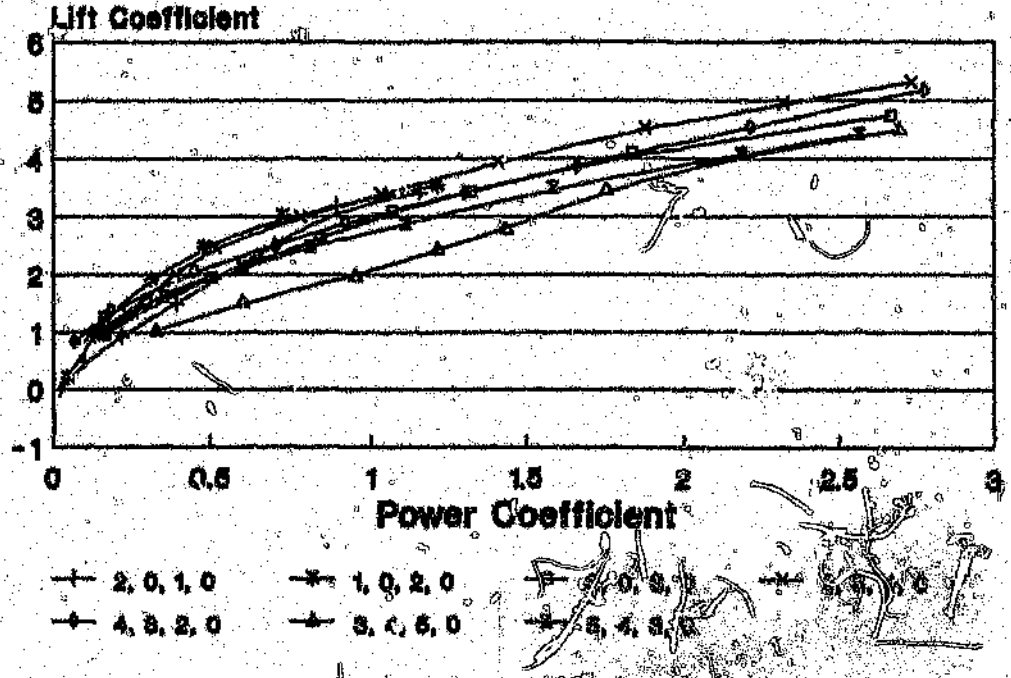

Figure 8.18: C_l vs C_{pow}. Slots at 70°; 105°; 140°; 175°.

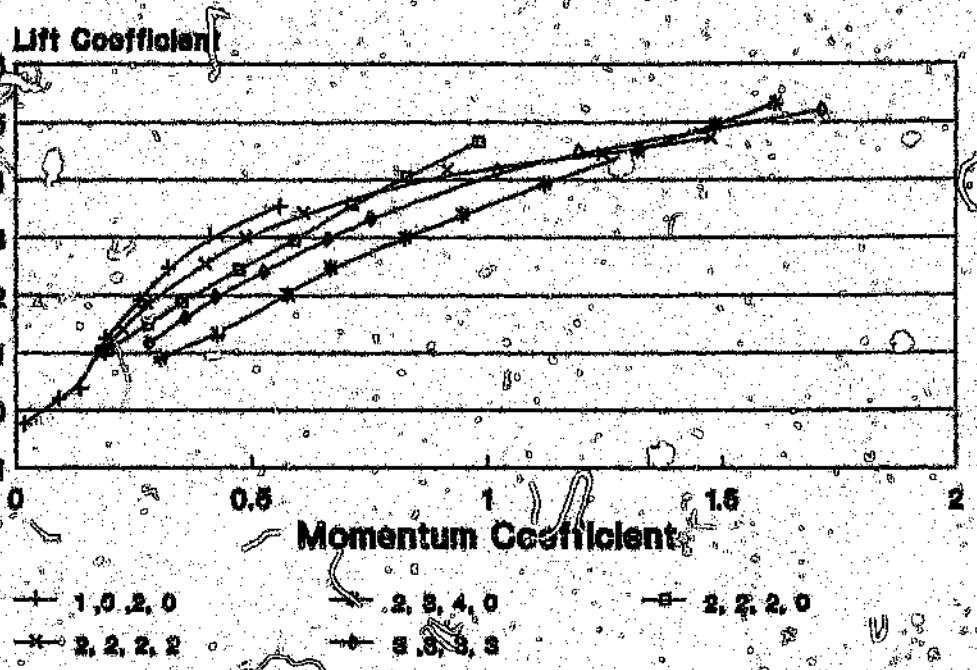

Figure 8.19: C_l vs C_μ. Slots at 70°; 105°; 140°; 175°.

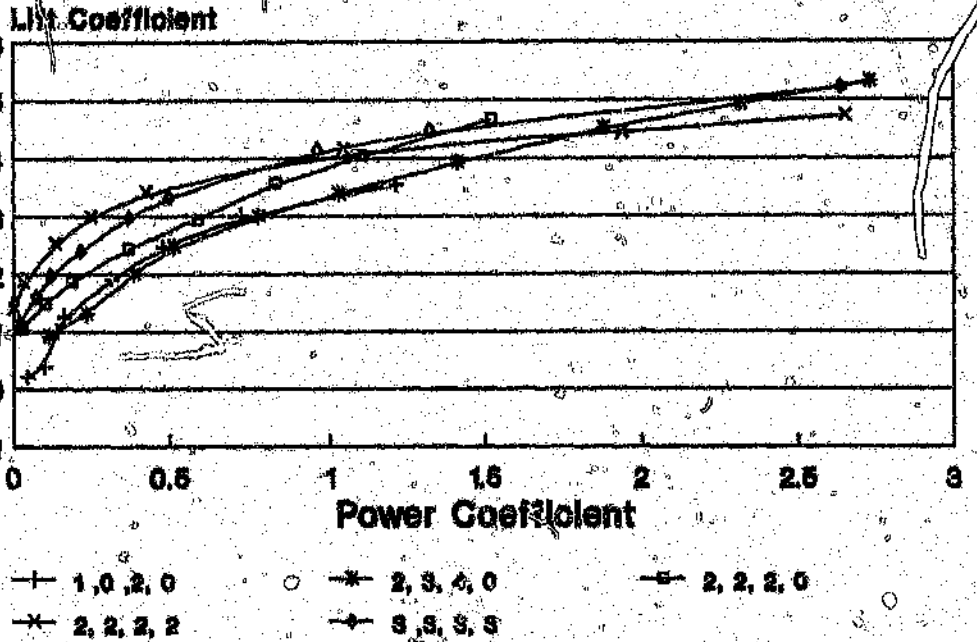

Figure 8.20: C_l vs C_{pow}. Slots at 70°; 105°; 140°; 175°.

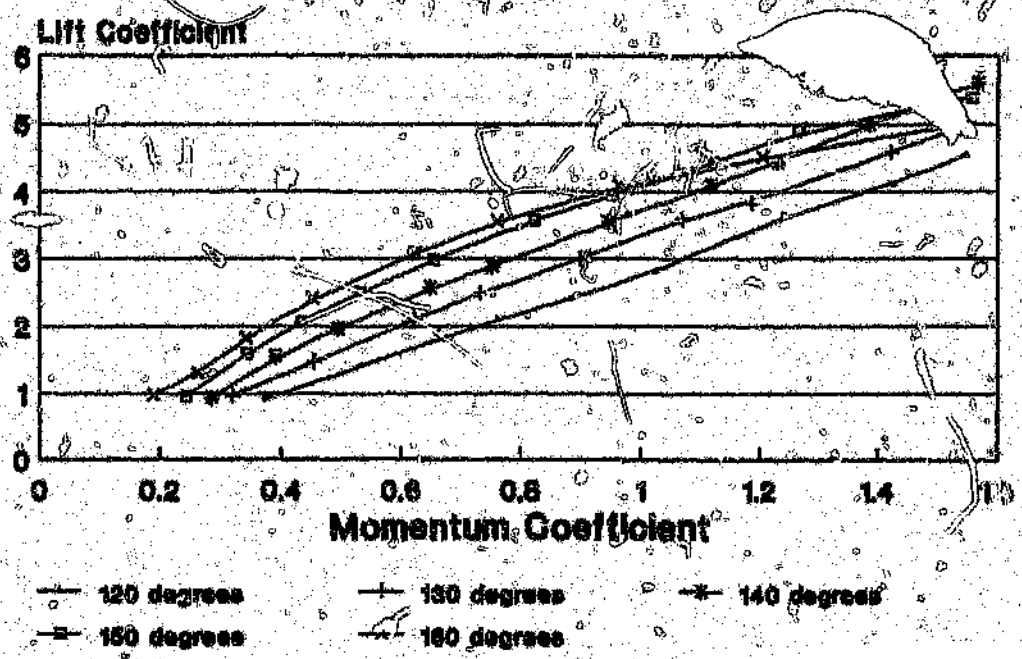

Figura 8.21: C_l vs C_μ. 3 slots. 3, 3, 3, 0.

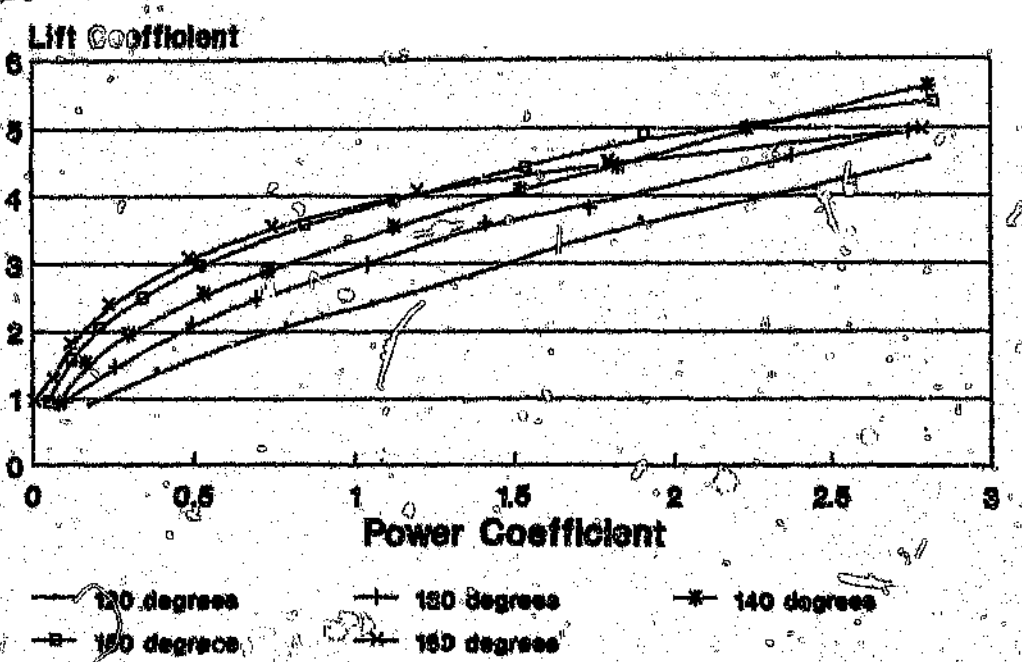

Figura 8.22: C_l vs C_{pow}. 3 slots. 3, 3, 3, 0.

referred to as the upper wall for convenience. Similarly, the flexible wall closest to the cylinder lower surface will be referred to as the lower wall.

The upper wall pressure distribution is shown on the left hand side of the manometer bank, the reading on the extreme left (upper 1) corresponding to the most upstream wall tapping, while the 12th reading from the left (upper 12) corresponds to the most downstream tapping. The lower wall pressure distribution is shown on the right hand side of the manometer bank, the reading on the extreme right (lower 1) corresponding to the most upstream wall tapping, while the 12th reading from the right (lower 12) corresponds to the most downstream tapping. The central tall column in the manometer bank corresponds to the pressure behind the flexible walls. For positive positioning of the walls, it is necessary that this pressure is always lower than the pressures in the tunnel flow channel, ie. the central alcohol column must always be higher than any of the other columns.

Looking at all the measured and predicted wall pressure distributions collectively, it can be seen that the wall pressures are fairly well predicted, especially those on the upper wall, ie. the wall closest to the cylinder. It is also observed that the pressures, upper and lower, upstream of the cylinder correspond better than those downstream. A source flow affects the velocity of the flow both upstream and downstream of the source, upstream velocities being decreased, while downstream velocities increase. Since the static pressure in a flow is proportional to the square of the flow velocity, the difference between downstream pressures and the freestream pressure will be greater downstream than upstream. A change in source strength therefore has more effect on downstream static pressure than upstream pressure. The discrepancy in the measured pressures of the CC cylinder downstream of the cylinder is therefore probably due to the incorrect modelling of the cylinder drag and fluid addition. At present the drag and fluid addition is modelled as a source at the cylinder centre, but a better approximation may be to model the drag as a single, or maybe even distributed, source at the cylinder trailing edge. Durham[17] has shown that the pressure distribution about a CC cylinder can be fairly well approximated if a single source is positioned where the ideal flow would normally leave the cylinder, ie. the downstream stagnation point, in addition to the other three elementary flows, ie. freestream, doublet and vortex. His method does not,

measured wall pressures for a similar sized rigid wall tunnel using the same model would be far worse due to the large blockage of the tunnel caused by the model. Tunnel boundary corrections applied to the data of such a test are not likely to be very successful either, especially as far as boundary layer effects are concerned, a central issue in CC aerofoils.

9.2 Tests on CC Cylinder

9.2.1 Drag of the Cylinder

The drag of the cylinder was measured at various tunnel speeds, to establish the relationship between drag and Reynold's number and compare it with well-documented data. For this test, all four slots were closed and sealed with masking tape. Furthermore, to eliminate any asymmetry of the model, the slots were positioned symmetrically at the rear of the cylinder. The slots (and masking tape) were positioned to be situated in the wake of the cylinder, thereby not tripping the boundary layer and affecting the transition of laminar to turbulent flow.

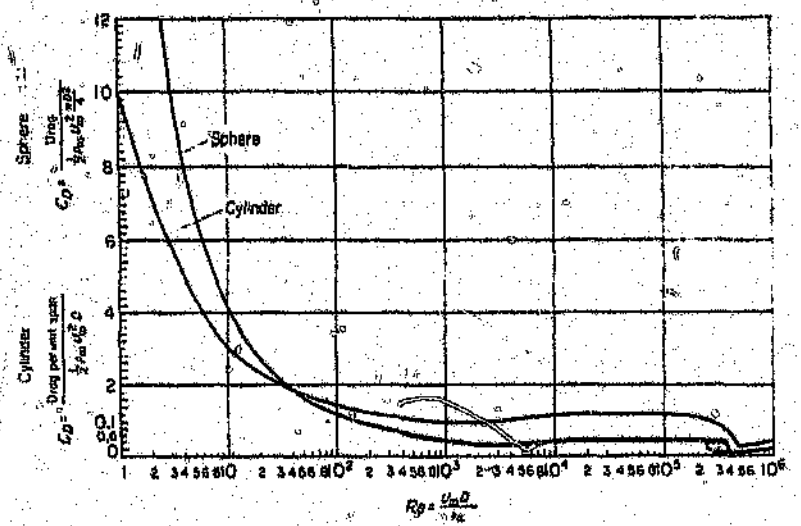

Figure 9.1: Documented variation of C_d with Re_d.

Figure 9.1 shows the accepted variation of drag coefficient with Reynold's number as given by Houghton and Carruthers[24]. The important features of this figure are a drag coefficient of 1.2 before, and approximately 0.5 after, transition. The transition commences at a Reynold's number of 2×10^5, and is complete at a Reynold's number of approximately 4.5×10^5. The freestream

To obtain a single drag curve, readings in the low Reynold's number range would have to be the average of a large number of measurements taken over a period that contains numerous oscillations of the drag reading.

9.2.2 Dimensionless Groups

Figure 8.2 through to Figure 8.6 show the variation of C_l and C_d with C_μ for a cylinder with 4 slots of fixed position, but ranging in thickness between 1mm and 5mm. The figure caption gives the slot positions, as well as their corresponding slot thickness. The tests were done at 25 m/s, 30 m/s and 35 m/s to establish whether the dimensionless groups normalize the data onto a single curve. It is evident from the curves that this is indeed the case.

Figure 8.7 through to Figure 8.12 show the variation of C_l and C_d with C_μ for a cylinder with 3 slots of fixed position, but ranging in thickness between 1mm and 5mm. Again, the slot positions and thicknesses are given in the figure caption. For this slot configuration, the tests for slot sizes ranging from 1mm to 4mm were done at 30 m/s and 35 m/s (Figure 8.7 through to Figure 8.10), while the tests for a slot size of 5mm were done at 15 m/s, 20 m/s, 25 m/s, 30 m/s and 35 m/s (Figure 8.11 and Figure 8.12).

The 3 slot, 5mm slot configuration was tested over a wide range of speeds for two reasons, firstly to establish the behaviour of C_l and C_d over a range of Reynold's number, and secondly to obtain high values of lift for the limited blowing power that was available from the CC blower. Since the blower supplying air to the CC cylinder only has a limited power, high lift coefficients can only be obtained for cylinder configurations with large slots sizes, ie. large slot flow rates, if the tunnel speed is kept low. Small slot sizes generally require lower blowing volumetric flow rates for a given boom pressure, therefore they do not suffer from the blower power limitation to a great extent.

Referring collectively to Figure 8.2 through to Figure 8.12, ie. those tests performed with varying tunnel speed, it can be seen that the data collapses onto one curve for different tunnel speeds for each cylinder configuration. This implies that, at least as far as tunnel speed is concerned, the dimensionless groups used to normalize the data included all the important

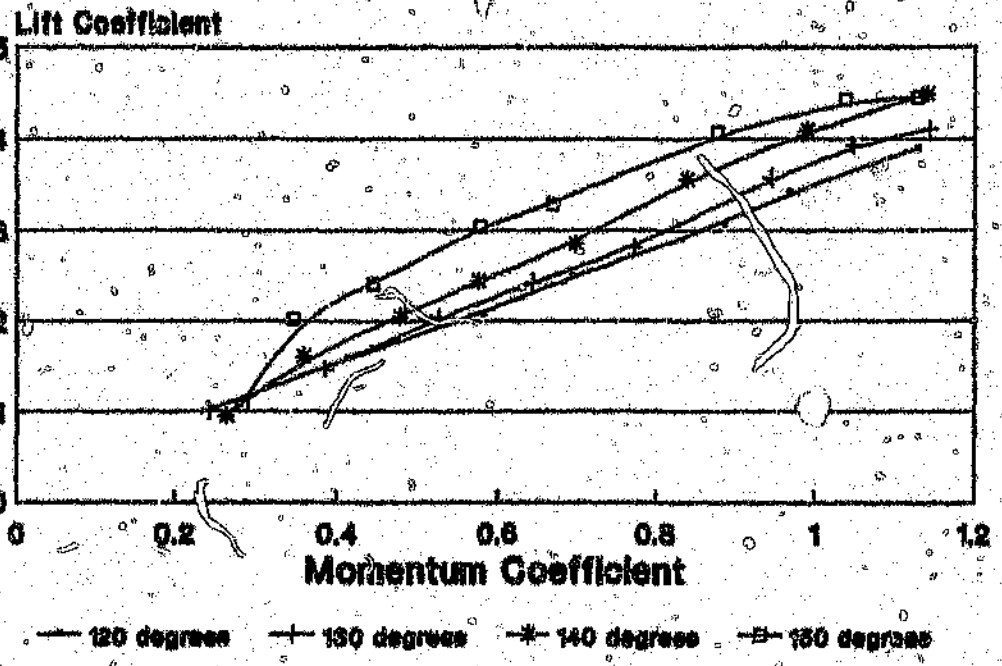

Figure 8.23: C_l vs C_μ. 2 slots. 3, 0, 3, 0.

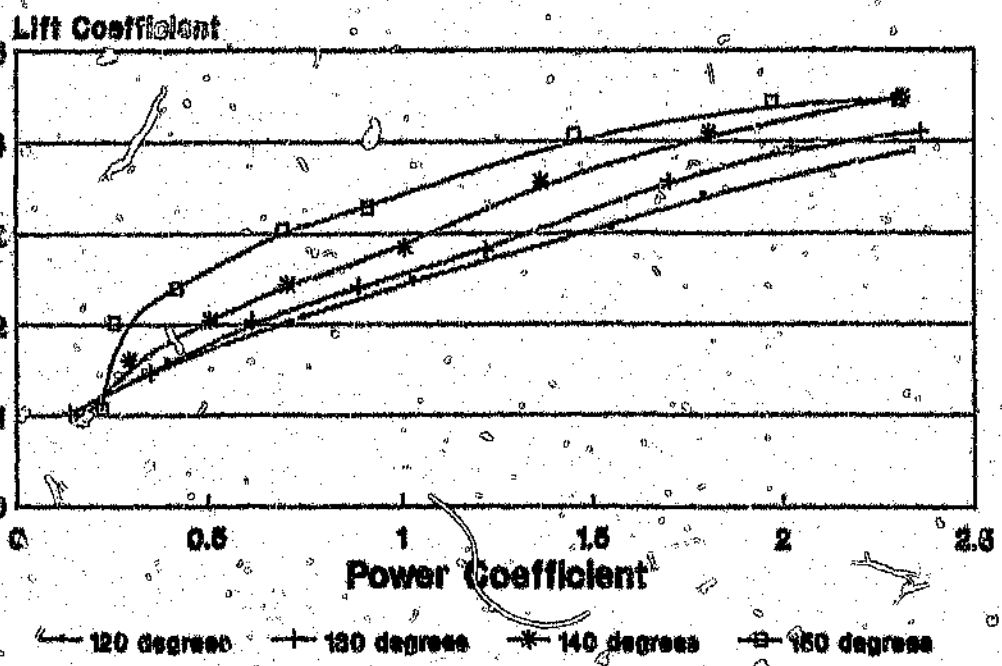

Figure 8.24: C_l vs C_{pow}. 2 slots. 3, 0, 3, 0.

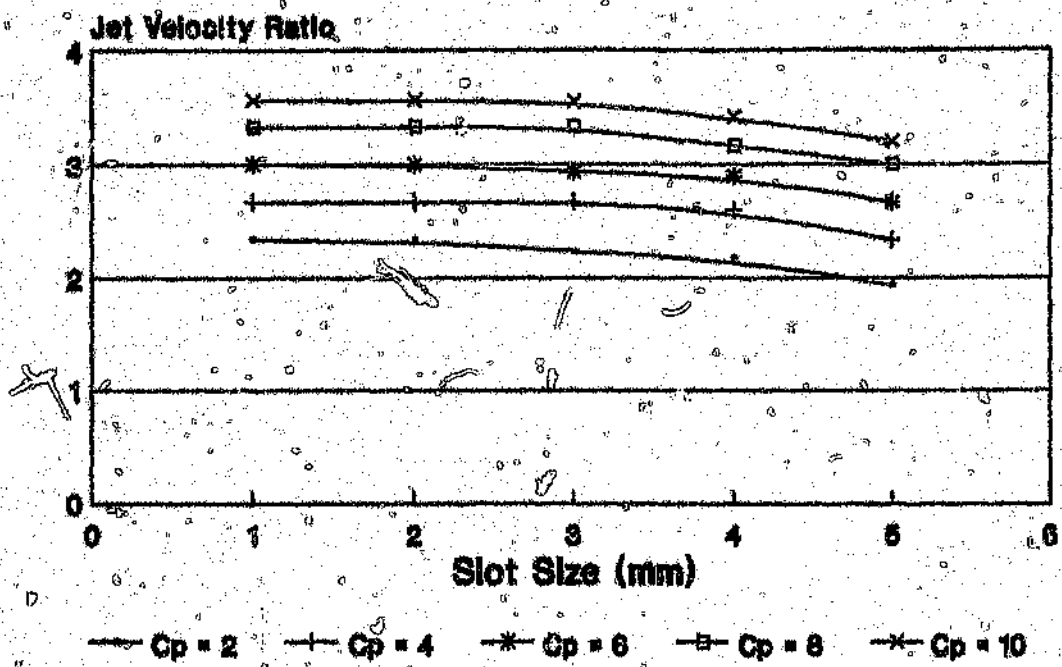

Figure 8.25: V_{jet} vs slot size. 3 slots. 70°; 105°; 140°.

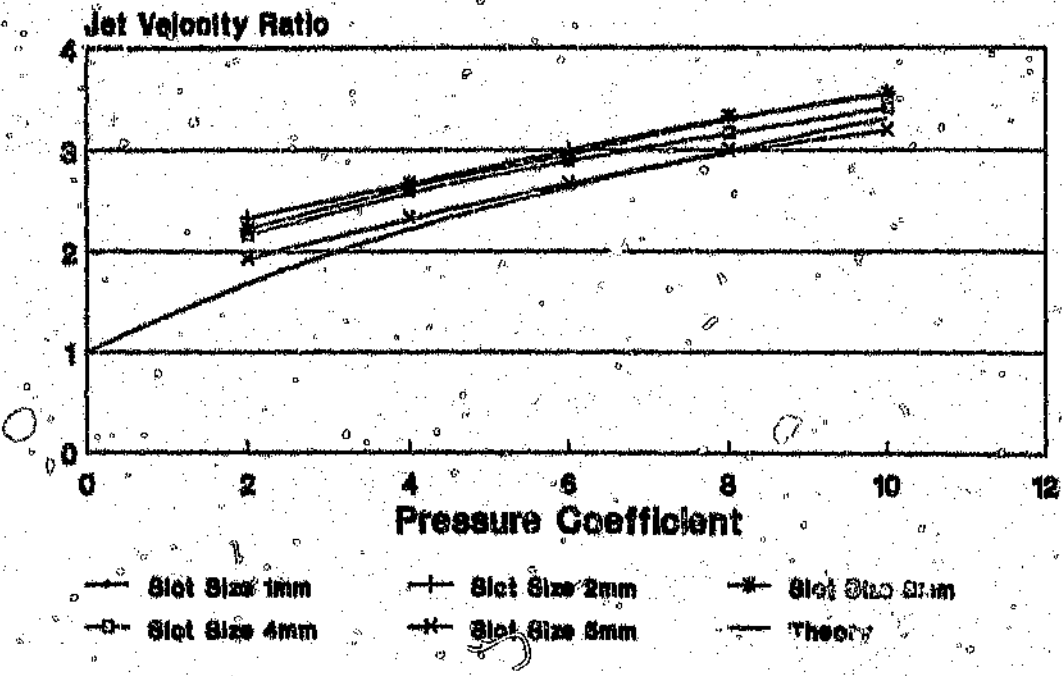

Figure 8.26: V_{jet} vs C_p. 3 slots. 70°; 105°; 140°.

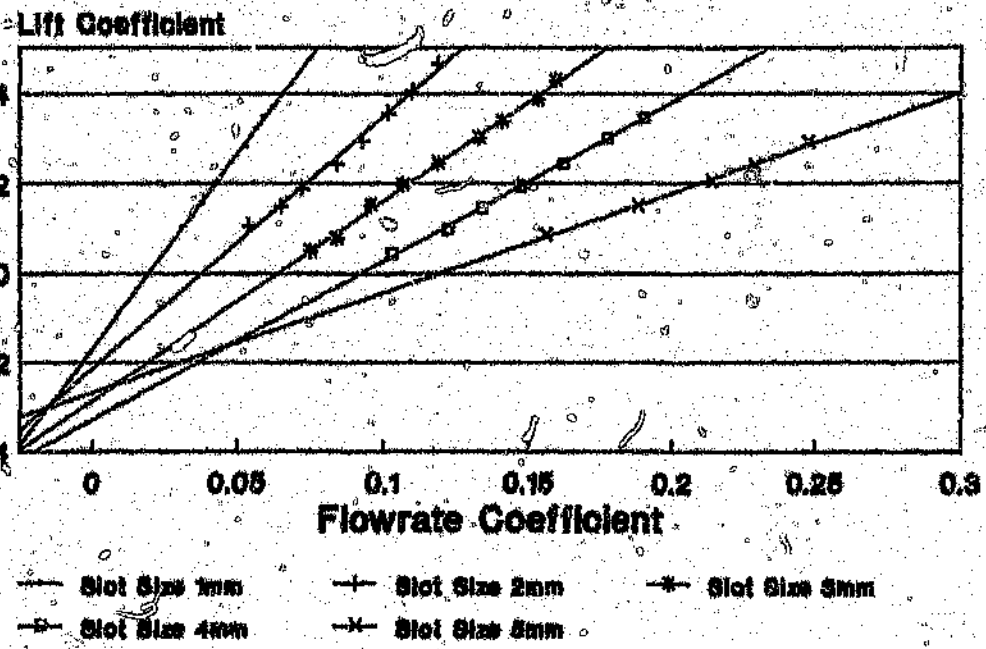

Figure 8.27: C_l vs C_q. 3 slots. 70°; 105°; 140°.

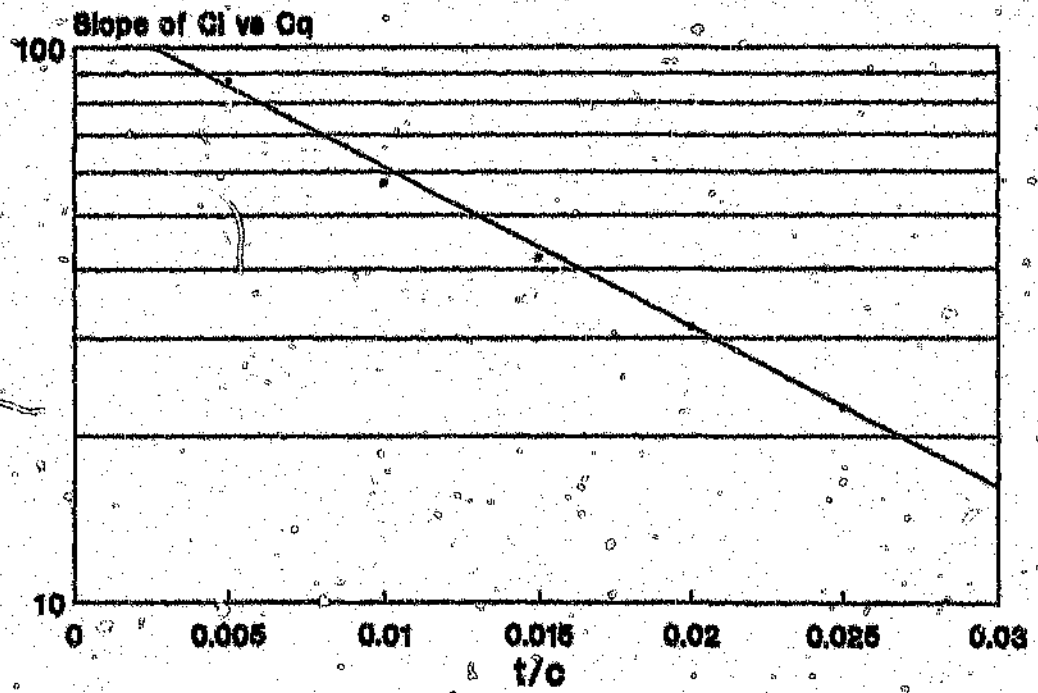

Figure 8.28: Slope of (C_l vs C_q) vs t/c.

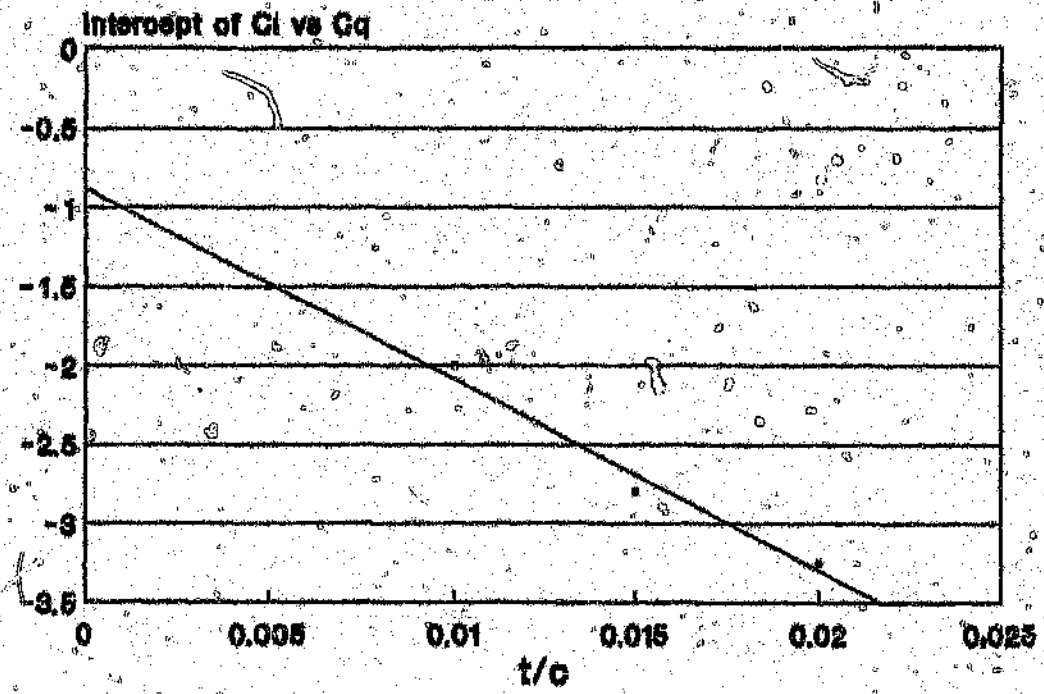

Figure 8.29: Intercept of (C_i vs C_q) vs t/c.

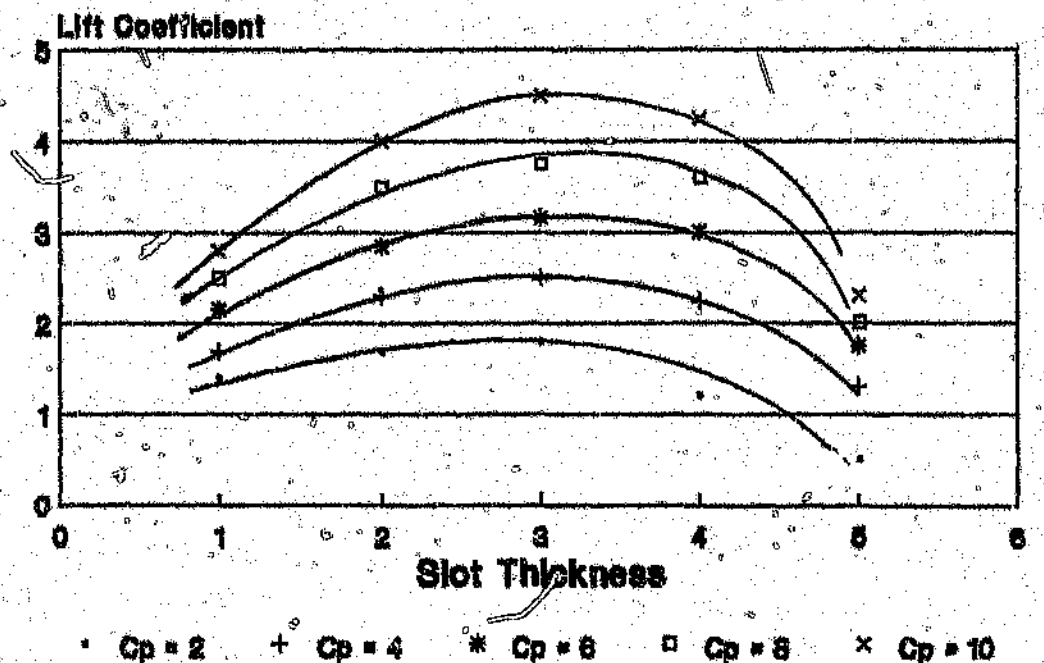

Figure 8.30: C_l vs t. 3 slots. 70°; 105°; 140°.

9 Discussion

9.1 Adaptive Wall Wind Tunnel

9.1.1 Wall Streamlining Strategy

To determine how well the tunnel walls were being streamlined during tests on the CC cylinder, predicted wall pressures were compared to measured wall pressures. A cylinder with a random slot configuration was chosen to provide lift and drag, the geometry of the cylinder slots not being important since the only inputs required by the streamlining strategy are the model lift, drag, total slot flow rate and the tunnel speed.

The predicted wall pressure distribution was calculated using inviscid incompressible potential flow theory. Details of the method used are given in Appendix B. The method predicts velocities at the tunnel walls, which are then converted into pressures using Bernoulli's equation. A computer program, called CALCPRES.EXE (to be found in Appendix F), was used to calculate the wall pressures. The algorithm takes into account the movement of the pressure tappings as the wall curvature changes, ie. as the flexible walls change in arclength. The predicted pressures should therefore correspond to the measured pressures exactly if the wall streamlining strategy is perfect.

The measured wall pressure distribution, obtained from the wall pressure tappings, was displayed using an alcohol manometer, the predicted pressure distribution being superimposed onto the measured one by means of transparent overlays. Both pressure distributions were then photographed simultaneously so that they could be compared at a later stage. The photographs are shown in Plate 8,1 through to Plate 8,9. For completeness, the comparison was done at two tunnel speeds, namely 30 m/s and 40 m/s, for two drag coefficients and for various lift coefficients. The drag coefficient included the effect of fluid addition through the slots, and because the pressure distribution is not very sensitive to changes in drag coefficient, only two cases were plotted, ie. $C_d = 0.5$ and $C_d = 1$. Whichever drag case was closer to the actual drag of the CC cylinder was then used.

Since the test section is lying on its side, the flexible wall closest to the cylinder suction side (upper surface) will be

however, predict the effects of cylinder drag on the pressure distribution, therefore it cannot be applied directly. Sun, Pai and Chopra[20] have shown that the pressure distribution about a CC ellipse due to drag can be approximated by a distributed source in the region of the ideal ellipse downstream stagnation point. It may therefore be possible to model the drag and fluid addition of the CC cylinder using one of the two methods mentioned above.

Referring to Plate 8,1 and Plate 8,6, ie. those tests with the slots completely closed and therefore zero lift, it can be seen that the measured pressures behind the model are lower than predicted, or in other words, the velocities behind the model are too high. Since there was no fluid addition or lift in these two cases, the increased velocities behind the model can be attributed to the effects of drag alone. Any body having drag has a wake which displaces the freestream flow, causing higher velocities behind the model. Since the pressures behind the cylinder are too high, ie. the velocity is too low, it is suspected that the source strength in the wall streamlining strategy and wall pressure prediction is too small, causing too little displacement of the freestream.

It is therefore suggested that the source strength in the potential flow model is increased until the predicted wall pressures match the measured wall pressures. This may seem to be a very empirical means of getting the theory to work, but it must be remembered that a change in theory affects not only the pressure distribution, but also the way in which the walls are streamlined, and hence the actual flow field. Since the flow field near the tunnel walls is the focus of attention, the manner in which the model and its effects are represented in an inviscid flow field is arbitrary. The only requirement is that the calculated and measured flow fields near the tunnel walls match, subject to the condition that the predicted flow field has been calculated using a method that represents an unconfined and inviscid flow field. This condition is based on the reasoning that the flow field near the tunnel walls is indeed inviscid, and is required to be unconfined. An inviscid potential flow model can be used to satisfy both these conditions, irrespective of whether the model uses point or distributed elementary flows.

As far as lift is concerned, ie. flow curvature, the measured and predicted pressure distributions match quite well. It can however be observed that, for higher lift coefficients, the pressures

near the test section inlet, ie. those on the outer edges of the manometer, match less well. In theory, the measured pressures on the upper and lower walls should approach one another at the test section inlet and exit, as indicated by the predicted pressure distributions. In other words, the outermost pressures of the manometer should be almost equal, the same being true for the innermost pressures. From the photographs, especially those corresponding to higher lift coefficients, it is observed that this is not the case. This aberration is due to the finite, in fact very short, length of the flexible test section with respect to its width.

Flow entering the test section parallel to the tunnel axis is forced to change direction rapidly in order to comply with the test section side walls. Since the flow is being deflected towards the upper wall, such a change in flow direction would cause higher pressures on the lower wall, and lower pressures on the upper wall. This trend is observed in the photographs, reinforcing the deduction that the test section is too short. Furthermore, at the test section exit, flow having a angularity towards the lower wall is straightened rapidly by the diffuser which is parallel to the tunnel axis. Since pressure effects are transmitted upstream in an incompressible flow, the effects of a change in direction of the flow at the test section exit are felt both upstream and downstream of the test section exit. The straightening effect of the diffuser side walls, and hence the test section side walls upstream, would cause a lower pressure on the upper wall, and a higher pressure on the lower wall. From the photographs, this is once again apparent, and it can be concluded that the mismatch in test section upper and lower wall pressures at the inlet and exit is due to the rather short length of the flexible test section.

The flow can only be streamlined perfectly if the flexible walls extend very far upstream and downstream. The transonic tunnel used by Goodyer and Wolf[13] has a length to width ratio of 10, whereas the present tunnel only has a ratio of 3.5. The accuracy of the results is obviously a function of the tunnel size, and hence cost. It is felt, however, that the pressure distributions match quite well in the region of the model, and these are the pressures which will affect the aerodynamic forces on the model the most. The fact that the wall pressures, measured and predicted, actually correspond in magnitude and trend, is already an achievement in itself. The correlation between predicted and

turbulence level is zero.

Figure 8.1 shows the variation of measured lift and drag coefficients of the test cylinder with Reynold's number ($Re = 10^5$ corresponds to a tunnel speed of 9 m/s). The lift coefficient is also shown because its magnitude was not necessarily zero during the test, the reason being that the cylinder model was not located in the centre of the test section laterally, but offset from the tunnel centreline by 125mm. The tunnel walls were therefore not symmetrical, and would cause a lift component if not streamlined properly.

From the figure it can be seen that the transition occurred between 10^5 and 3.5×10^5, and that the drag coefficient before and after transition is approximately 1.2 and 0.5 respectively. These drag trends are very close to the accepted values, the only difference being a slightly early transition. This implies that the tunnel turbulence level is not zero, which is very likely since a tuft screen upstream of the test section was still in place during the tests. If the tuft screen were removed, the tunnel turbulence level would probably approach zero. A zero tunnel turbulence level could be expected since the air entering the inlet contraction will have atmospheric turbulence levels which, for an enclosed volume such as the inside of a building, should be close to zero. The tuft screen was never removed since it was felt that a higher effective tunnel Reynold's number would be useful in further tests since a lower tunnel speed could then be employed for a given flow Reynold's number requirement.

The lift coefficient is observed to be about zero for all Reynold's numbers, which implies that the tunnel walls are being streamlined satisfactorily. This observation is all the more remarkable when it is noted that the tunnel blockage due to the cylinder is 20%, and that the difference in the width of the streamtubes on either side of the cylinder is 250mm, ie. 25% of the tunnel width. There is a slight variation of the lift coefficient about zero, this probably being due to the streamlining not being perfect. It can however be deduced that, at least for lift coefficients around zero, the tunnel walls are being streamlined satisfactorily as far as lift is concerned.

The divergence of both the lift and drag curves at low Reynold's number is due to random transducer readings taken in a fluctuating flow field caused by the cylinder shedding vortices.

variables.

The above observation can be expected since the lift, drag and momentum coefficients are well established parameters in aerofoil testing. Nevertheless, it is reassuring to see data collapsing onto a single curve, especially when one considers the complex flow field giving rise to these curves.

Since the air density and cylinder diameter could not be varied deliberately, nothing can be said about the success of the dimensionless parameters with regard to these variables. However, based on the previous success of using these parameters, it can be assumed that variations in air density and model size will also be accounted for by the dimensionless groups.

The small amount of scatter in the data suggests that the flow was steady and that the transducer outputs had little noise.

9.2.3 Effect of Reynold's Number

Referring to Figure 8.2 through to Figure 8.6, it can be seen that the data are relatively insensitive to changes in freestream velocity from 25 m/s to 35 m/s. This is important since it is desirable to test at as a low a tunnel speed as possible, since this implies that the highest lift coefficients can be achieved for a given circulation control blower power.

Figure 8.11 and Figure 8.12 show lift and drag data for a cylinder with 3 slots open 5mm, but for various tunnel speeds. It is evident that for very low tunnel speeds (15 m/s and 20 m/s) there is a definite effect of Reynold's number on drag, while the lift seems to be insensitive to Reynold's number. This is expected since drag is dictated by viscous shear as well as pressure effects, while lift is governed almost exclusively by pressure effects. At a low Reynold's number, viscous effects will become prominent, and hence the drag will be affected more than the lift. For tunnel speeds of 25 m/s and greater, there are virtually no Reynold's number effects on lift or drag. For this reason, the majority of subsequent tests were performed using a tunnel speed of 25 m/s, the intention being to obtain the highest lift coefficients for the available circulation control fan power.

Although the range of speeds used for these tests was quite small

(15 m/s to 35 m/s), it did encompass the laminar to turbulent transition of the non-lifting cylinder (15 m/s to 30 m/s). Since the slot efflux is almost certainly turbulent, it is very unlikely that the laminar to turbulent transition of a lifting CC cylinder will occur at a higher Reynold's number than the non-lifting case. In fact, the transition was observed to occur at lower Reynold's number (corresponding to 25 m/s). It can therefore be deduced that at velocities greater than 25 m/s, the flow Reynold's number has little effect on lift and drag of the CC cylinder.

9.2.4 Comparison of Configurations

A whole series of slot configurations were tested to establish a data base on which the discussion of trends could be discussed. The discussion of trends is only useful, as far as design is concerned, if it leads to some conclusion regarding which configuration is the best for a particular application. For the CCTB concept the requirement is the production of the greatest torque using the smallest amount of absorbed engine power. This translates directly into the creation of the greatest lift using the least power. For this reason it was decided to plot lift coefficient, C_l, against power coefficient, C_{pow}, for all the configurations tested.

Figure 8.13 and Figure 8.15 show the curves of configurations with 3 and 4 equal slots respectively, plotted in the conventional fashion using C_l and C_μ. The sizes, as well as positions, of the slots are given in the figure. Plotting lift data against C_μ suggest that the optimum configuration is the one with the smallest slots, however, if the same lift data are plotted against C_{pow} as shown in Figure 8.14 and Figure 8.16, it is evident that this is not the case. It can be seen from the curves that, for the case with 4 slots, ie. Figure 8.16, the lowest power consumption for a given lift is obtained when the slot size is between 2mm ($C_\mu < 0.7$) and 3mm ($C_\mu > 0.7$), depending on the desired lift. For the case with 3 slots, ie. Figure 8.14, it is clear that the configuration with slots of 1mm is no better than that of 2mm, and only marginally better than the case with 3mm slots.

As far as the CCTB is concerned, the merit of a particular configuration is more a function of the input power than the slot momentum. The reasons for this is that a particular slot momentum

can be achieved using various amounts of input power, depending on the amount of residual kinetic energy present in the jet. Since one of the purposes of the CC is to restore the momentum lost by the cylinder boundary layer due to the effects of surface shear forces (by entraining the boundary layer), it follows that various amounts of power can be absorbed in this process depending on what jet velocity and mass flow rate is employed. In a manner analogous to the high bypass-ratio turbofan, a given momentum transfer can be effected at low power if the transfer involves a large mass flow with a small residual kinetic energy. The better efficiency of the larger slot sizes (around 3mm), especially in the case of the cylinder with 4 slots, is then probably due to this effect.

Figure 8.17 shows the variation of C_l with C_μ for various random configurations with differing slot sizes, but fixed slot positions. The individual digits of the codes in the legend of the plot correspond to the slot sizes (in mm) at 70°, 105°, 140° and 175°. It can be seen that two particular slot configurations, ie. 2,0,1,0 and 1,0,2,0, seem to perform better than any of the others. The former of these corresponds exactly to the slot configuration employed by McDonnell Douglas on their NOTAR demonstrator.[4] Figure 8.18 shows the same lift data plotted against C_{pow}, and reveals an interesting fact. The slot configuration 2,3,4,0 has a better performance over a greater lift range than 2,0,1,0 or 1,0,2,0. A CCTB helicopter employing the 2,3,4,0 slot configuration would require a smaller boom diameter or less power to obtain the same boom torque. From a design and operation point of view this is significant.

In an effort to establish which configuration had the best performance, all configurations that had been tested were compared. Figure 8.19 and Figure 8.20 show comparative plots of several successful configurations plotted against C_μ and C_{pow} respectively. The figures only include configurations that performed well in previous comparisons. Using only momentum to judge the merit of a configuration, configuration 1,0,2,0 would seem to be best, especially up to lift coefficients of about 4. Considering power, however, it can be seen that configurations 2,2,2,2 and 3,3,3,3 perform best up to lift coefficients of about 4.5. For lift coefficients around 3 or 4, configuration 3,3,3,3 would be the best since it has greater maximum lift. At lift coefficients of 3 or 4, ie. those that would be interesting for CCTB's due to the relatively low power requirement for a given

lift, it can be seen that the difference in power absorbed between configurations 1,0,2,0 and 3,3,3,3 is not small, the former being more than twice the latter.

Since the designer of a CCTB is more concerned about the power input required for a given lift by a particular configuration, and not so much about the (rather academic) momentum of the slot efflux, it can be concluded that the power coefficient is a more suitable parameter to judge the merit of CCTB aerofoil sections than the momentum coefficient.

9.2.5 Effect of Number of Slots

Referring to Figure 8.17 and Figure 8.19, ie. plotting lift data against slot momentum, it can be inferred that, for a given slot momentum, maximum lift is obtained using a cylinder with fewer slots. Although no configurations were tested with only one slot, it has been suggested by Lockwood[19] that, for small slot momentum coefficients, a single slot has the best performance. This is hardly a surprising observation since Lockwood used the momentum coefficient as a figure of merit when comparing different cylinder configurations. The observation is based on the fact that, for a given slot momentum, small slots have more kinetic energy. Small slots therefore have greater potential to keep a tired boundary layer moving, but this potential is not being considered if momentum is used as a yardstick. At some stage the price for this added energy has to be paid, therefore a better figure of merit would be one that considers the kinetic energy of the jet, the power coefficient doing precisely that.

Referring to Figure 8.18 and Figure 8.20, ie. plotting lift data against boom power, it is noticed that the larger the number of slots, the better the performance of the cylinder. This implies that, as far as power requirements are concerned, it is better to have distributed momentum addition than a single point of momentum addition. The reason for this is the result of two factors. Firstly, addition of momentum at a single slot favours a small slot size and high slot velocity, which implies a high residual kinetic energy in the jet, energy which is ultimately dissipated in the wake of the cylinder. Secondly, a higher jet velocity will also generate higher shear forces as it passes over the cylinder, therefore the added momentum will be depleted more rapidly as it is still passing over the cylinder. It can therefore be concluded that a larger number of slots is conducive

to lower power input, provided the slots are not situated in separated flow regions or on the lower surface of the cylinder. The ultimate solution would be to have uniformly distributed momentum addition since this would approach the situation where momentum is added at the same rate and location where it is being depleted. Such a surface effectively would not have surface shear from the point of view of the inviscid flow field, and once a circulatory flow had been established, it would continue indefinitely provided the CC is maintained.

9.2.6 Effect of Slot Thickness

As discussed in Section 9.2.5, a small slot thickness may give rise to very high lift coefficients for a given momentum coefficient, but this is not necessarily indicative of the efficiency of the configuration. Lifting efficiency is defined in terms of the ability of a configuration to produce the highest lift for a given blowing power, and not the maximum lift that can be attained by the configuration. The analogy of lifting efficiency in conventional aerofoil testing is the lift curve slope. Referring to Figure 8.14 and Figure 8.16, ie. cylinders with 3 and 4 equal slots respectively, it can be seen that maximum lifting efficiency is obtained for a slot size of 2mm and 3mm for the 3 and 4 slot configurations respectively. Increasing the slot size any further results in a jet that has too little kinetic energy, ie. its velocity is too low, to energize the boundary layer. Even though the flow rate is great, and hence the jet momentum, such a slot is of no benefit. This latter argument is yet another nail in the coffin of a momentum based comparison of different configurations. It will be shown in Section 9.2.8 that increasing fluid addition too much, ie. using very large slot flow rates, decreases the lift that can theoretically be attained by the cylinder.

The slot thickness not only affects the efficiency of lift production, but also the maximum lift that can be achieved by a particular configuration. Figure 8.15 shows how a cylinder with 4 equal slots achieves higher maximum lift coefficients when the slot size is increased. This trend can obviously not be extended to any slot size, and the figure seems to indicate that the curve corresponding to a slot size of 5mm will not obtain as high a maximum lift coefficient as that corresponding to a slot size of 4mm. The truncated nature of the data makes this difficult to prove conclusively.

At this stage no conclusion will be drawn, but it will be shown in Section 9.2.8 that the efficiency of lift production is maximized for a given slot thickness.

9.2.7 Effect of Slot Location

A series of tests were performed to determine the effect of the trailing slot position, since, according to Lockwood[19], this is a major factor influencing the maximum lift which can be attained by a CC cylinder. Maximum lift is defined as the greatest lift that can be attained, no matter what the blowing momentum is. Figure 8.21 shows the effect rotating the cylinder has on lift, for a cylinder with 3 slots open 3mm. The three slots are spaced 35° apart from each other, the trailing slot position being given in the figure. It can be seen that, for a given momentum coefficient, the lift is greater when the slots are located further back. However, this does not necessarily guarantee that the maximum attainable lift coefficient is the greatest. Extrapolating the data of the curves to greater values of slot momentum, it seems that highest overall lift is obtained when the trailing slot is positioned at 140°.

Figure 8.23 refers to a cylinder with only two slots open 3mm. The slots are spaced 140° apart, the trailing slot position being given in the figure. From the figure it can again be seen that, for a given median momentum coefficient, the lift is greater when the slots are positioned further back. Although the tests did not include trailing slot positions beyond 150°, the data seems to suggest that positions beyond 140° do not yield the highest maximum lift. This is probably due to the fact that the trailing edge slot is approaching the rear separation point on the cylinder, and the effect of the added momentum is not felt over much of the cylinder surface.

Figure 8.22 and Figure 8.24 show that the same trends apply when the identical lift data are plotted against power. It can therefore be concluded that, at least for the two configurations mentioned, maximum lift is attained when the trailing slot position is around 140°. Due to insufficient data on other configurations with respect to trailing edge position, no generalizations will be made. The only generalization that can be made is that the further back a slot is positioned, the more likely it is that its effect will be diminished by the wake of the cylinder. Positioning the slot too far forward could lead to

premature flow separation as a result of the boundary layer having insufficient momentum to overcome the adverse pressure gradient on the rear portions of the suction surface of the cylinder.

9.3.8 Analysis of a Single Configuration

Due to the large number of variations that are possible when slot sizes and positions are altered, it was decided to look at one particular slot configuration in detail. This was done to obtain greater insight into the mechanisms of lift production by CC, and to get a better understanding of the flow field in general. The configuration chosen was one with 3 slots, positioned at 70°, 105° and 140°. For each particular test, all three slots had the same slot size, a total of five slot sizes being tested. This particular configuration was chosen because it performed well, and there was a comprehensive set of data (test number 0016 to 0025) to base the analysis on. All further discussion will deal with this particular configuration.

Referring to Figure 8.25, it can be seen that, at least for slot sizes of 3mm and less, V_{jet}/U is independent (or a very weak function) of slot size, and is only a function of the pressure inside the boom, which is given in the form of a pressure coefficient, C_p, for convenience. The independence of jet velocity and slot size is expected, since the ideal velocity of any fluid ejected from a nozzle is only a function of the pressure difference and the fluid density, given by Bernoulli as

$$V_{jet}=\sqrt{\frac{2\Delta p}{\rho}} \qquad (9,1)$$

Figure 8.26 shows the actual variation of jet velocity with boom pressure for various slot thicknesses. The jet velocity was calculated using the slot flow rate and the slot thickness. It is observed that the curves for slot sizes of 3mm or less lie almost on top of one another, and have a small (square-root) curvature. The boom pressure coefficient is defined as

$$C_p=\frac{(p_{boom}-p_{total})}{p_{dynamic}} \qquad (9,2)$$

where p_{total} and $p_{dynamic}$ refer to the absolute freestream total and dynamic pressures, and p_{boom} refers to the absolute pressure inside the boom. Since the freestream total pressure is the sum of static and dynamic pressure, as a first approximation, C_p can be written in terms of the pressure difference across the jet, ie. $p_{boom} - p_{stat}$, where p_{stat} is the freestream static prassure.

$$C_p = \left(\frac{\Delta p}{\frac{1}{2}\rho U^2}\right) - 1 \qquad (9,3)$$

Combining equations 9.1 and 9.3 yields

$$\frac{V_{jet}}{U} = \sqrt{C_p + 1} \qquad (9,4)$$

This curve was plotted as the theoretical prediction in Figure 8.26. From the figure it is evident that the actual jet velocities exceed the theoretical prediction. This is due to the existence of circulation about the cylinder which causes the static pressure on the upper surface to be considerably lower than the freestream static pressure. Since the slots are positioned on the suction side of the cylinder, the static pressure difference across the slot will be greater than predicted. At very large pressure coefficients, the theoretical curve approaches the actual curves since the difference between freestream static pressure and cylinder upper surface static pressure is completely overshadowed by the magnitude of the boom static pressure.

Figure 8.27 shows the variation of lift coefficient with slot flow rate coefficient for various slot thicknesses. The flow rate coefficient was obtained by dimensional analysis in Chapter 5, and is defined as

$$C_q = \frac{Q_{slots}}{SU} \qquad (9,5)$$

The linear nature of the data in Figure 8.27 is interesting, and warrants further investigation. It can be shown that the flow rate coefficient can be written in terms of jet velocity and slot thickness as

$$C_q = \left(\frac{V_{jet}}{U}\right)\left(\frac{t}{c}\right) \qquad (9,6)$$

Now, since C_l is directly proportional to C_q, and because V_{jet}/U is independent of t/c, C_l is directly proportional to V_{jet}/U and t/c.

Looking then at the effect of V_{jet}/U and t/c on lift, it can be shown that the circulation about a lifting cylinder can be written as

$$k = UC_l a \qquad (9,7)$$

where a is the cylinder radius = c/2.
Since C_l is proportional to V_{jet}/U, a simple substitution reveals that k is proportional to V_{jet} and t.

The above is an interesting observation, albeit rather intuitive. Since the only agent promoting a circulatory flow about the cylinder is the tangential ejection of fluid from surface slots, the magnitude of that circulation will almost certainly be a direct function of the velocity of ejection and the quantity of fluid being ejected.

The ejection of fluid on the upper surface of a CC cylinder serves two purposes. If there is no circulation about the cylinder, the ejected fluid will cause a difference in velocity between the upper and lower surfaces of the cylinder, thereby creating a circulatory flow. Unlike the case of an inviscid fluid, once the circulation has been established it must be maintained, since frictional effects in the fluid will tend to dissipate the circulation. If a closed, imaginary boundary is drawn around the cylinder, just outside its boundary layer, the function of the ejected fluid is to overcome the effects of viscosity within that boundary. Since the flow outside the boundary is essentially inviscid, the circulation about the lifting cylinder is not dissipated in this region, ie. the flow field outside the circular boundary of the cylinder will maintain itself indefinitely provided it is not dissipated by the effect of the internal viscous region.

The dissipation of circulation within the boundary is due to distributed frictional shear stress on the surface of the

cylinder, resulting in a depletion of momentum in the boundary layer of the cylinder. To overcome the dissipation of circulation, momentum is added to the boundary layer by means of tangential blowing through surface slots. Since these slots are discreet, they would have to add sufficient momentum to the surface flow not only to recover the momentum already lost, but also to energize the boundary layer sufficiently to reach the next slot (if there are more than 1 slots), or to encounter further adverse pressure gradients.

If the assumption is made that jet and freestream densities are similar, which is reasonable for the low velocities encountered, the momentum coefficient of the jet can be written as follows

$$C_\mu = 2\left(\frac{t}{c}\right)\left(\frac{V_{jet}}{U}\right)^2 \qquad (9.8)$$

It is evident that the momentum added to the boundary layer is also only a function of the two independent parameters, V_{jet}/U and t/c. Since momentum is transferred from the jet to the boundary layer by entrainment of the boundary layer by the jet, it is the momentum of the jet that is the important factor in maintaining the circulation about the cylinder.

Since V_{jet}/U and t/c are inherently linked to the jet momentum (equation 9.8) as well as the circulation about, and hence lift of, the cylinder (equation 9.7), the relationship between slot momentum and lift becomes evident. However, as elucidated earlier, momentum addition is accompanied by residual kinetic energy in the jet, therefore the manner in which momentum is added (number of slots, slot position and slot size) greatly affects the efficiency with which lift is generated.

Referring to Figure 8.27, the lift coefficient can be written as

$$C_l = m\left(\frac{t}{c}\right)\left(\frac{V_{jet}}{U}\right) + n \qquad (9.9)$$

where m and n are the slope and intercepts of the curves, and are both a function of t/c.

Figure 8.28 shows the relationship between m and t/c. The relationship can be written as

$$m=\exp\left(4.669-62.2\left(\frac{t}{c}\right)\right) \qquad (9,10)$$

Figure 8.29 shows the relationship between n and t/c. The relationship can be written as

$$n=-116.7\left(\frac{t}{c}\right)-0.9167 \qquad (9,11)$$

Using Figure 8.26, the jet velocity ratio can be written in terms of the boom pressure coefficient as

$$\frac{V_{jet}}{U}=2+0.1667C_p \qquad (9,12)$$

Combining equations 9.9, 9.10, 9.11 and 9.12, the lift coefficient can be written as

$$C_l=\exp\left(4.669-62.2\left(\frac{t}{c}\right)\right)\left[\left(\left(\frac{t}{c}\right)(0.1667C_p+2)\right]-\left(116.7\left(\frac{t}{c}\right)+0.9167\right)\right. \qquad (9,13)$$

If t/c and C_p are specified for this particular configuration, the lift coefficient can be calculated. The above equation can be differentiated with respect to t/c, to obtain the value of t/c that yields maximum lift. To make the equation more graphic, Figure 8.30 shows the variation of C_l with t for various C_p. It can be seen that for all C_p, and hence jet velocity, C_l is a maximum when t is about 3mm. This maximum is the direct result of the nature of the momentum addition. The addition of momentum is beneficial to the circulation about, and hence the lift generated by, the cylinder. However, the addition of momentum is unfortunately accompanied by the addition of fluid to the freestream by the inherent nature of CC by blowing. In the right hand plot of Figure 5.1, Dunham[17] shows how a high source strength corresponds to a low lift coefficient. In the potential flow model, if an additional source is added to the trailing stagnation point of the lifting cylinder, the upper surface pressures are increased, ie. the suction is reduced. For this reason, addition of fluid to a real cylinder (also in the region

of the trailing edge) will result in a reduced lift. The objective is therefore to add momentum without adding too much fluid. This is again a compromise since the above implies a high jet velocity, which is undesirable from a power input point of view.

Returning to equation 9.13, some interesting deductions can be made about the design of CCTB's. The lift coefficient dictates the geometry of the generic flow about the cylinder, ie. the positions of stagnation points as well as streamline curvature, and since C_p contains only two variables, namely U and p_{boom}, the flow geometry is only a function of U, p_{boom} and t. In the case of a CCTB, if the slot size is kept constant along the length of the tail boom to maximize lift as suggested by Figure 8.30, C_l will vary with the inverse of the rotor downwash since the pressure inside the boom is assumed to be constant. This variation of C_l will be observed as a change in the location of the separation point at various stations along the boom length. The variation of C_l along the span may be undesirable, and since it is no longer desirable to vary slot size along the length of the boom, the only other way to vary the distribution of C_l along the boom is to change the boom diameter along the boom. Since the boom is merely a wing of finite span, it would be desirable to obtain a lift distribution that approaches an ideal case. This ideal case would obviously not be the same as the classic elliptic loading since the freestream velocity, or rotor downwash, varies across the span. Also, induced drag is of secondary importance when compared to absorbed boom power, since the generation of torque about the main rotor axis is of paramount importance. However, some distribution can be found that will maximize torque and minimize power input. The analysis of the above would best be achieved numerically using a computer. The variables in the algorithm would be boom diameter and length, longitudinal slot length and slot thickness, as well as boom pressure. Calculating the input power for various configurations of the above would yield information about the efficiency of the entire CCTB for a given main rotor downwash and torque requirement.

10 Conclusions

The conclusions can be broadly divided into those pertaining to the adaptive wall wind tunnel, and to the tests performed on the CC cylinder.

10.1 Adaptive Wall Wind Tunnel

1 A flexible wall adaptive wind tunnel, capable of high-lift testing with minimal boundary interference, was designed and commissioned.

2 The potential flow wall streamlining strategy works satisfactorily for lift effects, but less so for drag effects.

10.2 Tests on CC Cylinder

1 The quality of data obtained was good, although the uncertainty in the measurements was large.

2 The momentum, power, flow rate and boom pressure coefficients were shown to be relevant parameters in CC testing.

3 The power coefficient can be used to compare the merits of different CC configurations. A cylinder with 4 equal 3mm slots positioned at 70°, 105°, 140° and 175° was found to be the most efficient configuration tested.

4 From a power point of view, the more slots the better, subject to the condition that none of the slots are situated in a separated flow region.

5 The trailing slot position influences the maximum lift attained by the cylinder. A trailing slot position of about 140° was found to be optimum.

6 For any given cylinder configuration, there is an ideal slot size which maximizes the lift.

11 Recommendations

11.1 Wind Tunnel

The following improvements to the wind tunnel are recommended:

1 Remove any surface discontinuities from the inlet contraction, especially in the region of the lower lip.

2 If this does not solve the tunnel speed instability, a new lip may need to be fashioned out of expanded polystyrene.

3 If the speed instability persists, turbulators can be installed at the diffuser inlet.

4 A ladder must be built to ease access to the test section window, which is situated above the test section.

5 The tunnel drive fan speed control should be linked to the PC so that the tunnel speed can be controlled automatically. The hardware is all there, it merely requires wiring up.

6 The CC blower must either be speed controlled or otherwise suitably throttled by a more precise mechanical valve than a simple butterfly flap. It is suggested that the throttle can be controlled (electrically or mechanically) from inside the control room. This will allow the operator to stay in the control room during a complete test, leaving the room only to make adjustments to the model.

7 Smaller load cells can be installed in the balance to increase the accuracy of the balance when small forces are being measured. It is suggested that the new load cells are made to fit the same bolt holes used by the existing load cells. This will allow load cells to be exchanged as the task at hand requires.

8 The tunnel drive fan speed control should have an override which prevents it from being switched on before the wall suction blower is switched on.

9 A 24 channel pressure multiplexer should be obtained to measure the wall pressures rapidly. This will allow different wall streamlining strategies to be employed.

10 Stiffer flexible walls and smoother triangular foam sealing strips may be required to reduce the scatter in the wall pressures.

11 The perspex test section window should be replaced with a glass window if LDV measurements are required.

12 The wall suction fan exhaust should be ducted back into the diffuser inlet by means of rearward facing jets. This will

ensure a constant pressure difference across the walls for all tunnel speeds. The flow entering the diffuser must be equally distributed around the edge of the diffuser in order to prevent disturbance to the upstream flow. The use of rearward facing jets is advised to prevent the possibility of flow separation.

13 A second diffuser should be added behind the tunnel drive fans to reduce the speed of the air being exhausted. This will increase the tunnel speed for a given power requirement and also reduce the tunnel noise level. Two simple conical sections, one behind each fan, would be adequate.

14 The CC blower should be enclosed in a sound absorbent box to reduce the high noise level emitted by this particular component.

11.2 Software

The following alterations to software are recommended:

1 It is strongly suggested that some form of verification software is written. At present the tunnel can damage itself if certain relays controlling the actuator motors become defective. Since the wall positioning system is a closed loop system with feedback, a simple checking procedure, that checks the tunnel at initialization, could be written. This procedure would instruct the walls to move to a position and then check that the actuators are performing satisfactorily.

2 The operating program, MAINPROG.EXE, should use measured values of U, C_l, C_d and Q_{slot} to streamline the walls. This will decrease the user's workload, and increase the rate of wall streamlining.

3 The user inputs to the operating software should be error checked so that the program does not crash if incorrect data is entered.

4 A routine should be written that plots the data as it is being acquired.

5 At present the tunnel takes about 15 seconds to streamline the walls for small changes in C_l, typically in the region of 0.5. The walls are positioned rapidly (using a 12V power supply) to their approximate positions, and then slowly (using a 6V power supply) to their final positions. If the walls could be positioned rapidly (using a 20V power supply for instance) to their final positions, the streamlining

time could be reduced to a second or two. The hunting problem caused by rapidly moving walls and small error bands could be alleviated by having a separate error band for each actuator which takes into account the stopping distance of the actuator. At present the wall position sampling is slow, but clever alterations to the software can increase the sampling rate substantially. The above modifications would allow data to be acquired (and plotted) in real time as the tunnel is adjusting itself to the changing flow field.

11.3 Streamlining Algorithm

The following alterations to the streamlining strategy are recommended:

1 It is suggested that the streamlining algorithm be modified to better simulate the effects of drag, ie. by moving the position of the source in the potential flow model to the rear stagnation point of the cylinder, or by using a distributed source.

2 The algorithm should include a Zhukovsky transform that will allow non-circular aerofoils to be modelled approximately.

3 A panel method applied to the walls can be used to calculate wall pressures, and hence to streamline the walls. The effects of a finite test section length would have to be included. This method of streamlining the walls requires no knowledge of the model being tested. The scatter of the wall pressure readings (probably caused by wall waviness) could pose some problems.

11.4 Further Tests

The following additional tests could be performed.

1 The effects of slot location, especially with respect to the cylinder 'angle of attack', should be investigated in greater depth.

2 More tests should be performed with one and two slots open, to prove conclusively that a large number of slots consume the least power for a given lift.

12 References and Bibliography

12.1 References

1 Logan A H; **Experimental Investigation of a Circulation Control Tailboom under a Statically Thrusting OH-6A Main Rotor.**
Hughes Helicopter Report No. HH 78-29. Feb 1976.

2 Logan A H; **Evaluation of a Circulation Control Tailboom for Yaw Control.**
USARTL TR-78-10, Applied Technology Lab, US Army.

3 Rao C S; **Tailboom Design of the 520N NOTAR Helicopter.**
McDonnell Douglas Helicopter Company, Mesa Arizona.

4 Nurick A, Fonternel M A; **The Use of Circulation Control on the Tail Boom of a Helicopter: A Survey.**
Research Report No 93, Sept 1990 School of Mechanical Engineering, University of the Witwatersrand.
ISBN 1-86814-187-X

5 Groesbeek C, Nurick A; **Modelling of a Helicopter Circulation Control Tail Boom using a 3-D Navier-Stokes Code.**
Research Report, 3rd South African Aeronautical Engineering Conference Aug 1991

6 Rae W H, Pope A; **Low-Speed Wind Tunnel Testing.**
John Wiley and Sons Inc. 1984. 2nd ed.

7 Wolf S W D; **Status of Adaptive Wall Technology for Minimization of Wind Tunnel Interferences.**
ICAS Congress, ICAS-90-6.2.1, Sept 1990.

8 Tuttle M H, Mineck R E; **Adaptive Wall Wind Tunnels: A Selected Annotated Bibliography.**
NASA Technical Memorandum 87639, 1986.

9 Lewis M C; **Aerofoil Testing in a Self-Streamlining Flexible Walled Wind Tunnel.**
Ph.D Thesis. NASA CR-3128, May 1988, N88-22865.

10 Sears W R; Self Correcting Wind Tunnels.
Aeronautical Journal Feb/Mar 1974.

11 Ferri A, Baronti P; A Method for Transonic Wind Tunnel Corrections.
AAIA Journal, Vol.11, No.1, Jan 1973.

12 Goodyer, M J and Wolf, S W D; Self-Streamlining Wind Tunnel: Low Speed Testing and Transonic Test Section Design.
NASA Cr-145217, Oct 1977.

13 Goodyer M J, Wolf S W D; Development of a Self-Streamlining Flexible Walled Transonic Test Section.
AAIA Journal Vol.20 No.2 Feb 1982.

14 Wolf, S W D; The Design and Operational Development of Self-Streamlining Two-Dimensional Flexible Walled Test Sections.
Ph.D. Thesis. NASA CR-172328, 1984. N84-22534#.9

15 Judd M; Analytical Work in Support of the Design and Operation of Two-Dimensional Self-Streamlining Test Sections.
NASA CR-145019, July 1976.

16 Young T; Outlines of experiments and Inquiries Respecting Sound and Light.
Lecture to Royal society, 16 Jan 1800.

17 Dunham J; A theory of Circulation Control by Slot-blowing Applied to a Circular Cylinder.
Journal of Fluid Mechanics Vol.33 No.3 pp 495-514, 1968.

18 Jones, Buckingham; 1964.

19 Lockwood V E; Lift Generation on a Circular Cylinder by Tangential Blowing from Surface Slots.
NASA Technical Note D-244.

20 Sun M, Pai S I, Chopra I; Aerodynamic Force Calculations of an Elliptic Circulation Control Airfoil.
Journal of Aircraft Vol.23 No.9 Sept 1986.

21 Karamcheti K; **Principles of Ideal-Fluid Aerodynamics.**
John Wiley and Sons. 1956.

22 Douglas J F, Gasiorek J M, Swaffield J A; **Fluid Mechanics.**
Pitman Publishing Ltd, 1979.

23 Hoerner S F; **Fluid-Dynamic Drag.**
S F Hoerner c/o AIAA. 1957.

24 Houghton E L, Carruthers N B; **Aerodynamics for Engineering Students.**
Edward Arnold, 3rd ed, 1982. ISBN 0-7131-3433-X.

25 British Standard 1042: Part1: 1964; **Methods for the Measurement of Fluid Flow in Pipes.**
Orifice Plates, Nozzles and Venturi Tubes.
Gr9 British Standards Institution.

26 Shigley J E; **Mechanical Engineering Design.**
1st Metric edition. Mc Graw - Hill Inc. 1986.

27 Beitz W, Kuttner K H; **Dubbel: Taschenbuch fur den Maschinenbau.**
16 Auflage. Springer Verlag, Berlin 1987.

12.2 Bibliography

1 Milne-Thomson; **Theoretical Aerodynamics.**
4th edition. Macmillan and Company Limited. 1966.

2 Nurick A, Laing P, Groesbeek C; **An Investigation of the Application of Circulation Control to the Tail Boom of a Helicopter.**
Research Report, 3rd South African Aeronautical Engineering Conference, Aug 1991.

3 Pai Shih-I; **Viscous Flow Theory - Turbulent Flow.**
D Van Nostrand Company. Inc. 1957.

4 Wilson D J, Goldstein R J; **Turbulent Wall Jets with Cylindrical Streamwise Curvature.**
Journal of Fluids Engineering, Vol 96, 1976 pp550.

Appendix A
Orifice Plate Calculations

The orifice plate was designed according to the British Standard 1042: Part1[23], and has D, D/2 tappings.

A.1 Working Equations in Metric Units

The volumetric flow rate through an orifice plate is given by

$$Q=\frac{\pi}{4}CZ_R Z_D \epsilon E d^2 \sqrt{\frac{2\Delta h}{\rho}} \qquad (A,1)$$

where
Q = Volumetric flow rate (m^3/s)
C = Discharge coefficient
Z_R = Reynold's number correction factor
Z_D = Pipe diameter correction factor
ϵ = Expansibility factor
E = Velocity of approach factor
d = Orifice diameter (m)
Δh = Orifice pressure difference (Pa)
ρ = Orifice fluid density at upstream tapping (kg/m^3)

The Reynold's number based on orifice diameter is given by

$$R_d=\frac{4\rho Q}{\pi\mu d} \qquad (A,2)$$

where
R_d = Reynold's number based on orifice diameter
μ = Orifice fluid dynamic viscosity (Pa.s)

The velocity of approach factor is given by

$$E=\frac{1}{\sqrt{1-m^4}} \qquad (A,3)$$

where
$m = (d/D)^2$
D = Upstream pipe diameter

There are two orifice plates that can be inserted into the pipeline, with diameters of 200mm and 125mm respectively. The measured flow variables are upstream pressure and orifice differential pressure.

A.2 Correction Coefficients d = 125mm

d = 0.1248m D = 0.154m m = 0.66 E = 1.326

A.2.1 Discharge Coefficient

From Figure A.1, for m = 0.66, C = 0.6113

A.2.2 Reynold's Number Correction

To calculate the Reynold's number, the upstream fluid density and viscosity are required. The fluid density is given by the ideal gas law

$$\rho = \frac{p_{up}}{RT_{up}} \qquad (A,4)$$

where
p_{up} = Upstream pressure (Pa)
T_{up} = Upstream temperature (K)
R = Gas constant for air = 287.26

The fluid viscosity is given by Rayleigh's equation as

$$\mu = 1.714 \times 10^{-5} \left(\frac{T_{up}}{273.15}\right)^{\frac{3}{4}} \qquad (A,5)$$

Since the upstream temperature is not measured directly, it is calculated using the fact that the fan compresses air almost adiabatically. The relationship between temperatures and pressures for an adiabatic compression is given by

$$T_2 s = T_1 \left(\frac{p_2}{p_1}\right)^{\frac{\gamma-1}{\gamma}} \qquad (A,6)$$

where p_1 and T_1 refer to atmospheric air properties at the fan inlet, and p_2 and T_2 refer to air properties at the fan exit, ie.

upstream of the orifice plate. T_{2s} refers to the ideal temperature at the fan exit if the compression were totally isentropic.

The isentropic efficiency of a compressor is usually quite similar to the mechanical efficiency, and since the latter is known, the former can be deduced. The isentropic efficiency is given by

$$\eta_{isentropic}=\frac{(T_{2s}-T1)}{(T_2-T_1)} \qquad (A,7)$$

Substituting the adiabatic compression equation and simplifying in terms of T_2 yields

$$T_2=T_1\left[1+\frac{\left(\left(\frac{p_2}{p_1}\right)^{\frac{\gamma-1}{\gamma}}-1\right)}{\eta_{isentropic}}\right] \qquad (A,8)$$

where the fan isentropic and mechanical efficiencies can be interchanged. From the fan performance chart in Appendix D2, the mechanical efficiency can be assumed to have an average value of 0.6.

The Reynold's number now being known, Figure A.2 can be used to find the Reynold's number correction. For m = 0.66, the data in this figure can be assigned an equation of the form

$$Z_R=a+b\ln(R_d) \qquad (A,9)$$

A least squares fit of the data yields the following constants for a and b:
a = 1.1315 and b = -9.565×10^{-3}.

A.2.3 Pipe Diameter Correction

From Figure A.3, for m = 0.66 and D = 0.154m = 6in, Z_D = 1.004.

A.2.4 Expansibility Factor

The expansibility factor can be read from Figure A.4. Since the pressure ratio h/p is required in imperial units, it is necessary to first convert h/p in metric units to imperial units. The conversion is given by

$$\left(\frac{h}{p}\right)_{imperial} = 27.74\left(\frac{h}{p}\right)_{metric} \qquad (A,10)$$

Writing the simple linear relationship between ϵ and $(h/p)_{imperial}$ in equation form yields

$$\epsilon = 1 - 1.469\times10^{-2}\left(\frac{h}{p}\right)_{imperial} \qquad (A,11)$$

A.3 Correction Coefficients d = 100mm

d = 0.100m D = 0.154m m = 0.42 E = 1.103

A.3.1 Discharge Coefficient

From Figure A.1, for m = 0.42, C = 0.60666

A.3.2 Reynold's Number Correction

Using the same procedure as before to find the Reynold's number, Figure A.2 can be used to find the Reynold's number correction. For m = 0.42, the data in this figure can be assigned an equation of the form

$$Z_R = a + b\ln(R_d) \qquad (A,12)$$

A least squares fit of the data yields the following constants for a and b:
a = 1.0972 and b = -7.391×10^{-3}.

A.3.3 Pipe Diameter Correction

From Figure A.3, for m = 0.42 and D = 0.154m = 6in, Z_D = 1.0025.

A.3.4 Expansibility Factor

Writing the simple linear relationship between ϵ and $(h/p)_{imperial}$ in equation form yields

$$\epsilon = 1 - 1.224\times10^{-2}\left(\frac{h}{p}\right)_{imperial} \qquad (A,13)$$

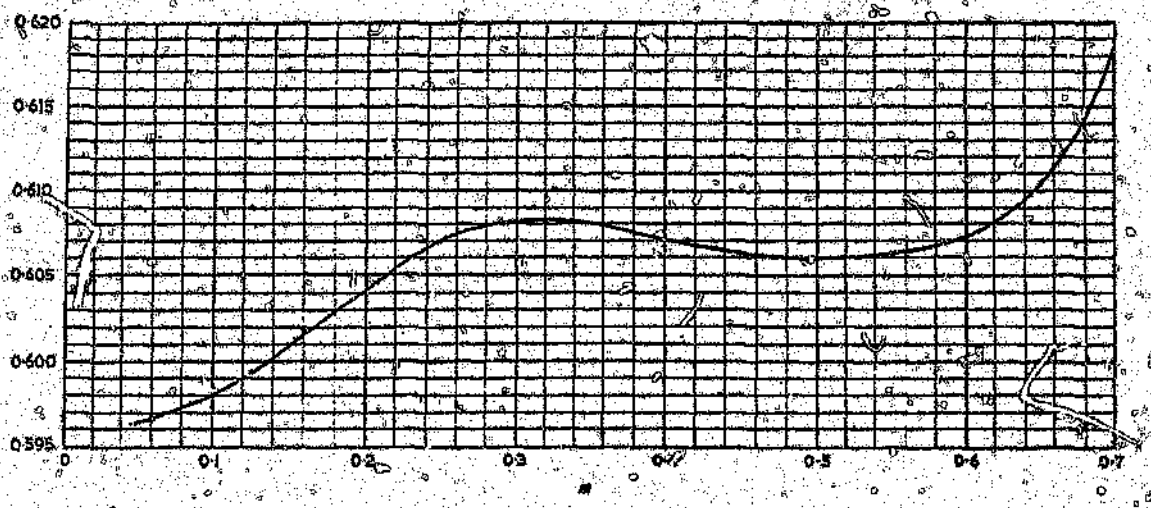

Figure A.1: Discharge coefficient.

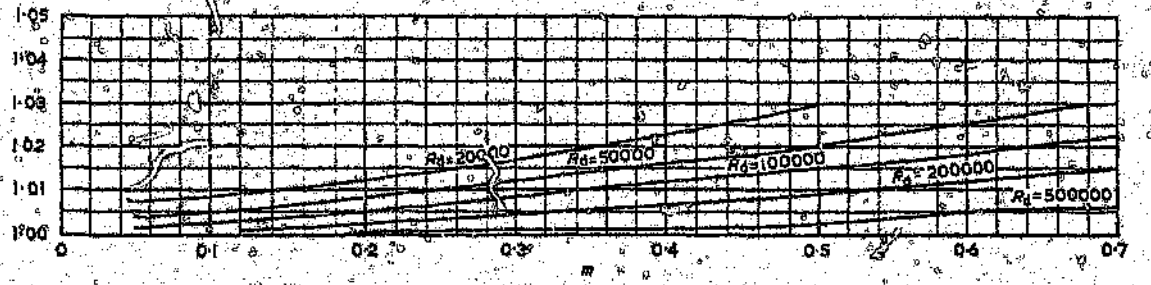

Figure A.2: Reynold's number correction factor.

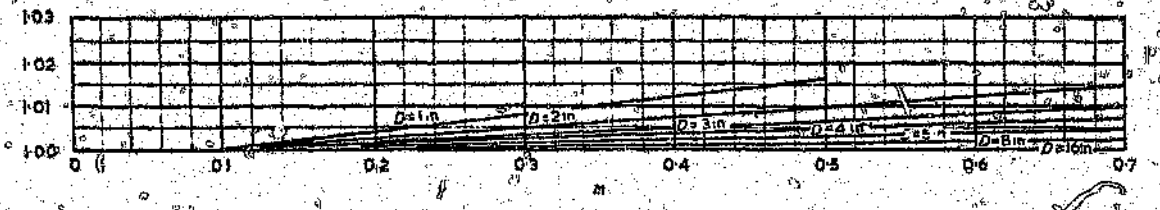

Figure A.3: Pipe size correction factor.

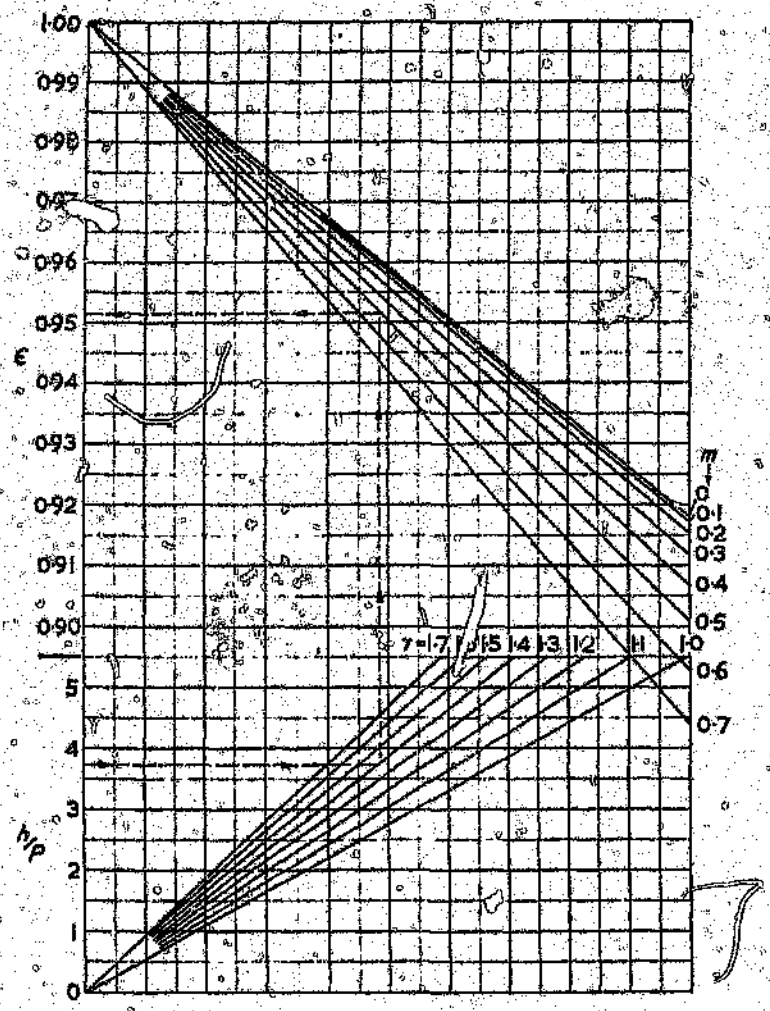

Figure A.4: Expansibility factor.

Appendix B
Wall Pressure Distribution

The wall static pressure distribution can be calculated if the velocities everywhere along its length are known. Since the stream-function, Ψ, of the flow is known, the u and v velocity components are easily found using

$$u(x,y)=\frac{\partial\psi}{\partial y} \qquad v(x,y)=\frac{-\partial\psi}{\partial x} \tag{B,1}$$

B.1 Elementary Flows

B.1.1 Uniform Stream

$$\psi=Uy \tag{B,2}$$

$$u(x,y)=U \qquad v(x,y)=0 \tag{B,3}$$

B.1.2 Source

$$\psi=\frac{q}{2\pi}\arctan\left(\frac{y}{x}\right)+c \tag{B,4}$$

$$u(x,y)=\frac{q}{2\pi}\frac{x}{(x^2+y^2)} \qquad v(x,y)=\frac{q}{2\pi}\frac{y}{(x^2+y^2)} \tag{B,5}$$

B.1.3 Doublet

$$\psi=\frac{\mu}{2\pi}\frac{y}{(x^2+y^2)} \tag{B,6}$$

$$u(x,y)=\frac{\mu}{2\pi}\frac{(x^2-y^2)}{(x^2+y^2)^2} \qquad v(x,y)=\frac{\mu}{2\pi}\frac{2xy}{(x^2+y^2)^2} \tag{B,7}$$

B.1.4 Vortex

$$\psi = \frac{-k}{2\pi} \ln(\sqrt{x^2+y^2}) + c \qquad \text{(B,8)}$$

$$u(x,y) = \frac{-k}{2\pi} \frac{y}{(x^2+y^2)} \qquad v(x,y) = \frac{k}{2\pi} \frac{x}{(x^2+y^2)} \qquad \text{(B,9)}$$

B.2 Combined Flow

The combined flow is given by

$$\psi = Uy + \frac{q}{2\pi} \arctan\left(\frac{y}{x}\right) - \frac{\mu}{2\pi} \frac{y}{(x^2+y^2)} + \frac{k}{2\pi} \ln(\sqrt{x^2+y^2}) + c \qquad \text{(B,10)}$$

where

$q = U\ C_d\ a + Q/b$

$\mu = 2\ \pi\ U\ a^2$

$k = U\ C_l\ a$

The resulting velocities are

$$u(x,y) = U + \frac{q}{2\pi} \frac{x}{(x^2+y^2)} - \frac{\mu}{2\pi} \frac{(x^2-y^2)}{(x^2+y^2)^2} + \frac{k}{2\pi} \frac{y}{(x^2+y^2)} \qquad \text{(B,11)}$$

$$v(x,y) = \frac{q}{2\pi} \frac{y}{(x^2+y^2)} - \frac{\mu}{2\pi} \frac{2xy}{(x^2+y^2)^2} - \frac{k}{2\pi} \frac{x}{(x^2+y^2)} \qquad \text{(B,12)}$$

The resultant of theses velocities is given by Pythagoras as

$$V_R = \sqrt{u(x,y)^2 + v(x,y)^2} \qquad \text{(B,13)}$$

B.3 Pressure Difference

The difference in pressure between the atmosphere and the wall static pressure tapping is derived using Bernoulli

$$p_{atm} = p_{tapping} + \frac{1}{2} \rho V_R^2 \qquad \text{(B,14)}$$

$$\Delta p = p_{atm} - p_{capping} = \frac{1}{2}\rho_{air} V_R^2 \qquad (B,15)$$

Converting this pressure difference to a difference in liquid column height of an alcohol manometer yields

$$\Delta h = \frac{\Delta p}{\rho_{alcohol} g} \qquad (B,16)$$



Appendix C
Structural Analysis

C.1 Test Section Beams

The maximum deflection of a beam, with fixed supports at both ends and uniformly loaded, is given by Shigley[26] as

$$\delta_{max} = \frac{qL^2}{384EI} \qquad (C.1)$$

where
δ_{max} = Maximum beam deflection (m)
q = Loading per unit length (N/m)
L = Beam length (m)
E = Modulus of elasticity (N/m^2)
I = Area moment of inertia (m^4)

For the given design, the beams are spaced 0.5m apart and are required to support the tunnel floor or ceiling which is subject to a pressure loading of 5000 Pa. This yields a beam loading, q, of 2500 N/m.

For wood, ie. pine, Shigley[26] gives E = 11 GPa.
The beam cross-section is 300mm x 30mm, yielding $I = 67.5 \times 10^{-6}$.
Although the beams are 3.5m long, they are supported inside the test section by vertical columns. The maximum unsupported length is 1.5m, ie. the section of beam spanning the flow channel. It is for this reason that the beam is considered to have fixed supports at each end.

Substituting the above values into the deflection equation yields δ_{max} = 0.044mm, which is negligibly small.

C.2 Test Section Floor and Ceiling

The test section floor and ceiling are divided into 0.5m square plates by the beam structure they are attached to. Dubbel[27] gives the maximum deflection of a simply supported square plate with uniform loading to be

$$\delta_{max} = \frac{CPb^4}{Eh^3} \qquad (C.2)$$

where
δ_{max} = Maximum plate deflection (m)
b = Plate half-length (m)
C = Geometric factor = 0.71 for a square plate
P = Plate loading pressure (Pa)
E = Modulus of elasticity (N/m^2)
h = Plate thickness (m)

For a 0.5m square plate, b = 0.25m.
The test section is subject to a pressure loading of 5000 Pa.
For wood, ie. particle board, Shigley[26] gives E = 11 GPa.
The plate thickness is 22mm.

Substituting the above values into the deflection equation gives a maximum deflection of 0.1mm.

C.3 Flexible Walls

The maximum deflection of the flexible test section walls is required to establish the waviness these will have when they are sucked onto the actuator slides. Since the sheet metal wall can be regarded as a very long beam with multiple supports and uniform loading, the slope of the beam at each support is zero. The maximum deflection of each section of beam is thus identical to that of a beam with fixed supports and uniform loading, which is given by Shigley[26] as

$$\delta_{max} = \frac{qL^4}{384EI} \qquad (C,3)$$

where

δ_{max} = Maximum beam deflection (m)
q = Loading per unit length (N/m)
L = Beam length (m)
E = Modulus of elasticity (N/m^2)
I = Area moment of inertia (m^4)

The flexible walls are 0.5m wide, and subject to a pressure loading of 1000 Pa, yielding a beam loading, q, of 500 N/m.
For galvanized steel sheet, E = 200 GPa.
For a 0.5m wide and 0.8mm deep section, $I = 2.133 \times 10^{-11}$.
The actuator slide spacing, and hence the beam length, is 125mm.

Substituting the above values into the deflection equation results in a maximum deflection, and hence maximum waviness, of 0.075mm.

Appendix D
Fan Characteristics
D.1 Tunnel Drive Fans

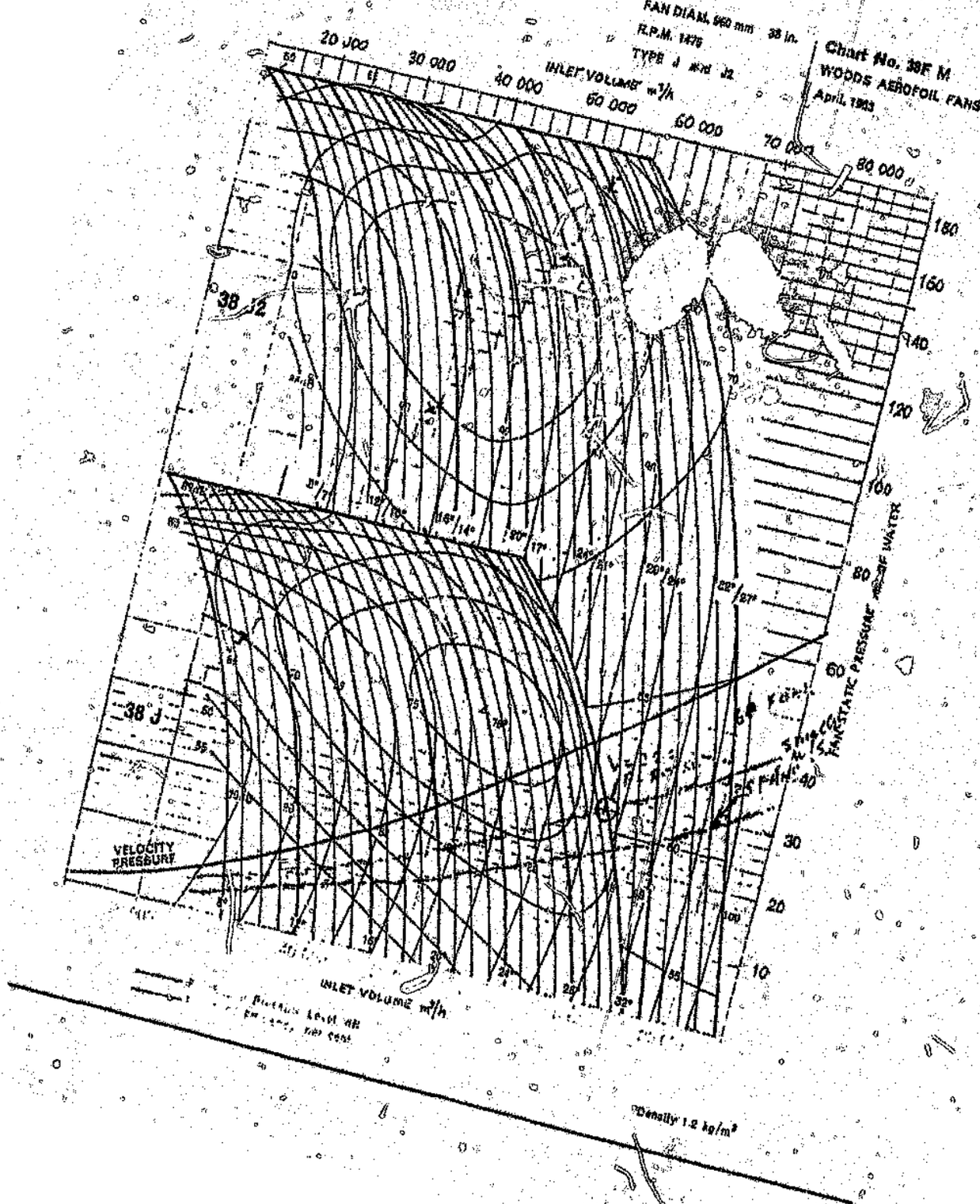

D.2 Circulation Control Blower

Donkin series HPLV high pressure blowers

Sizes 500, 560, 630 & 710 Widths 1,0 0,85 0,71

Speed 48 r/s (2880 r/min)

Air Density 1,2 kg/m³

Outlet Duct — Ø 150 mm Outlet Area 0,0177 m²

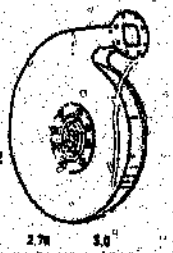

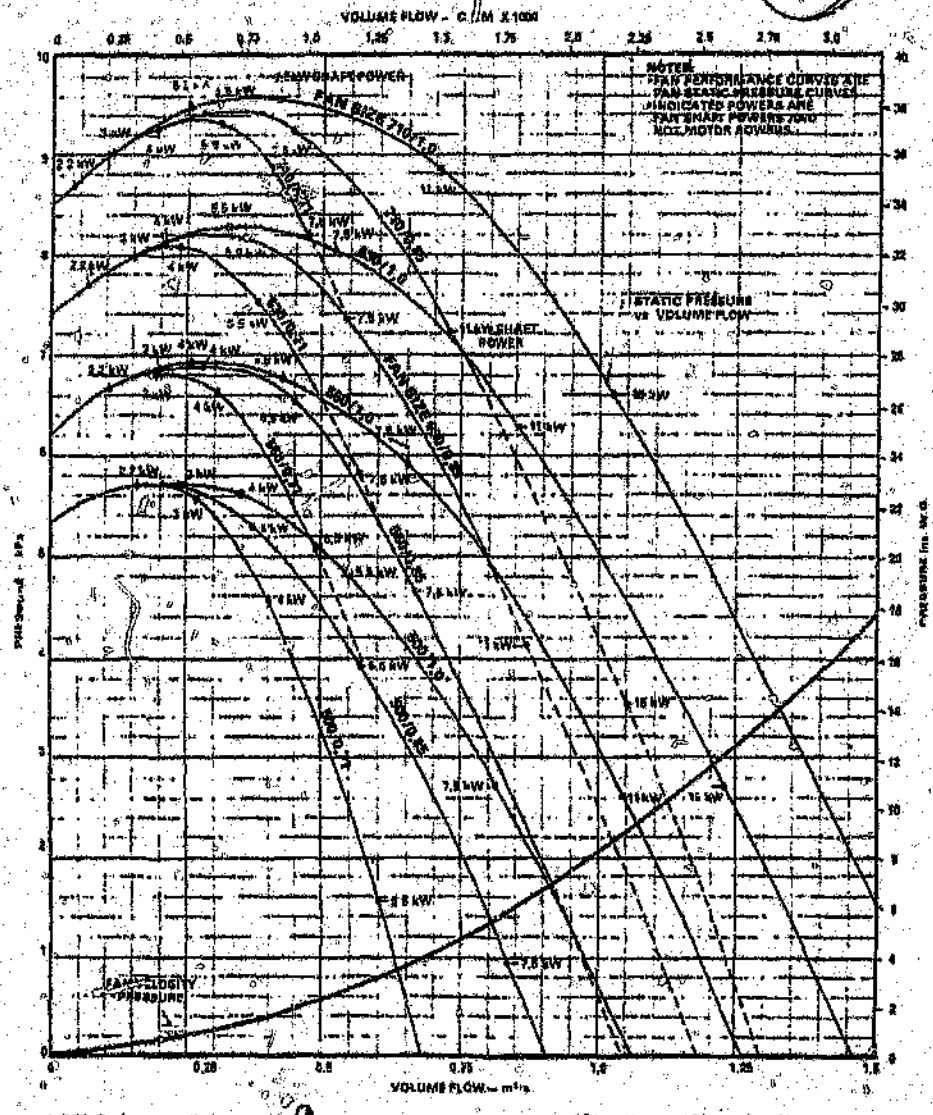

NOTE Performance Data is based on tests carried out in accordance with BS848 : Part 1 : 1963 — Test Method No. 1.

D.3 Wall Suction Fan

Serie CBT/COT et CST/CSB
Courbes caracteristiques

CBT/COT und CST/CSB
Leistungskennlinien

Series CBT/COT and CST/CSB
Caracteristics curves

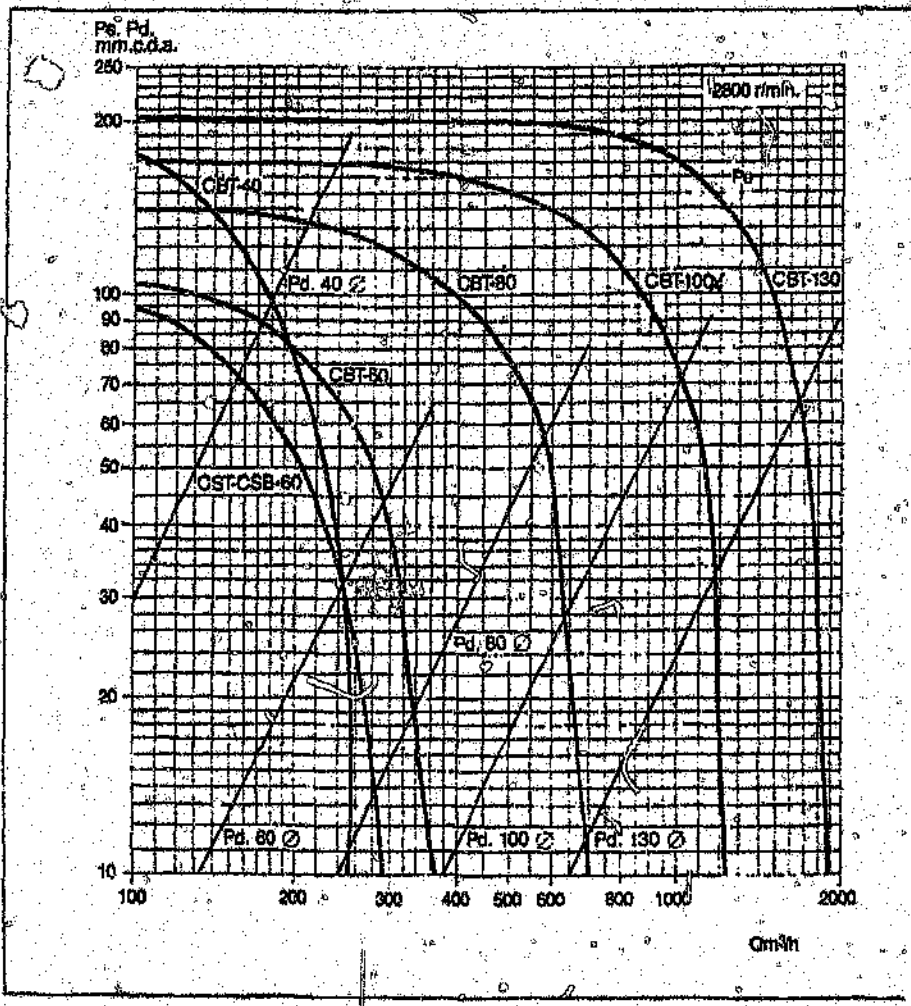

Qv=debit d'air en m³/h.
air flow in m³/h.
Luftmenge in m³/h.
Ps=pression statique en mm c.d.a.
static pressure in mm c.w.g.
statischer Druck in mm ws
Pd=pression dynamique en mm c.d.a.
dynamic pressure in mm c.w.g.
Staudruck in mm ws
Air sec normal à 20° C/760 mm. densité 1,2 kg/m³
Normal dry air at 20° C/760 mm. density 1,2 kg/m³
Normale trockene Luft bei 20° C/760 mm. Dichte 1,2 kg/m³

Laboratoire d'essais aérodynamiques S&P
Norme AMCA Standart 210-67 fig. 1.1.
Aerodynamic test laboratory S&P
AMCA standard n° 210-67 fig. 1.1
S&P Aerodynamische Versuchslabor
AMCA Standard 210-67 fig. 1.1.

Appendix E
Wiring Diagrams
E.1 A/D, I/O and PC Interface

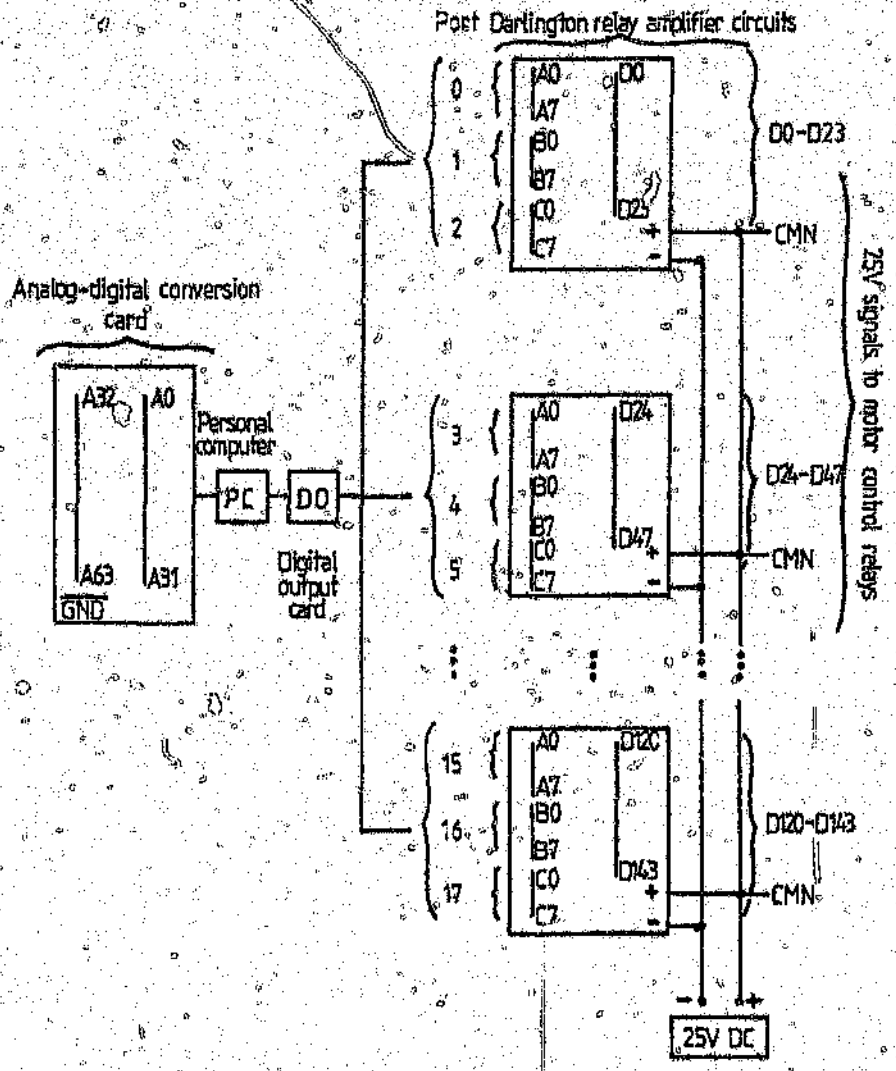

E.2 Transducer Wiring

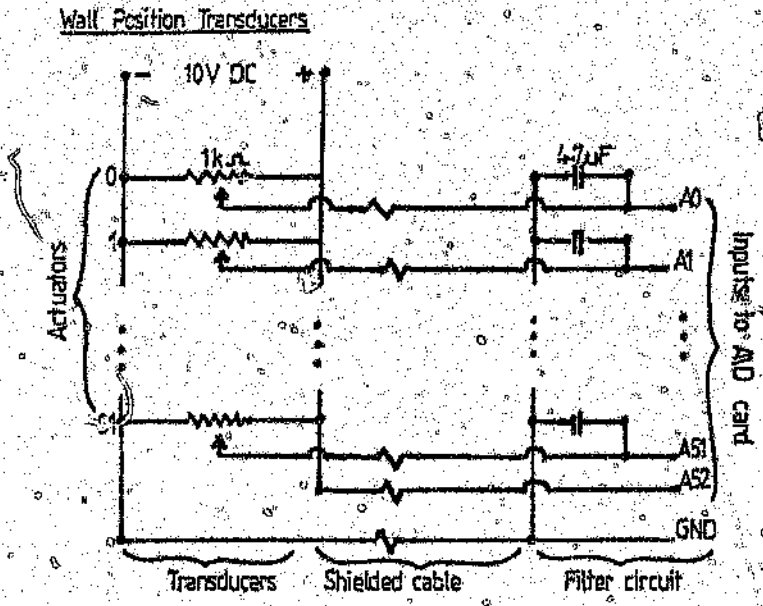

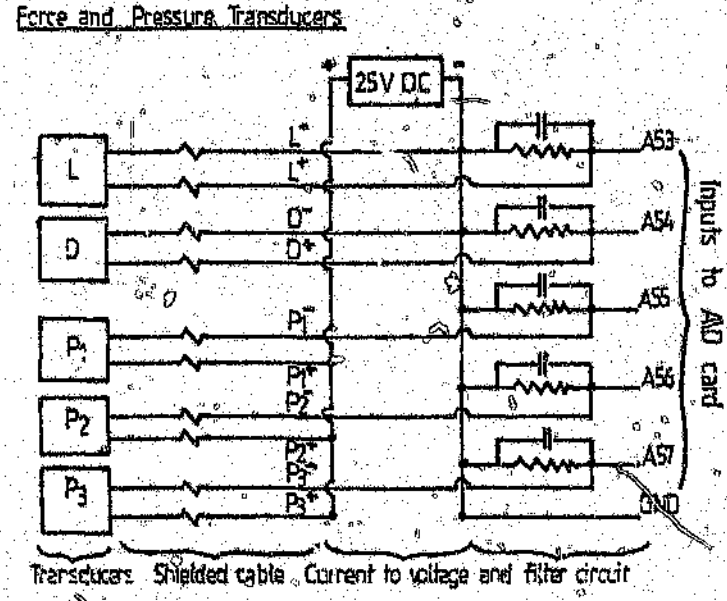

E.3 Actuator Relay Wiring

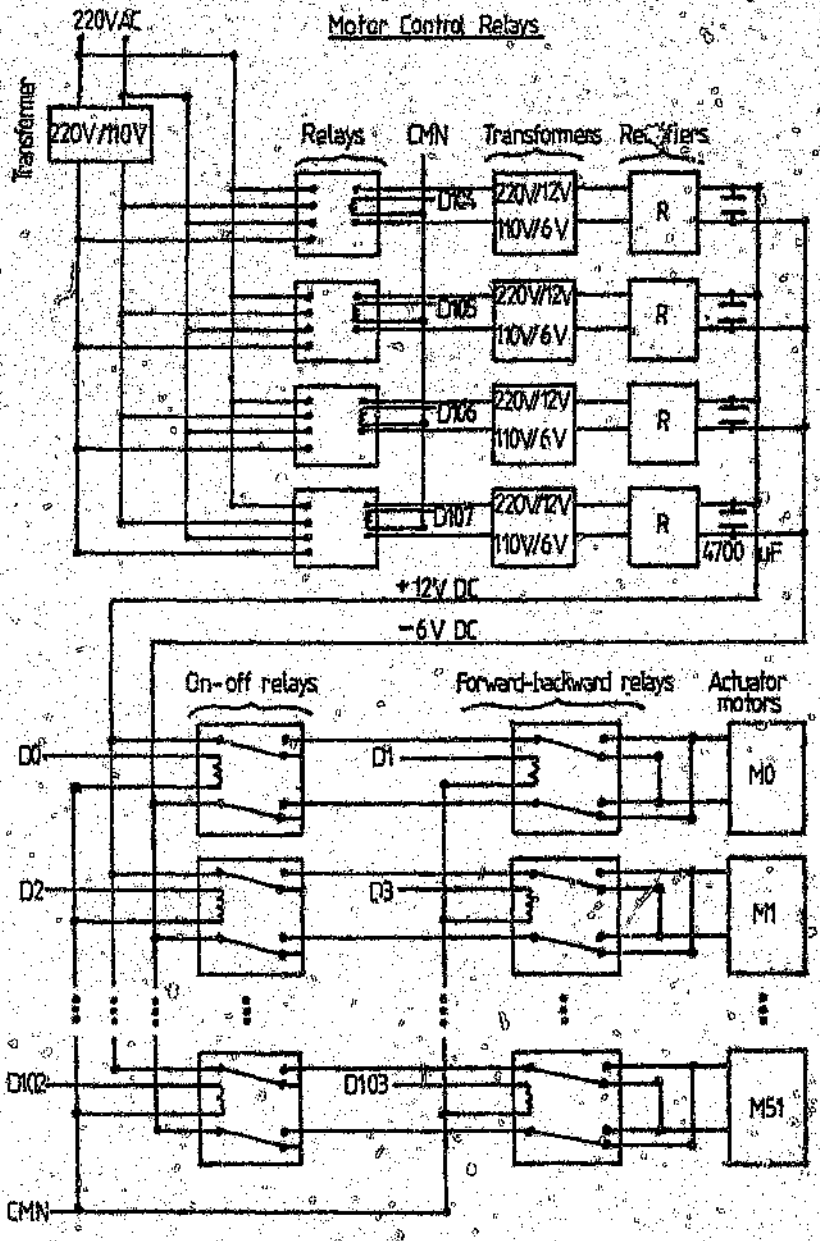

Appendix F
Software





Dysan 100

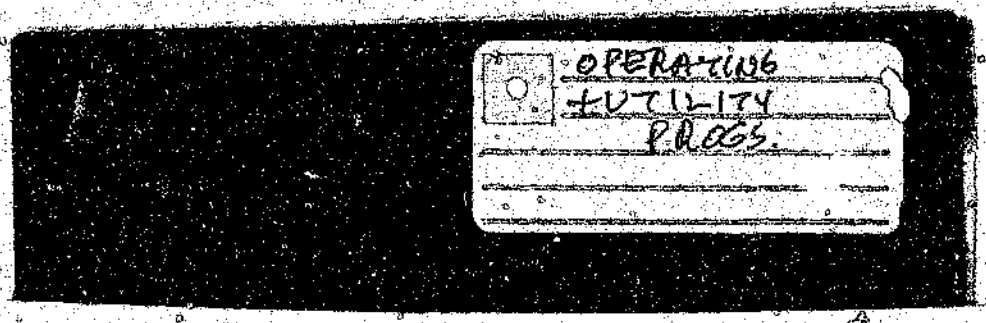



Dysan 100

Author: Berndt Roland Gunther.
Name of thesis: Adaptive wall wind tunnel investigation of a circulation controlled circular cylinder.

PUBLISHER:
University of the Witwatersrand, Johannesburg
©2015

LEGALNOTICES:

Copyright Notice: All materials on the University of the Witwatersrand, Johannesburg Library website are protected by South African copyright law and may not be distributed, transmitted, displayed or otherwise published in any format, without the prior written permission of the copyright owner.

Disclaimer and Terms of Use: Provided that you maintain all copyright and other notices contained therein, you may download material (one machine readable copy and one print copy per page)for your personal and/or educational non-commercial use only.

The University of the Witwatersrand, Johannesburg, is not responsible for any errors or omissions and excludes any and all liability for any errors in or omissions from the information on the Library website.